



# Particle Acceleration in the Magnetic Field of the Microquasar Cygnus X-3

Teilchenbeschleunigung in dem Magnetfeld des Mikroquasars Cygnus X-3

#### **Elena Lammert**

A thesis submitted for the academic degree of

Master of Science (MSc.)

in the TUM study program
Physics (Nuclear, Particle, and Astrophysics)

26.02.2025

Technical University of Munich School of Natural Sciences Department of Physics

Norwegian University of Science and Technology Faculty of Natural Sciences Department of Physics

First Examiner Prof. Dr. Hans-Thomas Janka

**Second Examiner** Prof. Dr. Elisa Resconi

External Supervisor Prof. Dr. Michael Kachelrieß

## **Abstract**

The microquasar Cygnus X-3 is one of the most enigmatic Galactic photon sources hosting a compact object, which orbits around a Wolf-Rayet star and develops a non-continuous jet. Recently, PeV photons were found to originate from the Cygnus bubble with Cygnus X-3 being a promising source. Aim of this work is to develop a model that describes the particle interactions leading to high-energy secondary particles. Based on the hadronic scenario, a program is designed to incorporate the characteristic photon background, geometry and magnetic field of Cygnus X-3 providing a framework for quantitative modeling of secondary particle production. A key aspect of this model is the formation of a cocoon structure by the jet in an active state, creating a secondary promising acceleration region. Reconnection appears close to the black hole while shock acceleration is considered at the edge of the cocoon. Both regions were found to be capable of accelerating protons up to PeV energies. The main photon production mechanism was identified to be photohadronic interactions inside the acceleration region while proton-proton interactions dominate beyond. In addition to the photon flux, the resulting neutrino flux was investigated confirming that Cygnus X-3 is a source for high-energy neutrinos following the flavor ratio  $1_e: 2_{\mu}: 0_{\tau}$ . The findings of this work provide a theoretical foundation supporting Cygnus X-3 as a high-energy source for both photons and neutrinos, while also delivering a simulation tool that can be modified to further parameter studies of Cygnus X-3.

# Zusammenfassung

Der Mikroquasar Cygnus X-3 ist einer der effizientesten galaktischen Teilchenbeschleuniger, bestehend aus einem kompakten Objekt, das einen Wolf-Rayet Stern umkreist und einen nicht-kontinuierlichen Jet ausbildet. Aus der Cygnus Blase konnten bereits PeV Photonen nachgewiesen werden, welche in Cygnus X-3 ihren Ursprung haben könnten. Ziel dieser Arbeit ist es, ein Modell zu entwickeln, das qualitative Aussagen über Wechselwirkungen der anwesenden Teilchen tätigt. Basierend darauf wird ein Program entwickelt, das Simulationen erzeugt, um quantitative Angaben zu den erwarteten Photon- und Neutrinoflüssen zu machen. Hierbei wird sich auf das hadronische Scenario beschränkt, welches Protonen als Quelle für hochenergetische γ-Strahlen und dazgehörige Neutrinos heranzieht. In dieser Arbeit sind besonders zwei für Cygnus X-3 charakteristische Modelle miteinander kombiniert worden, um zu überprüfen, inwiefern es möglich ist, Cygnus X-3 als Quelle für PeV Photonen und hochenergetische Neutrinos anzusehen. Zum einen wird magnetische Rekonnektion als Beschleunigungsmechanismus am kompakten Objekt betrachtet. Dieser zeigt sich als besonders effektiv und ist in der Lage PeV Photonen und hochenergetische Neutrinos zu produzieren. Weiterhin ist für Cygnus X-3 angenommen worden, dass der Jet im aktiven Zustand eine Kokon-Struktur im Medium ausbildet, wodurch sich eine zweite Beschleunigungsregion ergibt. Diese erweist sich ebenfalls als vielversprechend, wobei Sekundärteilchen erzeugt werden, die die gemssenen y-Strahlen erklären können. Diese werden in beiden Beschleunigungszonen mit den zusätzlichen Neutrinos durch photohadronische Wechselwirkungen erzeugt und außerhalb dieser sind Proton-Proton Wechselwirkungen dominant. Dadurch lässt sich Cygnus X-3 fundiert als bedeutende galaktische Hochenergiequelle für Photonen und Neutrinos etablieren, wobei gleichzeitig eine numerische Grundlage für weiterführende Parameterstudien geschaffen wird.

## **Declaration of Authorship**

I hereby declare that the thesis submitted is my own unaided work. All direct or indirect sources used are acknowledged as references. I am aware that the thesis in digital form can be examined for the use of unauthorized aid and in order to determine whether the thesis as a whole or parts incorporated in it may be deemed as plagiarism. For the comparison of my work with existing sources I agree that it shall be entered in a database where it shall also remain after examination, to enable comparison with future theses submitted. Further rights of reproduction and usage, however, are not granted here. This paper was not previously presented to another examination board and has not been published.

## Ehrenwörtliche Erklärung

Ich erkläre hiermit ehrenwörtlich, dass ich die vorliegende Arbeit selbständig angefertigt habe. Die aus fremden Quellen direkt und indirekt übernommenen Gedanken sind als solche kenntlich gemacht. Ich weiß, dass die Arbeit in digitalisierter Form daraufhin überprüft werden kann, ob unerlaubte Hilfsmittel verwendet wurden und ob es sich – insgesamt oder in Teilen – um ein Plagiat handelt. Zum Vergleich meiner Arbeit mit existierenden Quellen darf sie in eine Datenbank eingestellt werden und nach der Überprüfung zum Vergleich mit künftig eingehenden Arbeiten dort verbleiben. Weitere Vervielfältigungs- und Verwertungsrechte werden dadurch nicht eingeräumt. Die Arbeit wurde weder einer anderen Prüfungsbehörde vorgelegt noch veröffentlicht.

Trondheim, 26.02.2025

Ort. Datum

Unterschrift

Lanmon

## **Preface**

This thesis marks the end of my study career to become an astrophysicist. I knew early on that my dream was to explore the depths of the cosmos that surrounds us, and so the dream of studying astrophysics was born. Now I can finish my studies from Norway and would like to take this opportunity to thank everyone who has supported me.

First of all, I would like to thank Prof. Hans-Thomas Janka for his willingness to support my wish to study in Norway and to be my first examiner. I would also like to thank Prof. Elisa Resconi for agreeing to be my second examiner. My special thanks go to my supervisor Prof. Michael Kachelrieß for his professional support and the time he dedicated to me. Additionally, I thank Dr. Karri Koljonen for the helpful discussions during my work. I would also like to thank for the financial support by the EU programme Erasmus+.

I would also like to thank my partner, who was there especially during the challenging times of my studies, for his emotional support and encouragement in my work. Furthermore, I would especially like to thank my family for their unconditional support of my studies and all my friends in Germany and Norway who have made my studies a time I will truly enjoy to remember.

# Contents

1	Intr	roduction	1						
2	Fou	Foundations of High-Energy Astrophysics							
	2.1	Cosmic Rays	5						
	2.2	Astrophysical Neutrinos	9						
	2.3	X-Ray Binaries	10						
	2.4	Special Relativity	17						
	2.5	Particle Acceleration	20						
3	Суд	gnus X-3	27						
	3.1	Mass	27						
	3.2	Geometry	28						
	3.3	Photon Spectrum	30						
	3.4	Outburst Evolution Scenario	33						
	3.5	Magnetic Field	36						
	3.6	Ambient Particles	39						
4	Par	Particle Interactions							
	4.1	Energy Change	49						
	4.2	Particle Acceleration	49						
	4.3	Synchrotron Radiation	50						
	4.4	Photohadronic Interactions	53						
	4.5	Hadronic Interactions	55						
	4.6	Inverse Compton Scattering	57						
	4.7	Pair Production	59						
5	Numerical Setup 63								
	5.1	Particle Behavior in the Acceleration Region	63						
	5.2	Particle Spectrum on Earth	78						
	5.3	Simulation Setup	85						
6	Res	ults and Discussion	91						
	6.1	Acceleration Region $S_1$	91						
	6.2	Acceleration Region $S_2$	97						
7	Cor	nclusion and Outlook	101						

List of Constants	103
Bibliography	105

1 Introduction

In general, the term high-energy astrophysics includes various phenomena and objects that can only be observed in the universe under extreme conditions. The objects range from supermassive black holes to extraordinarily strongly magnetized neutron stars. Compact objects can reach densities of several nuclear densities  $\rho_{\rm nuc} \approx 3 \times 10^{14} \, {\rm g/cm^3}$  and in their vicinity particles can be accelerated up to the ultra-high-energy regime of  $10^{20}$  eV [1]. Particles propagating with high energies undergo various interaction mechanisms, which depend on their quantum physical characteristics like charge, spin and flavor.

These natural particle accelerators are highly efficient. Earth-based accelerators can accelerate particles up to the TeV regime, which is clearly below astrophysical ultra-high-energy particles. Ultra-high-energy cosmic rays (UHECR) are particles with the highest measured energies, in the EeV range, and are correlated with extragalactic origin [2]. Particles with energies in the TeV regime are called very-high-energy (VHE) cosmic rays and may be of galactic origin. In the study of all high-energy astroparticle physics, these cosmic laboratories, which are both galactic and extragalactic, therefore offer a unique opportunity to discover new physics and extend the current understanding of particle physics. The particles escaping the dense and turbulent acceleration regions and eventually reach Earth are called cosmic messengers. The great diversity of their individual properties requires a wide variety of detectors and telescopes to observe them. From the original particles and interactions, only the final products of the particles reach Earth.

An enormous number of cosmic particles from all directions reach the Earth's atmosphere every second. Deciphering these cosmic messengers and their information is one of the major tasks of current astrophysics. More precise telescopes provide a great potential to detect particles from regions that have never been explored. Of all cosmic messengers, photons are the most abundant particles in the universe reaching us with a wide range of energies. The lowest energy photons are classified as radio photons with energies detectable from approximately  $10^{-14}$  eV. On the other hand, photons from gamma-ray bursts (GRB)s can reach Earth with energies higher than  $10^{15}$  eV [3]. Photons have the advantage of not being charged, consequently they may scatter in the ambient medium without being deflected by magnetic fields. However, by detecting enough pho-

1

#### Chapter 1 Introduction

tons, including their incoming directions, scattering as a statistical process can be cancelled out and the direction of the photon source can be determined.

Charged particles are deflected by magnetic fields, making it impossible to detect their origin. As a result, all charged cosmic messengers contribute to a diffuse particle spectrum. These messengers, known as cosmic rays, reach energies of up to  $10^{20}$  eV [4]. The energy spectrum of cosmic rays is not yet fully understood, in the sense that it is not known exactly how the charged particles, a large fraction of which are protons, are accelerated to energies that contribute to the UHECRs.

Whenever gamma-rays are observed, two scenarios have to be distinguished. The leptonic model describes high-energy electrons that can scatter with the surrounding photons. The photons eventually gain high energy through the inverse Compton process. On the other hand, the hadronic model describes high-energy protons that scatter with the surrounding medium, where higher proton resonances are created. They decay under quantum number conservation into pions and nucleons. Neutral pions decay into high-energy gamma-rays, and charged pions eventually decay into electrons, positrons and the corresponding neutrinos.

This work focuses on hadronic acceleration and interaction scenarios including a characteristic neutrino signature, which is related to the hadronic scenario. Like photons, neutrinos are uncharged, and therefore lead directly in the direction of their origin. Due to their inherent nature as being weakly interacting particles, they can escape from denser regions than photons and carry information from regions where photons cannot escape. However, their small cross section makes them difficult to detect. It is therefore important to analyze as many cosmic messengers as possible to get an overall picture of the cosmic accelerator.

Although the origin of high-energy components of cosmic rays is not fully understood yet, possible sources are limited. GRBs and active galactic nuclei (AGN) are considered to be important sources. GRBs are divided into long (> 2 s) and short (< 2 s) bursts, which is directly linked to their different origins [4]. AGN are supermassive black holes with masses ranging from  $3 \times 10^7 \, M_\odot$  to  $5 \times 10^9 \, M_\odot$  at the center of galaxies, accreting material at up to 10 % of the Eddington rate [5]. AGN are characterized by their non-thermal spectrum. The emission spectrum can change over time and, above all, a strongly collimated jet can develop. Since the speed of light limits the propagation of information, the properties of AGN only change on large time scales due to their size.

In order to be able to analyze the acceleration mechanisms and particle interactions in these key regions of AGN, it helps to study the properties of microquasars. Microquasars share many characteristics with AGN and they behave similar to microscopic AGN in a time lapse due to their significantly smaller

extension. Moreover, recent studies indicate that microquasars also have the ability to accelerate particles to energies that contribute to the VHE cosmic rays [4]. The spectrum of diffuse cosmic rays can be divided into galactic particles reaching Earth and extragalactic particles. Since AGN are located in the center of galaxies, they can only contribute to the extragalactic part of the cosmic ray spectrum. Microquasars, however, are binary systems of a compact object and a main-sequence star. Since their mass is in the order of  $10\,M_\odot$  [2], it is not possible for them to achieve luminosities and particle energies approaching the magnitudes of AGN, which explains why only galactic microquasars have been observed so far.

In 1966, Cygnus X-3 was discovered and remains one of the most enigmatic microquasars yet discovered in the Milky Way. Cygnus X-3 is a high mass X-ray binary system hosting a Wolf-Rayet star with a compact object orbiting around [6]. In this circumference, strong magnetic fields are ambient and are able to accelerate charged particles. Studying Cygnus X-3 is interesting not only because of its superlative properties, but also because of the Wolf-Rayet star. The Wolf-Rayet star implies large stellar winds resulting in high accretion rates at the compact object, as well as high densities in the vicinity of the compact object. Particle acceleration may be particularly efficient, and specific scenarios have been developed based on the particle jet interacting with the stellar medium [6, 7, 8]. Due to the high densities in the acceleration region, the medium may be opaque to gamma-rays. Since protons contribute to the diffuse cosmic ray spectrum, high-energy neutrinos may be the only remaining cosmic messengers able to escape the dense acceleration region and carry information about the acceleration mechanism.

Aim of this work is to investigate the region close to the microquasar Cygnus X-3 to understand the acceleration and interaction mechanisms of protons and their secondary particles. Scenarios like diffusive shock acceleration have been intensively investigated over the last decades, however, they are not able to provide a full description for the galactic cosmic rays. Therefore, in recent years, the concept of magnetic reconnection has been discussed as an efficient way of accelerating particles. It was originally proposed to describe particle acceleration in solar flares. A further development of this concept is applied to Cygnus X-3. The stellar wind of the Wolf-Rayet star surrounds the region of particle acceleration, and therefore both protons and leptons are abundant. Among various scenarios for particle acceleration at Cygnus X-3, this work will focus on the hadronic acceleration scenario by calculating and simulating proton interactions with the surrounding medium. Recent measurements of the star-forming region Cygnus, which contains Cygnus X-3, have detected photons in the PeV regime [9]. As Cygnus X-3 is a promising particle accelerator, this work focuses on

#### **Chapter 1** Introduction

the possibility of producing these ultra-high-energy photons. Thus, a program has been developed to simulate and investigate how efficiently Cygnus X-3 can accelerate particles up to energies in the high energies. The program will encompass all known and most possible parameters to provide the most realistic picture of the ambient mechanisms in Cygnus X-3. Furthermore, corresponding neutrino spectra will be carried out simultaneously, which may be measured in future neutrino detectors, providing an overall picture of particle acceleration and resulting secondaries in the vicinity of Cygnus X-3.

In Chapter 2, the theoretical framework that applies to astrophysical accelerators such as Cygnus X-3 is introduced. Chapter 3 focuses on the properties of the system, paying particular attention to the ambient photons and protons, and the embedding of the system within a considerable geometry. Chapter 4 introduces all the interaction mechanisms that have been considered, with a particular emphasis on interaction rates, which play an important role in the development of the subsequent program. Chapter 5 outlines the fundamental logic of the developed program and introduces initial estimates of the expected outcomes by treating the configuration and interactions analytically. Finally, Chapter 6 presents the results, including the calculation of photon and respective neutrino spectra, which reveal the significant potential of Cygnus X-3 as an important galactic particle accelerator.

The following Chapter provides a brief overview of high-energy astrophysics, which generally refers to the measurement and related analysis of cosmic rays. The high-energy particle spectrum, which is the basis for cosmic ray studies, is explained. Neutrinos, which are a special part of this work, are discussed in more detail. Microquasars, also known as active X-ray binaries, are then introduced with an overview of their properties. Since the energies of the particles considered here exceed many times their rest mass, the important relativistic concepts are introduced. Finally, the Fermi mechanism, which is the general acceleration principle, is introduced with two specific applications to diffusive shock acceleration and reconnection, which are both considered to occur in Cygnus X-3.

In the following work, several fundamental physical constants and astrophysical units are used for calculations and theoretical derivations. These constants are expressed in the centimetre-gram-second (CGS) unit system and play a crucial role in astrophysical formulations. For consistency and simplicity, Tab. 7.1 provides an overview of the most important constants used in this work.

## 2.1 Cosmic Rays

Around the year 1600, William Gilbert developed a rudimentary electroscope, which should be involved in various scientific discoveries of the following centuries. A further development of that electroscope was also on board of the balloons that took off at the beginning of 20th century to measure the Earth's atmosphere penetrating radiation. Victor Hess measured an increase of radiation with height in atmosphere and concluded that the radiation originates mostly from extraterrestrial sources. In 1937, Pierre Auger detected air showers and conducted that incoming high-energy charged radiation causes cascades of secondary particles, which are mostly photons, muons and electrons [3].

Today, the overall variety of extraterrestrial particles penetrating the atmosphere is well known. It is common to define charged particles such as electrons, nucleons and their respective antiparticles as Cosmic Rays. In addition, a substantial flux of cosmic neutrinos is observed to reach Earth. It is evident that cosmic rays carry information from space to Earth, thereby providing unique information about the Earth's astrophysical circumference. The analysis of radioactive nuclei

#### **Chapter 2** Foundations of High-Energy Astrophysics

has revealed that the cosmic ray flux has remained constant by a factor of two over the past  $10^9$  years [10].

A sketch of different cosmic rays traveling from its source to Earth is shown in Fig. 2.1. Since different cosmic rays have different properties, each cosmic messenger faces different interaction mechanisms on its way to Earth. For instance, stable hadrons carry a charge, as do electrons, which means that they are deflected by magnetic fields. By the time they reach Earth, they have been deflected several times and therefore do not travel in the direction of origin. Photons and neutrinos, on the other hand, do not carry an electromagnetic charge, so they travel in the direction of their origin. Photons may have scattered, which is a stochastic process, so it is important to measure as many photons as possible to obtain information about their direction of origin. However, neutrinos are the only cosmic ray particles with interaction cross sections small enough to avoid being. This means that a neutrino may be the only messenger that can escape dense regions. However, the small cross section makes them difficult to detect. When cosmic rays with larger cross sections ( $e^{\pm}$ ,  $\gamma$ , p, ...) hit the atmosphere, they interact with the atmospheric gas, leading to the production of air showers.

Advanced measurement techniques depending on the radiation and energy have to be applied. To measure primary cosmic rays, it is necessary to measure above the atmosphere to avoid the production of air showers. This is why high-altitude balloons or, more recently, space telescopes are used. Ground-based detectors of cosmic rays measure air showers, and a combined measurement of Cherenkov light detectors allows analysis techniques to calculate several particle properties. To detect neutrinos, however, it is essential to shield the detector from any background radiation. Since neutrinos arrive on Earth with other cosmic rays, there is always a background of primary cosmic rays and air-shower particles. Neutrino detectors are therefore often underground, shielded from other radiation by the surrounding water, rock or ice.

The general energy spectrum of cosmic rays is well known and shown in Fig. 2.2. It is easy to see that protons dominate the cosmic ray spectrum. The protons range in energy from 1 GeV to  $10^{11}$  GeV. The shape of the spectrum can be described by a power law  $dN/dE \sim E^{-\gamma}$ , where  $\gamma$  has different values depending on the energy range. This broken power law is marked in the figure by the *knee* and the *ankle*. Up to the knee with energy at about  $10^{15}$  eV, the curve can be described by  $\gamma = 2.7$ . Between the knee and ankle up to energies of  $10^{19}$  eV, the slope is described by  $\gamma = 3.15$  [12]. It is difficult to obtain data at this energy due to detector techniques and the reduced particle flux. Today, however, a slope corresponding to  $\gamma = 2.7$  is again observed after the ankle. Greisen [13], and Zatsepin with Kuzmin [14, 15] predicted a spectral cut-off caused by the

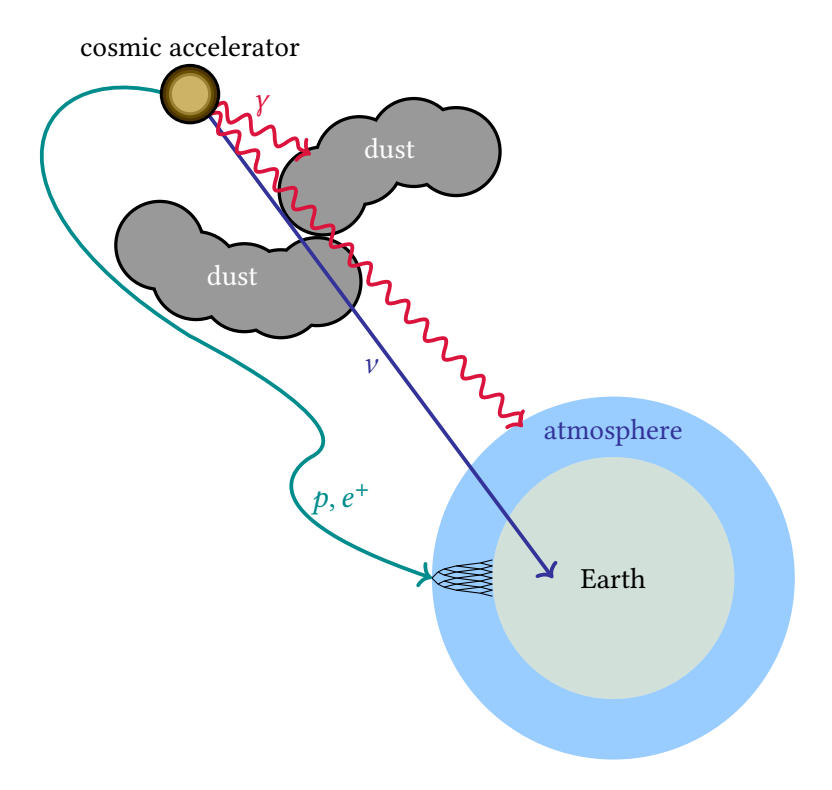
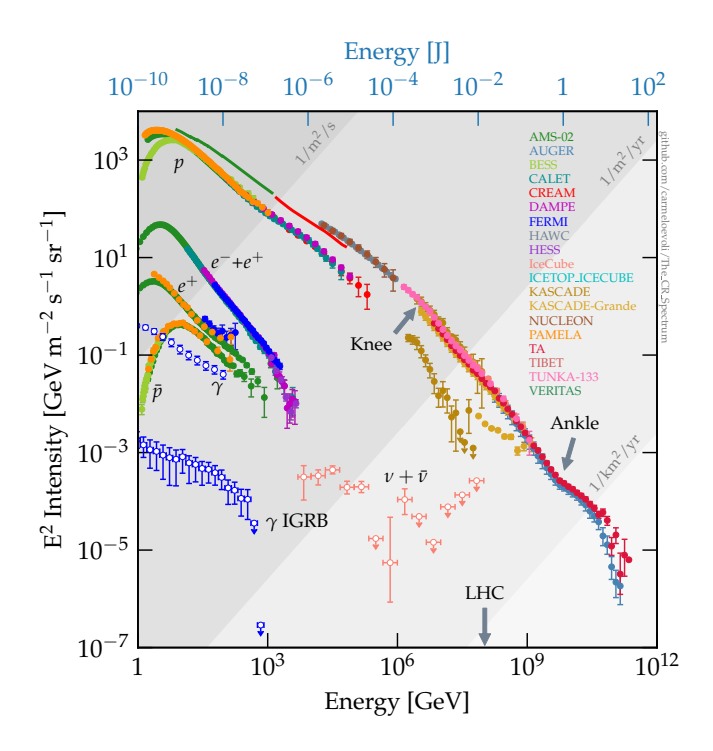


Figure 2.1: Sketch of cosmic messengers originating from a single source (yellow). Photons (red) can interact with interstellar dust, while charged particles, such as protons and electrons (green), are additionally deflected by magnetic fields. Furthermore, they cause electromagnetic showers in the atmosphere, leading to enormous secondary particle production (black). Neutrinos (blue) interact via weak interactions, thus propagating from the source without deflection or absorption.

ubiquitous cosmic microwave background. Primary cosmic rays tend to interact these photons limiting their energy to a threshold in the order of  $10^{20}$  eV.

The broken power-law slope in the spectrum for cosmic rays can be explained by considering possible sources of cosmic rays as in Ref. [16]. The detailed acceleration mechanism is explained in the following sections. However, a geometric approach maximal to particle energies is given by the Hillas criterion. A charged particle is accelerated in a source by magnetic fields. To be significantly accelerated, the energy gain must be greater than the energy loss due to other particle interactions, at least for some energy ranges. Assuming that the high-energy particle does not gain any energy outside the accelerating region, the maximum energy a particle can gain in the accelerating region is



**Figure 2.2:** Energy spectrum for different cosmic rays measured by several experiments (taken from Ref. [11], licensed under the MIT License).

$$E_{\max} = qBR. \tag{2.1}$$

Here, q = Ze is the particle charge, B is the magnetic field and R is the size of the accelerating region. The Hillas criterion is simply obtained by calculating the particle energy for the configuration where the Larmor radius  $R_{\rm L}$  exceeds the accelerating region  $(R_{\rm L} > R)$  [16].

Taking into account the Hillas criterion, it can be concluded that acceleration to higher particle energies requires larger acceleration regions or stronger magnetic fields. It is generally accepted that cosmic rays up to the knee are of galactic origin, mainly due to supernova remnants, although microquasars also contribute. Particles beyond the knee up to the cut-off are considered to be of extragalactic origin.

## 2.2 Astrophysical Neutrinos

The following explanations about the neutrinos are based on the description by K. Zuber [17].

Solar neutrinos were the first observed astrophysical neutrinos, detected by solar neutrino experiments originating from the pp chain in the core of the star. However, subsequent experiments also measured fewer neutrinos than expected. The missing electron neutrinos were later explained by introducing the concept of neutrino oscillations. Experimentally, this theory was confirmed by the *Soudbury Neutrino Observatory*, which eventually led to a small rest mass of neutrinos.

In 1987, the first neutrino signal outside the Solar System was detected, when two experiments (Kamiokande, IMB) simultaneously measured a total of 20 neutrinos from the supernova SN 1987A supporting the theory of supernova explosions.

Neutrinos are almost massless particles and carry no electric charge. They interact exclusively through the weak interaction by coupling to the  $W^\pm$  and  $Z^0$  bosons, the short range of the weak interaction being one reason for the rarity of the interaction of neutrinos. Since neutrinos are both unaffected by electromagnetic fields and have a small interaction cross section, they can carry important information directly from their source. However, this characteristic makes them difficult to detect.

#### 2.2.1 Neutrino Flavors

Neutrinos are fermions and come in three different flavors in the Standard Model. For the electromagnetically interacting fermions e,  $\mu$  and  $\tau$ , there are neutrinos in the flavors  $\nu_e$ ,  $\nu_\mu$  and  $\nu_\tau$  with their respective antiparticles.

In general, the Standard Model predicts that the neutrino does not interact strongly, electromagnetically. This includes the neutrino being a massless particle, which is in contrast to the observations mentioned above. Neutrino oscillations refer to the phenomenon that a neutrino produced in a certain flavor eigenstate is not necessarily detected in the same flavor eigenstate after a certain distance. This manifests in the quantum mechanical explanation of neutrino oscillations. In weak interactions, the flavor quantum state is conserved and therefore all neutrinos are created in a particular flavor eigenstate. This flavor eigenstate is a mixture of the corresponding mass eigenstates and for n eigenstates each flavor eigenstate can be described by the unitary mixing matrix  $U_{\alpha i}$  as

$$|\nu_{\alpha}\rangle = \sum_{i} U_{\alpha i} |\nu_{i}\rangle \tag{2.2}$$

and

$$|\nu_i\rangle = \sum_i U_{i\alpha}^* |\nu_\alpha\rangle \tag{2.3}$$

respectively. The index  $\alpha$  represents flavor and the index i denotes the mass. The mixing matrix has  $n \times n$  elements, where n is the number of eigenstates. For antineutrinos, the matrix element  $U_{\alpha i}$  must be replaced by the matrix adjunction  $U_{\alpha i}^*$ . Thus, a flavor eigenstate is always a linear combination of mass eigenstates. A mass eigenstate  $|i\rangle$  appears in the interaction picture as

$$|v_i(x,t)\rangle = \exp(-iE_it)|v_i(x,0)\rangle \tag{2.4}$$

and as a result the initial flavor eigenstate  $|\alpha\rangle$  propagates as

$$|v(x,t)\rangle = \sum_{i} U_{\alpha i} \exp(-iE_{i}t) |v_{i}\rangle.$$
 (2.5)

This elegantly illustrates that the initial flavor state varies because the mass eigenstates are time dependent and the phase factors are hence different due to distinct neutrino masses. The probability of measuring a neutrino with initial flavor  $\alpha$  in flavor  $\beta$  is given by the transition probability

$$P(\alpha \to \beta) = \left| \sum_{i} U_{\beta i}^* U_{\alpha i} \exp\left(-i \frac{m_i^2 L}{2E}\right) \right|^2, \tag{2.6}$$

where L is the source-detector distance. In general, neutrino oscillations can be measured in a certain regime, namely when the distance between detector and neutrino source is of the order of the neutrino oscillation length  $L/L_{\rm osc}\approx 1$ . If the distance between the source and the detector is too small, the neutrino has not oscillated enough to have a significant transition probability, and if the distance is too large, the neutrino has oscillated so much that all the neutrinos from the source arrive with a ratio determined by the initial neutrino flavors and the mixing angle.

## 2.3 X-Ray Binaries

Binary systems are generally defined as two stellar objects orbiting each other. They are born from the same collapsing cloud and therefore formed at the same time, although not necessarily with the same mass, resulting in different evolutionary timescales for the two stars. Since the ages of the stars in the system are equivalent, the more massive star leaves the main sequence earlier than its companion.

X-ray binaries (XRBs) are defined as stellar systems in which one component is a compact object, namely a neutron star or a black hole, and the other is a stellar companion. If the companion is an O- or B-type star of mass  $M>10\,M_\odot$  [18], the system is called a high-mass X-ray binary (HMXB). As a result of the mass and the associated temperature, the luminosity of optical photons in HMXBs is higher than the luminosity of X-ray photons. The companion star provides mass transfer to the compact object, which

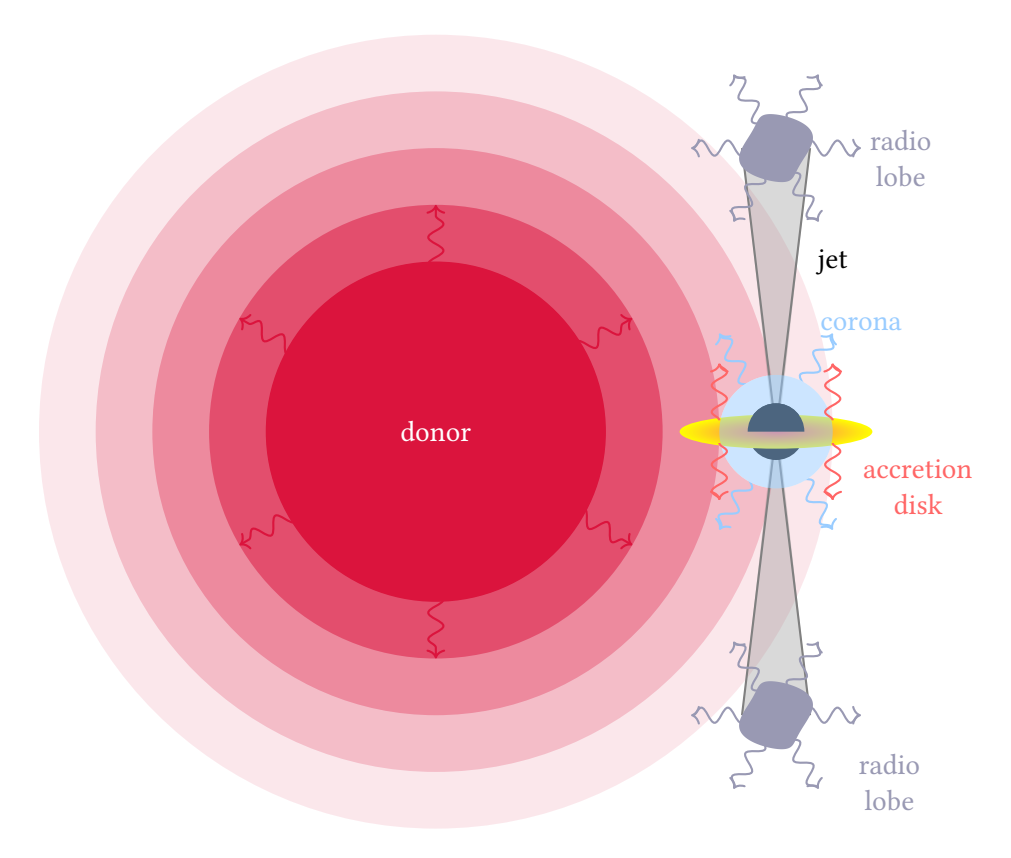


**Figure 2.3:** Exemplary representation of an X-ray binary with a black hole in active state. The donor star provides mass for the formation of the accretion disk with both emitting radiation corresponding to their temperatures. The corona surrounding the black hole contributes to the X-ray emission. The jet extends over long distances and develops strong radio lobes. Note that the scales do not correspond to reality.

occurs by different mechanisms depending on the mass of the companion. In binary systems with a companion of mass  $M < M_{\odot}$ , defined as low-mass X-ray binaries (LMXBs), mass is transferred via the Roche lobe overflow. This implies

an orbital separation small enough that the companion radius is larger than the Roche point. On the other hand, accretion in HMXBs is based on the stellar wind of the companion, since it has mass loss rates of  $\dot{M} \geq 10^{-6}\,M_{\odot}\,\mathrm{yr^{-1}}$  [19]. The compact object is in the dense stellar wind and is trapping the material. The material can either be stored in an accretion disk (*disk accretion*) or accreted directly by the compact object (*wind accretion*). Both mechanisms result in X-ray production but are based on different energy release mechanisms and therefore need to be distinguished [20].

Results from Koljonen et al. [21] have shown that Cygnus X-3 has different X-ray and corresponding radio states. This is associated with different accretion disk states, which correspond to different mass accretion rates. Therefore, it is reasonable to assume that the main accretion mechanism of Cygnus X-3 is due to the accretion disk, and wind accretion is not further explained.

LMXBs evolve on longer timescales, and the donor star remains on the main sequence longer because of its lower mass. On the other hand, HMXBs with a more massive star evolve on shorter timescales. Since Cygnus X-3 is known to be a HMXB, the theoretical framework focuses on the mechanisms in HMXBs. In the mass regime of a few solar masses, knowing the compact object mass is crucial as it determines whether the compact object is a black hole or a neutron star. Due to the fact that the pressure of the degenerated nucleons in the neutron star could not counteract gravity up to an arbitrary progenitor weight, the maximum mass for neutron stars is about 3  $M_{\odot}$  [22]. Compact objects heavier than this boundary mass must be black holes.

The phenomenology of HMXBs is illustrated in Fig. 2.3, where the mass donor has strong stellar winds that significantly exceed the orbital radius. A rotating accretion disk forms around the black hole, with viscous forces causing a loss of torque. The hot corona surrounds both the black hole and parts of the accretion disk. showing strong X-ray emission due to Comptonisation of electrons from the accretion disk. In the active state, relativistic jets can form, with characteristic radio emission from the radio lobes as they propagate. The jets are perpendicular to the plane of the accretion disk [22].

For mass measurements in eclipsing binaries, it can be used that the detected emission lines are modulated by the orbital period P. Additionally, an inclination i can be determined for binaries with a jet, and these values can be applied to the dynamical mass function [20]

$$f(M) = \frac{M(\sin(i))^3}{(M_1 + M_2)^2} = \frac{4\pi^2 (a\sin(i))^3}{GP^2},$$
 (2.7)

which is based on the third Kepler law and assumes a circular orbit. Here, M is the total mass of the binary system ( $M_i$ , j = 1, 2 represents the mass of each com-

ponent) and a is the semi-major axis of the elliptical orbit. However, it remains difficult to determine whether the compact object in Cygnus X-3 is a black hole or a neutron star. This paper assumes that the compact object is a black hole, since current research suggests a mass well above  $3 M_{\odot}$  [23, 24].

#### 2.3.1 Accretion Disk

The generic concept of accretion implies energy conversion and often ends in energy release by the binary system. The equations and explanations employed in this text can be found in Ref. [2]. Gravitational energy is converted to kinetic energy and radiated away, mostly in the form of X-rays. To calculate the luminosity, which is generally defined as  $L = \mathrm{d}E/\mathrm{d}t$ , the potential energy change for accreted matter is  $\mathrm{d}(mc^2)/\mathrm{d}t$ . Since not all the potential energy is converted into radiation, the total accretion luminosity depends on the accretion efficiency  $\chi$ . The X-ray luminosity resulting from the accretion can be written in the form

$$L_{\rm acc} = \chi \dot{m}c^2, \tag{2.8}$$

The luminosity is sensitive to the mass accretion rate, which often determines  $L_{\rm acc}$  in an active binary. During this process, the mass is heated to energies that cause radiation in the X-ray range. On the other hand,  $\chi$  is on the order of 10 % [20] for accreting black holes.

In general, the accretion process is limited by the angular momentum, which prevents matter from immediately reducing its gravitational potential and falling into the accreting object. In addition, the emitted radiation counteracts the gravitational force with radiation pressure

$$F_{\rm rad} = \frac{L_{\rm acc}\sigma_{\rm T}}{4\pi r^2 c},\tag{2.9}$$

with  $\sigma_T$  being the Thompson cross section. As a result, the radiation pressure limits the accretion rate, and thus the accretion luminosity, to a limit called the Eddington luminosity. This can be calculated by equating the forces  $F_{\rm rad} = F_{\rm g}$  with the gravitational force  $F_{\rm g} = GmM/r^2$  resulting from a mass m under the gravitational pull of a mass M. By assuming only Thompson scattering, the resulting luminosity can be written as

$$L_{\rm edd} = \frac{4\pi GcMm_{\rm p}}{\sigma_{\rm T}} \simeq 1.3 \times 10^{38} \left[ \frac{M}{M_{\odot}} \frac{\rm erg}{\rm s} \right]. \tag{2.10}$$

This is the maximum luminosity that can be achieved for spherically symmetric geometries and fully ionized hydrogen. There are exotic accretion mechanisms beyond the Eddington limit, which are not discussed here.

Applying Eq. (2.8) to the Eddington luminosity and combining it with Eq. (2.10), the Eddington accretion rate, is given by

$$\dot{M}_{\rm edd} = \frac{L_{\rm edd}}{\chi c^2} = \frac{4\pi G M m_{\rm p}}{\chi \sigma_{\rm T} c} \approx 2.218 \times 10^{-8} \left[ \frac{M}{M_{\odot}} \frac{1}{\rm yr} \right]. \tag{2.11}$$

This implies an Eddington accretion rate of about  $10^{-7} \frac{M_{\odot}}{\text{yr}}$  for the active black hole in Cygnus X-3.

The accretion rate is one of the important parameters determining the physics of the accretion disk, which is rather independent of the mass of the compact object. In general, an accretion disk forms when matter is accreted by a compact object and is forced to move in near Keplerian orbits. In astrophysics, two types of accretion disks are relevant: optically thick, geometrically thin disks, and optically thin, geometrically thick disks.

Here, geometrically thin and optically thick accretion disks are described in more detail, as this model applies to the assumptions made here for Cygnus X-3. This type of disk is known to be radiatively efficient, since the mass accretion rate is in the order of

$$10^{-2} \le \frac{\dot{M}}{\dot{M}_{\rm edd}} \le 1,\tag{2.12}$$

high enough to become optically thick for photons. At this point, the accretion disk can be assumed to be in hydrostatic equilibrium. As a result, the matter rotates on a constant circular orbit with radius R around the accreting object, and thus the radial velocity  $v_{\rm r}=0$ . This implies that the orbiting mass ideally has a Keplerian velocity

$$v_{\phi} = \sqrt{\frac{GM}{R}}. (2.13)$$

To continue falling towards the compact object, the mass must loose angular momentum. Thus viscosity plays a crucial role in these environments. The accretion disk temperature is high near the compact object and decreases outwards. The energy can be radiated away highly efficiently, since the accretion disk is considered to be geometrically thin  $z \ll R$ , whereby z represents half of the accretion disk thickness.

#### 2.3.2 Accretion Disk Temperature

The  $\alpha$ -disk model introduced by Shakura and Sunyaev [25] predicts turbulence enhanced viscosity. A detailed description of the model is provided in their paper. This model is used here to calculate an estimate of the temperature profile of

Cygnus X-3. It is important to note that it describes disks with an Eddington accretion rate, which implies that it is a boundary solution of Eq. (2.12).

To describe the radiation profile of the accretion disk, the energy and momentum loss of a single particle must be taken into account. For a proton inside the accretion disk at an orbital radius significantly larger than the Schwarzschild radius  $R_S$ , the potential energy can be described as

$$E_{\rm p} = \frac{GM_{\rm BH}m_{\rm p}}{r}. (2.14)$$

This implies that for protons on smaller orbits, more energy must be dissipated to further reduce the orbital radius. The total surface area of the accretion disk is  $2 \times 2\pi r$ , so the surface ring elements  $2\pi r dr$  become smaller near the black hole. However, they still have to emit more energy in absolute terms. It can further be assumed that the disk radiation is thermal radiation, and therefore each surface ring element emits blackbody radiation. With the previous considerations, this implies an increased disk temperature for smaller radii. Without any derivation, the total disk temperature profile can be described as

$$T(r) = \left(\frac{3GM\dot{M}}{6\pi\sigma_{\rm SB}r^3}\right)^{1/4} \left[1 - \left(\frac{3R_{\rm S}}{r}\right)^{1/2}\right]^{1/4}.$$
 (2.15)

Since all infinitesimally small ring elements emit blackbody radiation, Planck's law [22],

$$B(E,r) = \frac{2E^3}{(hc)^2} \frac{1}{\exp(E/k_{\rm B}T) - 1},$$
(2.16)

applies to the spectral energy density. The resulting photon flux as a function of energy can be described by integration over the Planck formula 2.16 as

$$F(E) = \frac{\cos(\theta)}{4\pi d^2} \int_{r_{\text{in}}}^{r_{\text{out}}} 2\pi r B(E, r) dr, \qquad (2.17)$$

where d is the distance from the source and  $\theta$  is the inclination angle between the plane of rotation of the accretion disk and a given observer of the photons. Furthermore, as a rough estimate, the differential photon density can be described by Eq. (3.7). However, this calculation is performed only over a half sphere, resulting in a factor of 0.5 being introduced.

#### 2.3.3 Jet Formation

The jet-launching mechanism for microquasars is not yet understood in detail. However, there is agreement on a general jet formation that is correlated with accretion. Matter in the accretion disk moves inwards by following ordered magnetic field lines. Following the magnetic field lines, the plasma in the inner accretion disk is ejected outwards, parallel to the axis of rotation of the accreting object. Since the accretion disk has a differential rotation, the magnetic field lines are spiraled perpendicular to their direction of expansion. In this structure, the plasma is both accelerated and collimated at the same time. This jet structure can extend over several orders of magnitude of the Schwarzschild radii  $r_{\rm S}$  [26].

Microquasars have much in common with quasars (active galactic nuclei) in terms of the qualitative description of the phenomena. However, the two main differences in scale between quasars and microquasars are the mass of the compact object, which is much smaller in microquasars and on the order of  $M_{\odot}$ . Also, the jet extends up to  $10^{17}$  cm for microquasars and  $10^{24}$  cm for quasars. The jet velocities for microquasars are typically between 0.3 c and 0.9 c [20].

The timescale of dynamical variation  $t_{\rm dyn}$  describes how fast a quasar or microquasar can change the properties of the jet, and thus  $t_{\rm dyn}$  describes how fast the jet is evolving. This timescale describes the time it takes for a particle to cross the Schwarzschild radius

$$R_{\rm S} = \frac{2GM}{c^2} \tag{2.18}$$

and thus it is directly proportional to the black hole mass M. Comparing microquasars (mq) to quasars (q) gives

$$\frac{t_{\rm dyn,mq}}{t_{\rm dyn,q}} = \frac{M_{\rm mq}}{M_{\rm q}} \sim a, \quad a \in [10^{-8}, 10^{-5}], \tag{2.19}$$

which justifies that the evolution of microquasars can help to understand the much slower evolution of quasars.

Having established theoretical foundations, the following explanations apply to microquasars and are based on the explanations in Ref. [20]. The general reason for jets is that they carry angular momentum

$$j = \dot{M}_{\rm W} r_{\rm A} \Omega, \tag{2.20}$$

where  $\dot{M}_{\rm W}$  is the wind mass loss rate and  $\Omega$  is the angular velocity. The Alfven radius,

$$r_{\rm A} = \left(\frac{8\pi^2 r^{12} B^4}{GM\dot{M}^2}\right)^{1/7},\tag{2.21}$$

describes the radius where magnetic energy density and kinetic energy density are equal which corresponds to the edge of the magnetosphere. For accretion to occur,  $j_{\rm acc} = 0.5 \dot{M}_{\rm acc} r \Omega$  must hold, with the mass accretion rate  $\dot{M}_{\rm acc}$  at the distance from the compact object r. This leads to

$$\frac{\dot{M}_{\rm W}}{\dot{M}_{\rm acc}} = 0.5 \left(\frac{r}{r_{\rm A}}\right)^2,\tag{2.22}$$

which means that most of the angular momentum is being carried away by the jet.

## 2.4 Special Relativity

Since the considered particles have energies significantly exceeding the rest mass energy, relativistic physics has to be considered. For every particle, a specific frame S' can be defined that moves with constant relativistic velocity v described by  $\beta = v/c$  with respect to an infinite number of rest frames  $S_i$ .

The covariance principle states that the laws of physics do not change in all inertial frames. The following sections briefly introduce what is important to consider for relativistic velocities of frames S' with respect to a rest frame S.

#### 2.4.1 Lorentz Transformation

Since the physics of relativity is formulated in 4 dimensional space-time in one inertial frame, it is convenient to use tensors. It is important to note that a physical quantity  $R_{\mu}$  and its contravariant counterpart  $R^{\mu}$ , related to an inertial frame, are connected via the metric tensor as  $g_{\mu\nu}R^{\mu}=R_{\nu}$ . For a more detailed mathematical description and derivation, refer to Ref. [27], as only the calculation conventions that are used are given below.

The Lorentz-transformation is explained in more detail in Ref. [28] and the following definitions are taken from there. The four-position vector  $x^{\mu}$  of a particle contains the time component in  $x^0$  and the three space coordinates are given in  $x^1, x^2$  and  $x^3$ . A particle at rest in S in a moving frame S' has a corresponding Lorentz factor

$$\gamma = \frac{1}{\sqrt{1 - \beta^2}},\tag{2.23}$$

which is defined by the velocity v of the moving frame. All components of the four-momentum vector of a rest frame transform into S' under the Lorentz transformation. For a simple motion of S' in the x-direction, the coordinates change by

$$x'^0 = \gamma(x^0 - \beta x^1), \quad x'^1 = \gamma(x^1 - \beta x^0) \quad x'^2 = x^2 \quad x'^3 = x^3,$$
 (2.24)

which is defined as a Lorentz-boost in the x-direction. However, if S' moves in all three dimensions, the Lorentz-boost becomes more complicated. In matrix notation it is defined as

$$\Lambda = \begin{pmatrix}
\gamma & -\gamma \beta_x & -\gamma \beta_y & -\gamma \beta_z \\
-\gamma \beta_x & 1 + (\gamma - 1) \frac{\beta_x^2}{\beta^2} & (\gamma - 1) \frac{\beta_x \beta_y}{\beta^2} & (\gamma - 1) \frac{\beta_x \beta_z}{\beta^2} \\
-\gamma \beta_y & (\gamma - 1) \frac{\beta_y \beta_x}{\beta^2} & 1 + (\gamma - 1) \frac{\beta_y^2}{\beta^2} & (\gamma - 1) \frac{\beta_y \beta_z}{\beta^2} \\
-\gamma \beta_z & (\gamma - 1) \frac{\beta_z \beta_x}{\beta^2} & (\gamma - 1) \frac{\beta_z \beta_y}{\beta^2} & 1 + (\gamma - 1) \frac{\beta_z^2}{\beta^2}
\end{pmatrix}.$$
(2.25)

When a particle in S' is Lorentz-boosted in S, the four-position vector  $x^{\mu}$  is transformed by the corresponding Lorentz-transformation matrix as

$$x^{\prime \mu} = \Lambda^{\mu}_{\nu} x^{\nu}. \tag{2.26}$$

#### 2.4.2 Proton Rest Frame

The scope of this work is to describe all particle interactions in the observer rest frame. However, for some particle interactions it is useful to calculate the properties of a particle in the initial particle rest frame. The four-momentum vector of a particle in the proton rest frame is described by

$$P = \begin{pmatrix} E/c \\ \vec{p} \end{pmatrix} = \begin{pmatrix} E/c \\ p_{x} \\ p_{y} \\ p_{z} \end{pmatrix}$$
 (2.27)

with total energy  $E = \gamma mc^2$ . Let a particle now move in S' with respect to a proton rest frame in S. The four-momentum vector for a particle in the proton rest frame S can be described by considering the Lorentz-transformation in Eq. (2.25) as

$$\begin{pmatrix}
E'/c \\
p'_{x} \\
p'_{y} \\
p'_{z}
\end{pmatrix} = \Lambda \cdot \begin{pmatrix}
E/c \\
p_{x} \\
p_{y} \\
p_{z}
\end{pmatrix}.$$
(2.28)

Thus, the energy transformation can be calculated, where  $\vec{\beta}$  describes the relative velocity given in spherical coordinates

$$\vec{\beta} = \begin{pmatrix} v_x/c\cos(\theta)\sin(\phi) \\ v_y/c\sin(\theta)\sin(\phi) \\ v_z/c\cos(\phi) \end{pmatrix} . \tag{2.29}$$

With  $\gamma_p$  being the Lorentz factor for the protons, the particle energy can be calculated according to

$$E'/c = \gamma_{\rm p}(E/c - \vec{\beta} \cdot \vec{p}) = \gamma_{\rm p}(E/c - \cos(\Psi)|\vec{\beta}||\vec{p}|), \tag{2.30}$$

where  $\cos(\Psi)$  describes the angle between the two moving inertial systems in the rest frame. The momentum of the particle can be rewritten by considering the relativistic energy-momentum relation  $E^2 = c^2 p^2 + m^2 c^4$  and a useful relation for a particles energy in the proton rest frame can be written as

$$E' = \gamma_{\rm p} \left( E - \cos(\Psi) |\beta| \sqrt{E^2 - m_0^2 c^4} \right). \tag{2.31}$$

For interactions, Lorentz invariant quantities are useful to describe the energy and momentum transfer. Threshold energies for scattering processes can be calculated by minimizing the Lorentz invariant center-of-mass (CM) energy  $\sqrt{s}$  for a 2  $\rightarrow$  2 - scattering process

$$s = (p_1 + p_2)^2 = (p_3 + p_4)^2,$$
 (2.32)

with  $p_i = (E_i/c, \vec{p}_i)$ ,  $i \in \{1, 2, 3, 4\}$  describing the four momentum of the particles. Four momentum conservation holds such that in the CM it follows for the three momentum

$$\vec{p}_1 + \vec{p}_2 = \vec{p}_3 + \vec{p}_4 = 0. \tag{2.33}$$

Combining these equations, yields for the CM energy

$$s = E_1^2 + E_2^2 + 2E_1E_2(1 - 2\cos(\theta_{12})c |\vec{\beta}_1| |\vec{\beta}_2|)$$
  
=  $E_3^2 + E_4^2 + 2E_3E_4(1 - 2\cos(\theta_{34})c |\vec{\beta}_3| |\vec{\beta}_4|).$  (2.34)

where  $\vec{\beta}_i = \vec{p}_i/E = \vec{v}_i/c$ ,  $i \in \{1, 2, 3\}$  describes the relative velocity of the respective particle and  $\theta_{ij}$  is the angle between the scattering particles.

#### 2.5 Particle Acceleration

To explain the Cosmic Ray spectrum, Fermi was the first who introduced 1949 [22] a particle acceleration process based on the presence of magnetic clouds that can reflect charged particles. Until today, it is common to expect high-energy particles to be accelerated at magnetic fields that are ambient both in the interstellar medium and in the circumference of astrophysical sources. Therefore, in the following section the Fermi acceleration mechanism is introduced and applied to two important acceleration mechanisms that may play a crucial role in the neutrino production in Cygnus X-3.

In general, charged particle acceleration both in electric and magnetic fields can be described by

$$\frac{\mathrm{d}}{\mathrm{d}t}(\gamma mv) = e(\vec{E} + \vec{v} \times \vec{B}). \tag{2.35}$$

As the most astrophysical plasmas have high conductivity, static electric fields can not exist as charged particles move and short-circuit the electric field. Therefore, either non-stationary electric fields or time-varying magnetic fields that induce an electric field can accelerate particles, following Maxwell's Equation  $\nabla \times \vec{E} = -\partial \vec{B}/\partial t$  [2].

#### 2.5.1 Fermi Acceleration

Fermi proposed a stochastic scenario where charged particles are reflected by magnetic irregularities. The particles gain energy on average in a stochastic process and, if they remain in the acceleration region long enough, they can be sufficiently accelerated so that the particle spectrum can be described by a power law. Here, the mathematical description of Fermi acceleration follows Ref. [29].

In the following, magnetized clouds of arbitrary size act as magnetic mirrors. Let a magnetic mirror have a non-relativistic motion with  $v_{\rm m}\ll c$  in arbitrary direction and interact with a relativistic charged particle by elastic collision. The mass of the magnetic cloud is infinitely large, leading to a constant magnetic cloud velocity during the collision.

The observers frame is at rest and values in the magnetic mirror frame are marked with primed values. Due to the elastic collision, energy is conserved and in the observer frame  $E_i' = E_f'$  holds. If a charged particle enters the magnetic cloud with  $P_i(E_i, \vartheta_i, ...)$  it is isotropized due to the inherent turbulence. As a result it leaves the magnetic cloud with an arbitrary final angle as  $P_f(E_f, \vartheta_f, ...)$ . The initial particle properties are labeled with index i and the final particle properties labeled with index f. For the initial energy in the cloud reference frame holds

$$E_i' = \gamma_{\rm m} E_i \left( 1 - \frac{v_{\rm m}}{c} \cos(\theta_i) \right) \tag{2.36}$$

where already initially ultra-relativistic particle with E = pc is assumed and magnetic cloud Lorentz factor  $\gamma_{\rm m} = 1/\sqrt{1-v_{\rm m}^2/c^2}$ . In the galactic frame, the final particle energy and momentum can be written as

$$E_f = \gamma_{\rm m} E_f' \left( 1 + \frac{v_{\rm m}}{c} \cos(\vartheta_f) \right) \tag{2.37}$$

Now, the conserved properties can be rewritten and by inserting Eq. (2.36) in Eq. (2.37), an expression for the final energy of the particle in the observer frame is given as

$$E_f = \gamma_{\rm m}^2 E_i \left( 1 - \frac{v_{\rm m}}{c} \cos(\theta_i) \right) \left( 1 + \frac{v_{\rm m}}{c} \cos(\theta_f') \right). \tag{2.38}$$

It is important to note that, since the process is stochastic, the average energy gain,

$$\frac{\Delta E}{E} = \frac{E_f - E_i}{E_i} = \frac{E_i (\gamma_{\rm m}^2 (1 - \frac{v_{\rm m}}{c} \cos(\theta_i)) (1 + \frac{v_{\rm m}}{c} \cos(\theta_f')) - 1)}{E_i}$$
(2.39)

is dependent upon the interaction angles. The expression can be simplified by taking into account the isotropic nature of the particles in the cloud, which results in  $\langle \cos(\theta_f) \rangle = 0$ . Furthermore, the initial angle is proportional to the relative velocity

$$v_{\rm rel} = c - v_{\rm m} \cos(\theta_i) = c \left( 1 - \frac{v_{\rm m}}{c} \cos(\theta_i) \right),$$
 (2.40)

if the magnetic cloud distribution is uniform. Thus, for the mean initial angle it holds

$$\langle \cos(\theta_i) \rangle = \frac{\int_{-1}^{1} \cos(\theta_i) v_{\text{rel}} d\cos(\theta_i)}{\int_{-1}^{1} v_{\text{rel}} d\cos(\theta_i)} \simeq \frac{-v_{\text{m}}}{3c}$$
(2.41)

By using Eq. (2.39) and inserting Eq. (2.41), the average energy gain can be described as

$$\left\langle \frac{\Delta E}{E} \right\rangle = \frac{\left(1 - \frac{v_{\rm m}}{c} \cos(\theta_i)\right) - \left(1 - \left(\frac{v_{\rm m}}{c}\right)^2\right)}{1 - \frac{v_{\rm m}}{c}} = \frac{\left(\frac{v_{\rm m}}{c}\right)^2 + \left(\frac{v_{\rm m}}{c}\right)^2 \frac{1}{3}}{1 - \frac{v_{\rm m}}{c}} \simeq \frac{4v_{\rm m}^2}{3c^2}.$$
 (2.42)

A particle gains energy proportional to the squared velocity and therefore this is referred to as second order Fermi acceleration.

#### 2.5.2 Diffusive Shock Acceleration

A shock is a discontinuity that spreads as a surface through a medium. The shock front moves at a speed  $v_2$  and in the rest frame of the shock there is a downstream flow in the direction of the shock front and an upstream flow that moves away from the shock front. In the following, only non-relativistic shocks are described, following the explanations in Ref. [2].

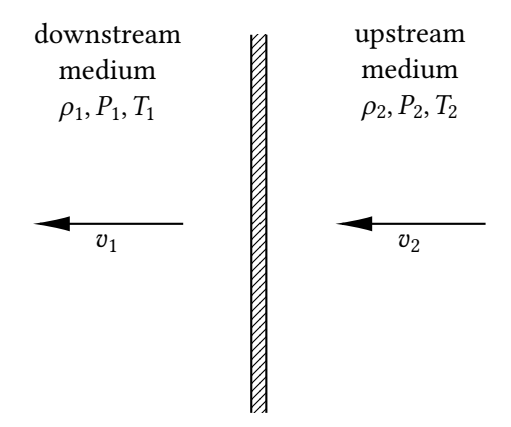


**Figure 2.4:** Sketch of the shock, with the shock front as a surface dividing the medium into a downstream and an upstream medium with their respective characteristics.

The characteristics of the shock and the surrounded medium can be described by fundamental conservation laws in fluid dynamics. In this case, the mass flow as well as the momentum flow and the energy flow through the shock surface can be described by the continuity equations

$$\rho v = 0,$$
 $P + \rho v^2 = 0,$ 
 $v(u + P + \frac{\rho v^2}{2}) = 0.$ 
(2.43)

Here, P represents the local pressure,  $\rho$  the local density v denotes the absolute value of the velocity  $\vec{v}$ . The internal energy per unit volume u can be expressed using the adiabatic index  $\gamma$ , which is considered to be constant on both sides, as  $u = P/(1 - \gamma)$ . Based on this considerations, the Rankine-Hugoniot jump conditions can be derived, which describe the medium around the shock

$$\rho_1 v_1 = \rho_2 v_2, \tag{2.44}$$

$$P_1 + \rho_1 v_1^2 = P_2 + \rho_2 v_2^2, \tag{2.45}$$

$$\frac{\gamma}{\gamma - 1} \frac{P_1}{\rho_1} + \frac{1}{2} v_1^2 = \frac{\gamma}{\gamma - 1} \frac{P_2}{\rho_2} + \frac{1}{2} v_2^2. \tag{2.46}$$

In the rest frame of the medium,  $v_2$  is the shock front velocity, while  $v_2 - v_1$  is the speed of the shocked medium. The setting in Cygnus X-3 requires strong shocks  $v_2 \gg c_s$  where the unshocked medium can be assumed as cold  $T \sim 0$  with  $P_1 = 0$ . The compression ratio is defined as  $R = v_2/v_1$  [30] for non-relativistic moving shocks and in the case of strong shocks in a medium with isotropic density  $R \to 4$ . As a result, the downstream velocity relative to the shock front equals  $v_1 = v_2/4$  and the upstream medium flows with relative velocity  $v_2 = v_s$  [30].

In astrophysical shocks, particles are accelerated by diffusive shock acceleration, which is considered to be collisionless, since the particles scatter on the magnetic field. The magnetic field can be described homogeneously on large scales, however small scale irregularities exist with sufficient strength to function as magnetic mirrors for high energetic particles.

The energy gain for a particle crossing the shock front can now be described using the considerations for the second order Fermi mechanism. The additional geometrical considerations follow M. Longair [2]. In the rest frame of the shock, the upstream gas traverses the shock in the x-direction at shock velocity  $v_s$ . As a result, the relativistic particle energy can be written as

$$E' = \gamma v_{\rm m} (E + v_{\rm s} p_{\rm r}), \tag{2.47}$$

where  $p_x$  describes the momentum with respect to the shock front, and since the shock is non-relativistic,  $\gamma v_{\rm m} \approx 1$ . Now the particle is relativistic and so it holds for the energy E = pc. This results in an energy change per crossing of

$$\left\langle \frac{\Delta E}{E} \right\rangle = \frac{v_s}{c} \cos(\vartheta). \tag{2.48}$$

Comparing this with the results for the second order Fermi shock acceleration, the geometry of a planar shock is different. The average angles  $\langle \cos(\theta_i) \rangle$  and  $\langle \cos(\theta_f) \rangle$  of the particle are different due to the different geometry. Since the particle has to cross the shock to gain energy, the particle velocity has to be projected in the direction of the shock normal. This gives a probability that the

particle will cross the shock  $p_{\text{crossing}} \sim \cos(\vartheta) d\Omega$ . The mean value for the angle can be calculated by analogy with the Eq. (2.41), which leads to

$$\langle \cos(\theta) \rangle = \frac{\int \cos^2(\theta) \sin(\theta) d\theta}{\int \cos(\theta) \sin(\theta) d\theta} = \frac{-\frac{\cos^3(\theta)}{3} \Big|_{\theta_{\min}}^{\theta_{\max}}}{-\frac{\cos^2(\theta)}{2} \Big|_{\theta_{\min}}^{\theta_{\max}}}.$$
 (2.49)

Furthermore, the geometric considerations for a planar shock include that a charged particle from the upstream medium can only cross the shock for  $\vartheta \in [\frac{\pi}{2},\pi]$  and for a particle from the downstream medium to the upstream medium  $\vartheta \in [0,\frac{\pi}{2}]$ . It is finally evident that the mean angles are expressed as  $\langle \cos(\vartheta_{i,f}) \rangle = \mp \frac{2}{3}$ . Taking this into account, the resulting energy change for a particle passing through the shock is

$$\left\langle \frac{\Delta E}{E} \right\rangle = \frac{2}{3} \frac{v_{\rm s}}{c}.\tag{2.50}$$

Since the energy gain scales linearly with the relative velocity of a particle changing from the upstream to the downstream medium, this acceleration mechanism is called first-order Fermi acceleration. The different velocities of the upstream and downstream media of a shock result in an acceleration mechanism based on the energy change in different frames, as predicted by Fermi acceleration.

### 2.5.3 Magnetic Reconnection

Magnetic reconnection manifests as a topological deformation of turbulent magnetic fields. In ideal magnetohydrodynamic theory (MHD), magnetic field lines are frozen in the fluid at the limit of large magnetic Reynolds numbers. This means that the magnetic field lines move with the speed of the plasma as  $v = c\vec{E} \times \vec{B}/B^2$ . The existence of magnetic reconnection therefore implies a deviation from the ideal MHD.

There is considerable empirical evidence for the occurrence of magnetic reconnection. However, the microscopic mechanism is not yet fully understood. Therefore, in the following, a rough overview of a general magnetic reconnection description is given.

Historically, magnetic reconnection was first introduced to explain solar flares. Today, magnetic reconnection is associated with several astrophysical objects that are surrounded by highly conductive fluids and produce energetic particles. In circumferences where particle acceleration appears, shock acceleration is not always sufficient to describe all scenarios. Two magnetized layers reconnect and the accelerated particle spectra are described by a simple power law  $dN/dE = N_0 E^{-p}$  [31].

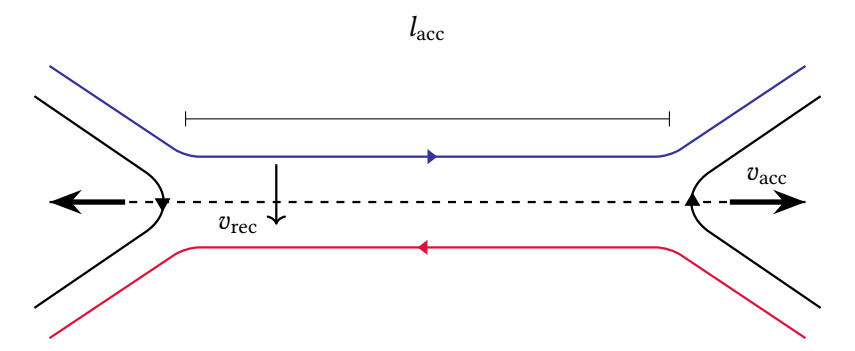


**Figure 2.5:** The Sweet-Parker model is depicted in two dimensions as a two-current-sheet configuration with infinite extension in three dimensions. The process of reconnection is characterized by a velocity  $v_{\rm rec}$ , and the region  $l_{\rm acc}$  is defined as the area where the current sheets primarily accelerate particles, resulting in a material flow  $v_{\rm acc}$  perpendicular to the reconnection velocity  $v_{\rm rec}$ .

The first model for magnetic reconnection was developed by Sweet and Parker [32, 33] and is based on two-dimensional geometry for laminar flow. Fig. 2.5 sketches the geometry of the Sweet-Parker model, where two laminar magnetic flows are separated by a small current sheet. The magnetic fields are opposed in the x-direction and reconnect in the y-direction with a reconnection velocity  $v_{\rm rec}$ , whereas the sheet extends theoretically to infinity in z direction. To ensure mass conservation, the plasma and magnetic inflow in the y-direction is balanced by a plasma outflow in the x-direction [2]. Detailed calculations of the energy dissipation can be found in Ref. [2]. They are not derived any further in this context, as this work is based on the magnetic reconnection model in de Gouveia et al. [34].

Their model is explained here qualitatively to understand the acceleration mechanism in the vicinity of Cygnus X-3. A coupled magnetic field between the black hole and the accretion disk extends the close vicinity of the system. From both the black hole and the accretion disk, the magnetic fields extend perpendicularly to the accretion disk rotation axis, leading to a configuration where the black hole and accretion disk magnetic fields can be regarded as parallel. This leads to a reconnection of the magnetic field lines with a macroscopic geometry similar to the reconnection shown in Fig. 2.5. Particles in the small current sheet are accelerated in the direction aligned with the poles of the black hole. The acceleration appears to be analogous to a magnetized shock acceleration due to the first-order Fermi mechanism.

In this approach, charged particles gain macroscopic energy by scattering off

# **Chapter 2** Foundations of High-Energy Astrophysics

microscopic magnetic irregularities, and thus the frame change causes an energy increase of  $\,$ 

$$\left\langle \frac{\Delta E}{E} \right\rangle = \frac{4}{3} \frac{v_{\text{rec}}}{c},\tag{2.51}$$

while the magnetic field lines move towards each other at the speed  $v_{\rm rec}$ .

This chapter provides a detailed description of the main characteristics of Cygnus X-3, such as the geometry, the ambient particle fields and the magnetic field, which are included in the numerical simulations. In addition, the scenario based on stellar wind and jet interactions is introduced by developing the two different acceleration regions  $S_1$  and  $S_2$ . The geometry of the system is then defined in detail in order to study the orbital modulation. In addition to the proposed qualitative scenario, measurement data are used to study the surrounding particles.

Cygnus X-3 is a high-mass X-ray binary with an estimated distance of about  $d=7-10\,\mathrm{kpc}$  emitting hard and soft X-rays with high variability. In addition, Cygnus X-3 exhibits strong radio emission associated with a jet-like structure and is one of the strongest radio sources among the known X-ray binaries. Since Cygnus X-3 shows outbursts in form of relativistic radio jets ( $v\sim0.81\,c$  in the regime of 0.1 Jy [6]), this system can be classified as a microquasar. It also radiates in the infrared spectrum with a modulated amplitude by the companion, which is known to be a Wolf-Rayet star. The compact object can be either a black hole or a neutron star, however, a black hole is more likely [6] and thus a black hole orbiting a Wolf-Rayet star is considered in this work.

#### 3.1 Mass

The total mass of the binary system is still being investigated and is subject to some uncertainties. In addition, it is challenging to predict whether the compact object is a neutron star or a black hole. Based on infrared observations, it is well known that the central object is a Wolf-Rayet star [35]. Therefore, a lower and an upper limit is given for the central object. Masses for Wolf-Rayet stars can be calculated based on luminosity measurements and for Wolf-Rayet star measurements in binary systems a broad mass range of  $M_{WR} \sim (10-83) M_{\odot}$  can be found [36]. Furthermore, the minimum mass of a black hole is in the range of  $(3-5) M_{\odot}$  [37].

Based on this mass ranges for the objects in the binary system, Kepler's third law

$$a^3 P^2 = \frac{G(M_1 + M_2)}{4\pi^2} \tag{3.1}$$

can be applied assuming an ideal two-body interaction [38]. Thus, the orbital separation is linked to the stellar mass  $M_{\rm WR}$  and compact object mass  $M_{\rm BH}$  as

$$a = 9.989 \times 10^{10} \left( \frac{M_{\rm BH} + M_{\rm WR}}{M_{\odot}} \right)^{1/3} \text{ cm.}$$
 (3.2)

Furthermore, the black hole mass is expected to be much smaller than the Wolf-Rayet mass and thus  $M_{\rm BH} \ll M_{\rm WR}$ . As a result, the black hole orbits the Wolf-Rayet star and it is an appropriate condition to choose the masses such that the barycenter

$$r_{\rm B} = \frac{aM_{\rm BH}}{M_{\rm WR} + M_{\rm BH}} \tag{3.3}$$

is located inside the Wolf-Rayet star. Corresponding to the orbital separation and the later introduced jet geometry, the masses are chosen to be  $M_{\rm WR}=50\,M_{\odot}$  representing the Wolf-Rayet mass and  $M_{\rm BH}=20\,M_{\odot}$  [39] representing the black hole mass leading to  $a=4\times10^{10}$  cm. The orbital separation is small enough to lead to the implication that the stellar winds of the Wolf-Rayet star, which mainly contain helium, completely envelop the compact object.

# 3.2 Geometry

In the following, the Wolf-Rayet star in Cygnus X-3 is defined as the origin of the coordinate system. The radius of the Wolf-Rayet star is  $R_{\rm WR}=6\times10^{10}$  cm [6] and for the compact object, the Schwarzschild radius is given as  $R_{\rm S}=5.9\times10^6$  cm.

Cygnus X-3 has a radio jet causing massive radio outbursts with transient  $\gamma$ -ray emission. The jet axis is close to the line of sight with  $\vartheta_{\rm BH} \lesssim 14^{\circ}$ , neglecting precision of the jet. The specific internal geometry is not fully understood and some scenarios are possible. A sketch of a possible geometry is taken from Ref. [39] and illustrated in Fig. 3.1. Three directions are marked by the corresponding vectors: First, the orbital vector  $\vec{d} = d\vec{e}_{\rm d}$  always points from the Wolf-Rayet star to the black hole and therefore changes with the orbital period. The vector  $\vec{r}_{\rm j} = r_{\rm j}\vec{e}_{\rm j}$  denotes the jet direction, which follows the jet line with respect to the black hole. Any point in the jet can be described by  $\vec{r}_{\rm WR}$  with respect to the Wolf-Rayet star. The described unit vectors are written as follows:

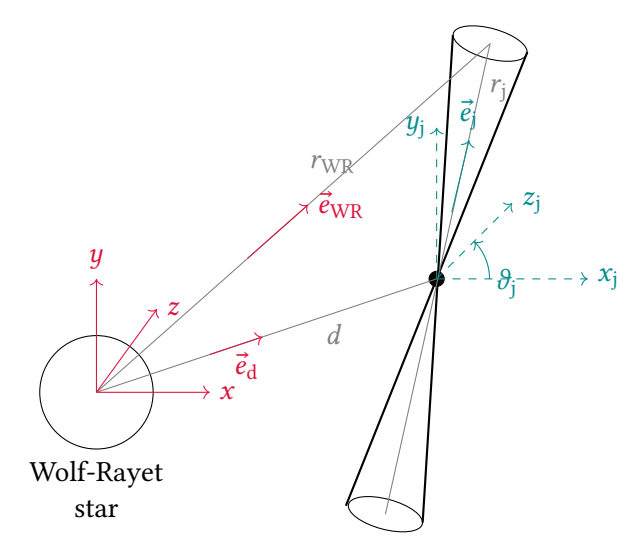


**Figure 3.1:** Sketch of the Cygnus X-3 configuration. The red colors denote the constellation with the Wolf-Rayet star in the center and the blue coordinate system represents the geometry with the black hole in the center.

$$\begin{split} \vec{e}_{\rm j} &= \begin{pmatrix} \cos(\vartheta_{\rm j}) \sin(\varphi_{\rm j}) \\ \sin(\vartheta_{\rm j}) \sin(\varphi_{\rm j}) \\ \cos(\varphi_{\rm j}) \end{pmatrix}, \\ \vec{e}_{\rm d} &= \begin{pmatrix} \cos(\theta) \\ \sin(\theta) \\ 0 \end{pmatrix}, \\ \vec{e}_{\rm WR} &= \frac{1}{r_{\rm WR}} (d\vec{e}_{\rm d} + r_{\rm j}\vec{e}_{\rm j}) = \frac{1}{r_{\rm WR}} \begin{pmatrix} r_{\rm j} \cos(\vartheta_{\rm j}) \sin(\varphi_{\rm j}) + d \cos(\theta) \\ r_{\rm j} \sin(\vartheta_{\rm j}) \sin(\varphi_{\rm j}) + d \sin(\theta) \\ r_{\rm j} \sin(\vartheta_{\rm j}) \end{pmatrix}. \end{split}$$

A circular motion of the compact object around the Wolf-Rayet star is considered [8]. For simplicity, it can be assumed that the observer is located directly in the jet direction  $\vec{e_j}$ . Disregarding precession,  $\theta_j = 9^\circ$  and  $\phi_j = 31^\circ$  is taken due to the calculations for orbital modulation in Ref. [39]. Since the jet axis is fixed relative to the black hole, the orbital modulation of the signal has to be considered and the orbital phase  $\theta$  is thus a free parameter in the simulation. Due to the assumption that the observer is located in the jet, the jet axis is as close as possible to the Wolf-Rayet star in the superior conjunction. A sketch of how

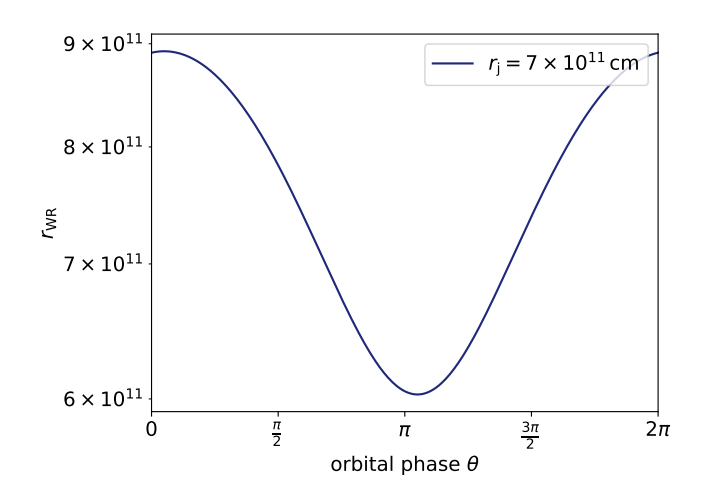


**Figure 3.2:** Distance to Wolf-Rayet star  $r_{\text{WR}}$  for distance in jet  $r_{\text{j}}$  depending on orbital phase. The inferior and superior conjunctions are close to  $\theta = 0$  and  $\theta = \pi$  respectively.

the inferior and the superior conjunction are configured is illustrated in Fig. 3.3. The three-dimensional geometry of the system leads to non-trivial angles  $\theta$  for superior and inferior conjunction. These can be considered by taking a distance in the jet (here  $r_{\rm j}=7\times10^{11}$  cm) and examining the minimum and maximum  $r_{\rm WR}$  as visualised in Fig. 3.2. It can be seen that for first considerations of the phase effect it is valid to take the orbital phase  $\theta=0$  for the inferior conjunction and  $\theta=\pi$  for the superior conjunction.

# 3.3 Photon Spectrum

Cygnus X-3 is an accreting binary system and therefore emits a significant amount of non-thermal radiation in the X-ray spectrum. It undergoes massive radio outbursts that exhibit a jet-like structure. The radio emissions as well as the X-ray emissions undergo significant variations. Furthermore, gamma-ray emission can occasionally be detected in association with a particular state. In addition to an orbital modulation, the X-ray spectrum can be divided into distinct states [40].

In general, photons with energies between 100 eV and 100 keV are classified as X-rays. Due to the broad energy range, high-energetic X-ray photons are referred to as hard X-rays and lower energy X-ray photons are soft X-rays [2]. The crucial coupling between accretion and emission in microquasars can be understood by analyzing the spectrum of a classical outburst evolution.

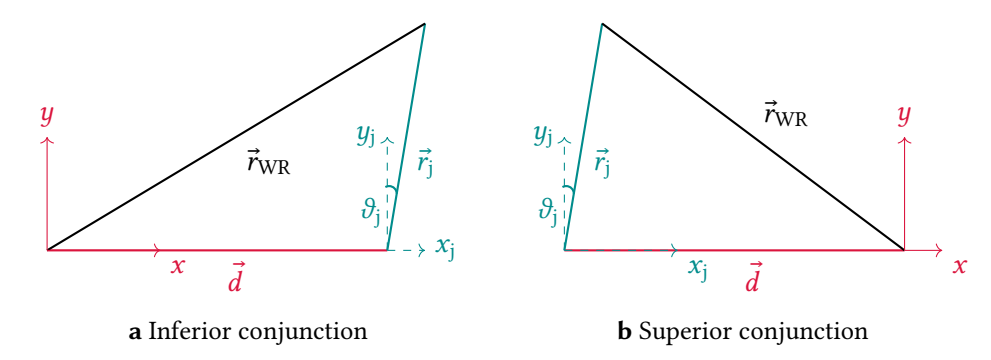


**Figure 3.3:** Two-dimensional geometry at two extreme configurations of interior conjunction and superior conjunction. The system is investigated here two dimensional with the observer is located in the jet opening angle.

Since the photon spectra of microquasars have a fast variability, there are several classifications for the different temporal spectral characteristics. One of the first attempts to classify the spectrum was made by M. A. Nowak [41] based on observations of high-energy measurements of black holes. He defined five distinct states based on the mass accretion rate  $\dot{M}$  of the compact object. As  $\dot{M}$  increases, the system evolves from a low/hard state through an intermediate state to a high/soft state. For some systems there exists a very high state and the final state is always the quiescent state. These states can be distinguished by measuring their energy and power spectra and follow a q-shaped line in the respective Hardness Intensity Diagram (HID), which is illustrated in Fig. 3.4 [42].

In general, these states can be distinguished by their X-ray spectrum. Cygnus X-3 is a special case, since the classification for the radio states [42] does not apply to the X-ray states. A more general classification for X-ray spectra can be found in [43], but a rough overview of the combined X-ray and radio emission states for Cygnus X-3 is given below [40]:

- Low/Hard state (LH) with a compact radio jet. Lots of X-ray radiation is produced, described by a power law and limited to a cut-off energy of 100 keV.
- *Intermediate state (IS)* shows a steep power-law spectrum with no cut-off

energy and a characteristic thermal disk spectrum. This state is defined as occurring as a transition between the LH and HS states.

- *Very High state (VHS)* occurs in the same spectral region as the IS but with significantly higher intensities.
- *High/Soft state (HS)* is the state in which radio flaring typically occurs. The general state is dominated by a thermal photon spectrum and no or less power-law radiation.
- *Quiescent state* (*QS*) is characterized by a hard power-law spectrum, where both the radio source flux and the X-ray flux are very low.

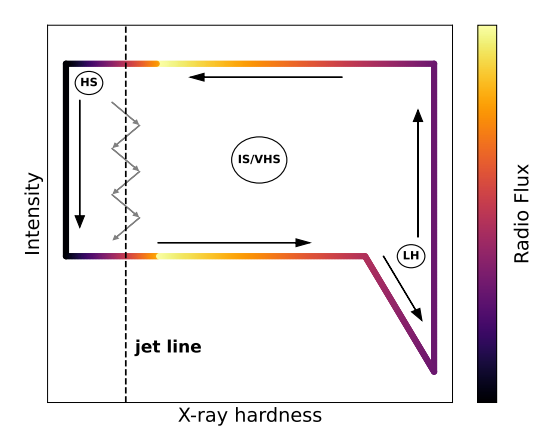


**Figure 3.4:** Sketch of a HID showing the general shape of microquasar radiation with the color plot marking the radio flux. The different canonical states of microquasars are labeled as well as the jet line.

It is common to plot the photon spectrum on a HID to analyze the spectral evolution of the system. QS is not shown in the diagram as no or very low intensity is measured in this state. The other four states mentioned above are marked on the characteristic curve in the diagram. Due to the complexity of Cygnus X-3, the color plot is used to show the associated radio emissions. Note that the jet line marks the transition from possible jet onset to jet suppression. As Cygnus X-3 evolves from HS to VHS, it produces large flares and jet onset is possible.

There is one state that has not yet been mentioned due to the fact that it is very characteristic of Cygnus X-3. This is the so-called hypersoft State (HyS), which

is a particularly extreme case of HS. The incoming X-rays are particularly soft and no radio radiation can be observed. In this state there is no flaring and the jet is off. In this state, gamma-ray emission can occasionally be observed, followed by an intense outburst whose evolution is described in detail in the following section. This work focuses on the two extreme states of Cygnus X-3, on the one hand the HyS with very soft X-ray at high intensity and no radio emission, and on the other hand the LH with low intensity hard X-ray and some radio flaring.

Since outbursts with jet-like structure are not stationary, the system occasionally rests in the quiescent state. The magnetic field around the accretion disk causes weak mass loss and during this state radio photons are only emitted by relativistic electrons without any jet structure. The system starts flaring in the high hard state, where the intensity increases. A HID for Cygnus X-3 is described in further detail in Ref. [40], where the six different spectral states, which are defined for Cygnus X-3, are described. The HID for those six different states is presented in Fig. 3.4, where this work focuses on the hypersoft state and the Hard state. Since the aim is to investigate neutrino production in the vicinity of Cygnus X-3, only states with a jet structure are important to be considered.

### 3.4 Outburst Evolution Scenario

When high-energy particles interact, a variety of secondary particles is produced. The long-living and less interacting particles are able to reach Earth. Initially accelerated protons may escape the acceleration region and, in the case of Cygnus X-3, are part of the galactic cosmic ray spectrum. Among the escaping particles, neutrinos are of particular interest because they interact only via the weak force and are therefore almost always the only carriers from regions of high density. In addition, high-energy  $\gamma$  rays can be produced, which can escape only if the opacity is low enough. A more detailed description of the interaction mechanisms for the initial proton and the resulting secondary particles follows in Chapter 4.

A scenario for the high variability of the spectrum of Cygnus X-3 is presented below, based on the mass loss rate of the Wolf-Rayet star and the resulting changes in the mass accretion rate. The relevant theory for accretion disks, jet launching mechanisms and general particle acceleration is explained in more detail in Chapter 2.

The generic model explained here for the spectral behavior of Cygnus X-3 was introduced by Fender et al. [42] and developed by Koljonen et al. [8]. Let the system be in QS, where the Wolf-Rayet star goes through a phase of increased mass loss rate. As a result, more thermal electrons are ambient in the tight surroundings of the compact object, and thus the jet-launching mechanism is

#### **Chapter 3** Cygnus X-3

quenched to a low level. Now the jet is almost switched off, barely weak enough to cause a small radio emission, which is measured in this state. In addition, the increased mass loss rate leads to an increased density of thermal electrons in the vicinity of the compact object. These thermal particles mix with the relativistic particles, causing the medium to become opaque to both the emitted synchrotron radiation and the radio emission. Finally, quenched radio emission appears, and the ambient thermal particles enhance the infrared radiation.

Increased mass loss also increases the rate of mass accretion into the black hole, leading to the characteristic hard X-ray spectrum in this state. As a result, an increase in the magnetic pressure in the inner disk region appears, which implies a massive injection of particles into the jet. The jet is fed by the accretion disk, and once the mass loss rate from the Wolf-Rayet star returns to a lower level, the jet begins to flare until it reaches the soft state. Here, no or only a little mass is transferred from the inner part of the accretion disk to the jet, and so the hard X-ray emission decreases while the density reaches levels where the soft X-rays from the accretion disk dominate the spectrum. Finally, the system remains in the quiescent state until the mass loss rate of Cygnus X-3 increases again.

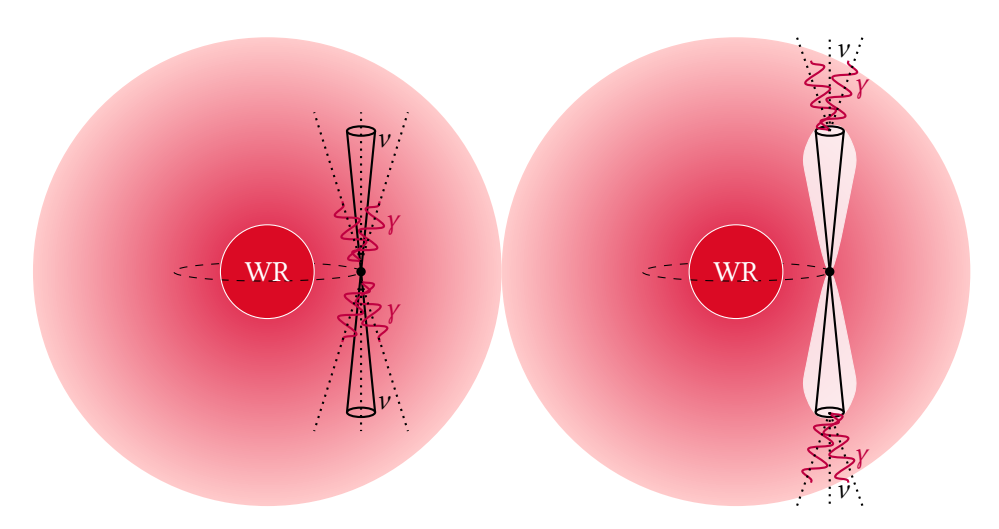


**Figure 3.5:** Sketch of the two jet state scenarios. On the left, the jet has switched on right after the quiescent state, interacting with the surrounding medium close to the black hole  $(S_1)$ . The right side shows the state when the jet has been on for a long time and has worked against the Wolf-Rayet medium, forming a cocoon  $(S_2)$ .

Considering the non-continuous jet in the dense wind of the Wolf-Rayet companion, it can be concluded that in the quiescent state the wind density around the black hole is unaffected by its presence. Hence, the wind density can be taken

as constant in each spherical element. The protons, which are accelerated in an outburst, interact close to the black hole with the ambient medium.

The jet and its interaction with the surrounding medium is examined in more detail when it comes to the jet evolution of the system. In the following, the jet is initiated after the quiescent state and thus the first point of interaction is close to the compact object, assumed at  $10\,R_{\rm S}$  based on Ref. [44]. In addition, as the jet begins, it acts against the stellar wind material and the medium around the black hole is pushed outwards, forming a cocoon structure and leaving behind a cavity of much lower density. The cocoon grows outwards during a period of stable jet propagation. If the continuous jet persists long enough, the relativistic protons in the jet begin to interact significantly with the stellar wind material at the outer sphere of the ejected cocoon. At the given distance, both the proton density and the magnetic field are distinctly different from those at the initial interaction point near the black hole.

The significant decrease in radio emission suggests that the jet is weakening or shutting down, leaving the cocoon structure behind. Subsequently, a pressure gradient causes the surrounding stellar wind to refill the cocoon in the Hys and QS. This means that the next time the jet is launched, the point of interaction of the relativistic protons in the jet with the non-relativistic stellar wind will again be close to the compact object. Stronger magnetic fields and higher densities are found in the immediate vicinity of the black hole. As mentioned above, both protons and secondary interaction mechanisms are affected.

The overall picture is one of two possible distinct interaction and acceleration regions, one at the beginning of the continuous jet launch phase at the QS to HS transition close to the compact object, and one further out when a cocoon has formed at the HS to Hys transition. This leads to different photon but also neutrino spectra at these points.

If the jet sets on again before the stellar wind fills back the cocoon structure, the proton acceleration and the interaction region is shifted to the end of the cocoon structure. The protons experience at this distance different magnetic fields and particle densities and thus distinct maximum particle energies and resulting secondary spectra are possible.

Based on these assumptions, the resulting particle energy spectra are considered later for the two different scenarios illustrated in Fig. 3.5. In the following,  $S_1$  refers to the acceleration region close to the black hole, which is associated with the scenario of the onset of the jet after the wind material has refilled the vicinity of the black hole. Consequently, the protons interact immediately with the surrounding stellar wind material at  $10\,R_{\rm S}$ .  $S_2$  describes the proton interaction at the end of the cocoon due to a continuous jet and thus a long phase of cocoon formation. It is evident to assume that the cocoon elongation

#### Chapter 3 Cygnus X-3

corresponds to twice the orbital separation after a certain period of time and together with the calculations made in Ref. [39], the acceleration region in  $S_2$  is chosen to be at  $7 \times 10^{11}$  cm. As outlined in Section 2.5, two distinct acceleration mechanisms can occur in astrophysical environments. In the vicinity of the black hole, the acceleration scenario corresponds to the theory of de Gouveia Dal Pino and Lazarian [34], as employed by Khiali et al. [45]. Reconnection, in this context, manifests exclusively in the proximity of the black hole, and thus, solely in  $S_1$ . In the following,  $S_2$  refers to the acceleration region at the extended jet, considering only the shock acceleration. However, it is important to note that even if the cocoon structure has already developed, both the accretion disk and the stellar wind can provide enough material to reach the vicinity of the black hole. Consequently, if  $S_2$  has evolved, there may be two acceleration regions, with one acceleration region close to the black hole and another at  $7 \times 10^{11}$  cm. Note that unless otherwise stated, the focus of  $S_2$  is on the shock acceleration at the cocoon edge.

Since the jet in Cygnus X-3 propagates at relativistic velocities, it is necessary to evaluate the contribution of relativistic effects. The jet velocity is assumed to be the same for both jets. However, the literature does not provide a clear picture of the general jet velocity. It ranges from weakly relativistic velocities of  $v \le 0.3 c$  [46] to higher relativistic velocities of  $v \ge 0.8 c$  [47]. It is important to note that the Lorentz boost leads to Doppler-shifted and non-isotropic photon spectra. Furthermore, the jet opening angle and the particle energies are Lorentz-boosted. A brief introduction to relativistic effects is given in Section 2.4, with explicit references to Ref. [27] for a detailed discussion of the implications for relativistic velocities. In the configuration of Cygnus X-3, different interaction frames have to be considered. Since the scope of this thesis focuses on the general ability of Cygnus X-3 to accelerate particles, it is assumed here without calculation that particles from the counter-jet are Doppler-boosted so efficiently that they make no first-order contribution to the particle spectra on Earth. Therefore, the counter-jet is not considered further. The jet is assumed to propagate relativistically, but it is noted here that properties experience relativistic effects without being calculated in detail. This leads to isotropic assumptions for particle spectra and non-relativistic shock estimates.

# 3.5 Magnetic Field

The ambient magnetic field in the acceleration region is a crucial parameter for the further investigation of the particle interaction (see Chapter 4). In a first approach, a magnetic field is assumed and the considerations for the magnetic field of Cygnus X-3 follow J.C.A. Miller-Jones et al. [44]. The particle accelera-

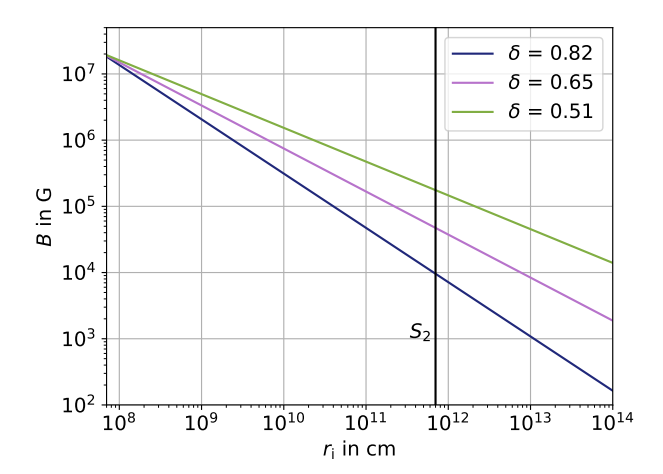


**Figure 3.6:** Magnetic field strength B depending on distance of particle to the black hole  $r_j$  calculated for different  $\delta$ . The distance of the acceleration region at the edge of the cocoon structure is marked as  $S_2$ , the magnetic field in  $S_1$  equals  $B_0 = 2.1 \times 10^7$  G independent of  $\delta$  (see Eq. (3.4)).

tion region of Cygnus X-3 has different locations depending on the jet evolution. Therefore, the magnetic field has to be determined at different distances  $r_{\rm j}$  from the black hole. The magnetic field strength around the black hole can be parameterized as

$$B(r) = B_0 \left(\frac{r}{r_0}\right)^{-\delta},\tag{3.4}$$

with  $r_0$  being the jet injection point and  $B_0$  being the corresponding magnetic field. The parameter  $\delta$  depends strongly on the properties of the jet, where  $\delta$  is limited to an interval of  $0.5 < \delta < 0.83$ . Fig. 3.6 shows the magnetic field strength for different  $\delta$  as a function of the distance to the compact object  $r_j$ . Based on the considerations in Ref. [44], the jet injection occurs at  $10 R_S \approx 6 \times 10^7$  cm with an ambient magnetic field of  $B_0 = 2.1 \times 10^7$  G.

It can be seen that especially for sufficiently large distances, as is the case in  $S_2$ , the magnetic field strength is sensitive to the choice of  $\delta$ . The magnetic field strength is already chosen optimistically and based on the assumptions in Koljonen et al. [8], the magnetic field in the outer regions of the jet best corresponds to a parameter choice of  $\delta = 0.65$ .

Another important parameter is the magnetization of the medium, described by

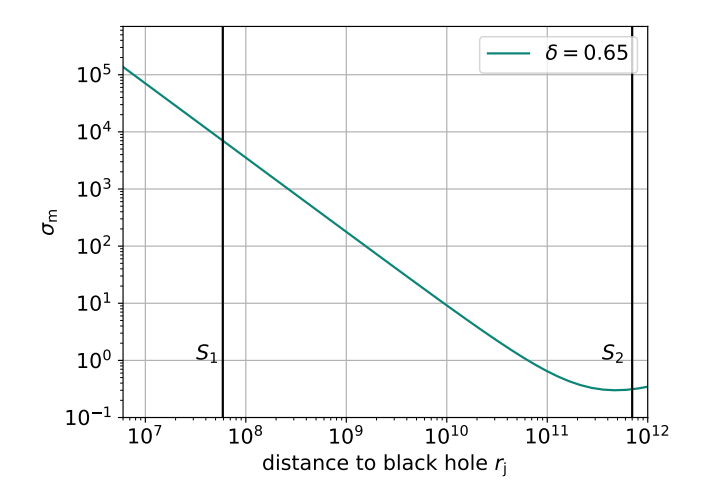


**Figure 3.7:** Magnetization parameter  $\sigma_{\rm m}$  based on the magnetic field considerations in Ref. [44] with  $\delta=0.65$  at different distances in the jet from the black hole. The distance of the acceleration region is marked for the respective regions  $S_1$  and  $S_2$ .

$$\sigma_{\rm m}(r) = B^2/(4\pi\omega(r)),\tag{3.5}$$

where  $\omega(r) = n(r)m_{\rm p}c^2$  is the enthalpy density and B is the magnetic field strength [31]. The magnetization parameter  $\sigma_{\rm m}$  relates the magnetic energy to the total energy of the particles. In weakly magnetized plasmas, particles can move efficiently and therefore the Fermi acceleration can sufficiently explain the particle acceleration with diffusive shock acceleration. In strongly magnetized plasmas ( $\sigma_{\rm m} \gg 1$ ), however, magnetic reconnection dominates [31].

Fig. 3.7 shows the magnetization parameter  $\sigma_m$  for different distances in the jet from the black hole. For this calculation, it is necessary to refer to the following section, as the magnetization depends on the proton density. The proton density depends on the distance to the Wolf-Rayet star, which is related to the distance to the black hole in the jet by Eq. (3.6). As a result, the magnetization varies strongly with  $r_j$ . For  $\sigma_m < 1$ , shock acceleration dominates, and for large plasma magnetization, particle acceleration occurs via magnetic reconnection. The markers in the plot illustrate that in  $S_1$  the plasma is strongly magnetized and magnetic reconnection is sufficient to accelerate particles. In  $S_2$ , however, the weak magnetization indicates that shock acceleration is dominant. Note that the magnetization depends on the particle density, which depends on  $r_{WR}$ , which changes significantly for jet elongations in the order of the orbital sepa-

ration thus leading to a deviation of the linear correlation in the graph at larger distances.

### 3.6 Ambient Particles

Besides the magnetic field, protons also interact with various particles. In the following, the particle densities of the initially abundant particles have to be considered in the acceleration region of the protons. Two different particle densities have to be distinguished, namely the proton density and the photon density in the region of proton acceleration.

## 3.6.1 Proton Density

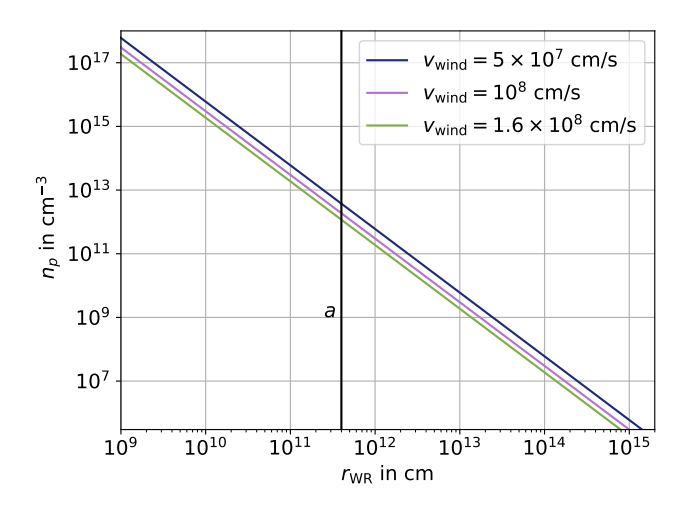


**Figure 3.8:** Density profile of stellar wind protons for different wind speeds as a function of distance from Wolf-Rayet star  $r_{\text{WR}}$ . Orbital separation is marked with a.

Cygnus X-3 contains a Wolf-Rayet star, so the dense medium created by the Wolf-Rayet wind is initially composed of helium. The giant dipole resonance is known as the phenomenon, where photons with approximate energies in the nucleus rest frame of E' = (30 - 50) MeV can cause the emission of one or two nuclei [48]. Implying an initial nucleus of <sup>4</sup>He, the emission of one or more nuclei leads to decay into single nuclei. However, there is no significant photon field ambient carrying these energies. The initial assumption of <sup>4</sup>He being accelerated leads to lower synchrotron energy loss. Nonetheless, as photohadronic interactions are considered to be the important interaction mechanism, the effect

of considering initial helium in the acceleration region leads to fractionation as a first photohadronic interaction. If helium nuclei exit the acceleration region without fractionation, they may interact with other helium nuclei in a four times less dense medium and increased cross section by a factor four. Consequently, accounting for helium introduces additional complexity with limited impact, making it common practice to assume protons for Cygnus X-3. Therefore, this work assumes that the ambient medium is composed of protons without further calculation.

The number density of protons  $n_{\rm p}$  in the circumference of the black hole can be described by the mass loss rate  $\dot{M}=10^{-5}~M_{\odot}$  [8] of the Wolf-Rayet star as

$$n_{\rm p}(r_{\rm WR}) = \frac{\dot{M}}{4\pi r_{\rm WR^2} v_{\rm wind} m_{\rm p}}.$$
(3.6)

Different stellar wind speeds have been estimated depending on the specific parameters and the calculated wind velocities are in the interval  $I_{\rm v} \sim [5 \times 10^7, 1.6 \times 10^8]$  cm/s [8]. Fig. 3.8 therefore illustrates the wind density profile for different wind velocities, and it is evident that changing the wind velocity parameter in the range of the measured velocity interval has a small effect. Thus, in the following, the stellar wind velocity is approximated by  $v_{\rm wind} = 10^8$  cm/s.

# 3.6.2 Photon Density

In the black hole's environment, photons from different sources require separate considerations, namely the thermal photons from the Wolf-Rayet star, the photons from the accretion disk and the synchrotron photons in the jet.

Since every star is an almost perfect black body, the differential photon spectrum from the Wolf-Rayet star can be described by Planck's law [22] and for the isotropic photon distribution follows

$$\frac{\mathrm{d}n_{ph}(E,T,r)}{\mathrm{d}E} = \frac{8\pi}{(hc)^3} \frac{E^2}{\exp(E/(k_{\rm B}T)) - 1} \left(\frac{R_{\rm WR}}{r}\right)^2. \tag{3.7}$$

The temperature of the Wolf-Rayet star is  $T \simeq 10^5$  K [6] and the resulting differential photon number density depends on both, photon energy and their distance. The photon spectrum can be seen in Fig. 3.10 for  $S_1$  and Fig. 3.11 for  $S_2$ . Note that the spectrum for the stellar photons depends on the distance from the Wolf-Rayet star and therefore has a minor effect with increasing distance from the jet.

The accretion disk does not emit photons with isotropic geometry requiring the differential photon density to be calculated corresponding to [49] as

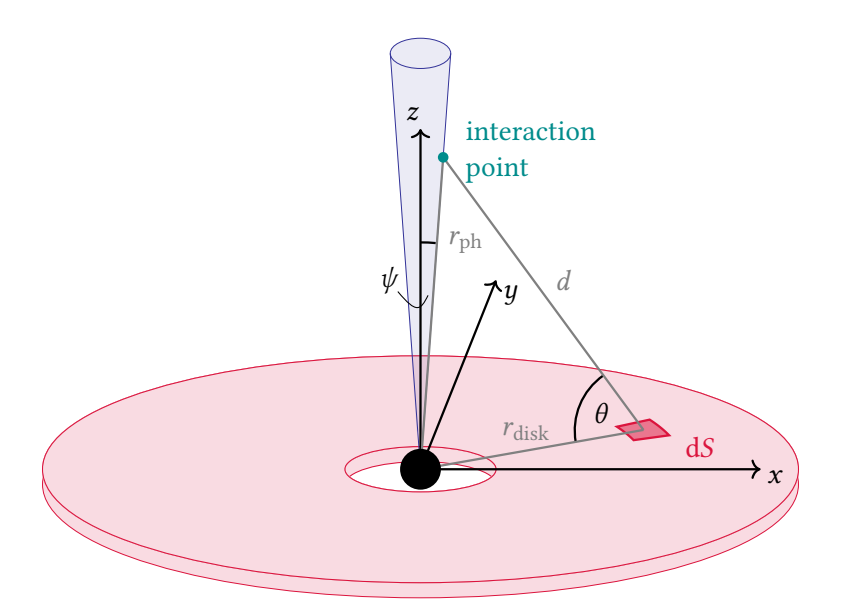


**Figure 3.9:** Sketch of a geometrically thin accretion disk with considerations that were made for the Cygnus X-3.  $r_{\rm disk}$  indicates the radius of the accretion disk element, while  $r_{\rm ph}$  denotes the position of a photon interacting in the jet with respect to the black hole.

$$\frac{\mathrm{d}n_{ph}(E,r)}{\mathrm{d}E} = \int_{\Omega_{\mathrm{disk}}} \frac{\mathrm{d}n_{\mathrm{ph}}(E,r)}{\mathrm{d}E\mathrm{d}\Omega} \mathrm{d}\Omega. \tag{3.8}$$

In Section 2.3.2, a model for the accretion disk is introduced and, considering the given temperature profile, the Planck distribution can be integrated over the disk extension to obtain the differential photon density taking into account the exact geometry for the solid angle element. The solid angle element can be obtained by considering a simplified the geometry of Ref. [49] as presented in Fig. 3.9. The surface element  $dS = r_{\rm disk} dr_{\rm disk} d\phi$  is projected in the line of sight, and

$$d\Omega = \frac{\vec{e}_{\rm d} \cdot \vec{e}_{\rm j}}{d^2} dS \tag{3.9}$$

follows. Fig. 3.9 defines  $\psi$  as the angle between the accretion disk normal and the photon with respect to the black hole  $\vec{r}_{\rm ph}$ . Thus, the maximum possible angle  $\psi$  corresponds to the jet opening angle  $\vartheta_0$ . Due to the small jet opening angle,  $\psi$  is negligibly small and the unit vector for the jet photons  $\vec{e}_j$  has only a z-component. As a result, the scalar product  $\vec{e}_d \cdot \vec{e}_j$  becomes  $\cos(\theta)$ . Substituting  $\cos(\theta)$  and d by the known parameters, namely  $r_{\rm disk}$  and  $r_j$ , gives

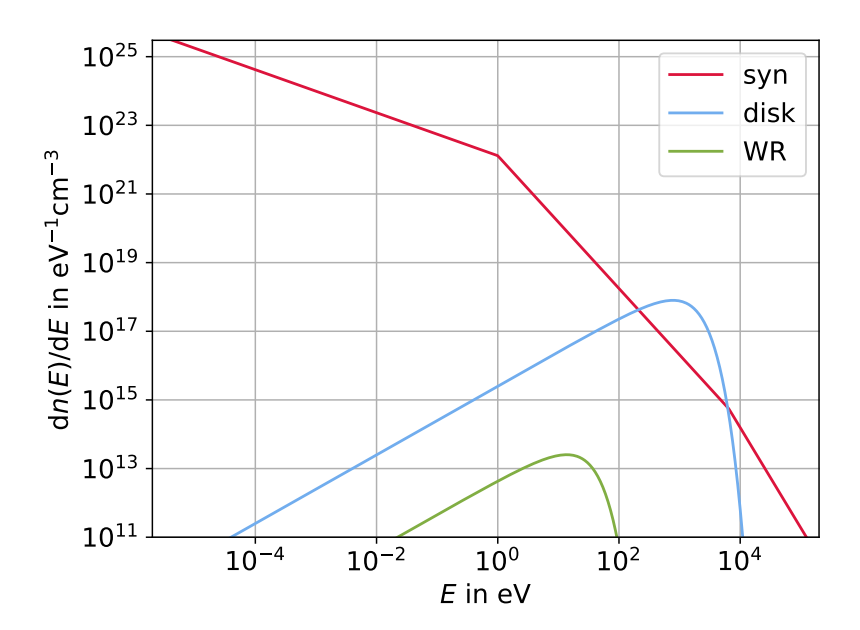


**Figure 3.10:** Photon densities ambient in the vicinity of Cygnus X-3 in  $S_1$ . Accretion disk photons (disk), stellar photons (WR) and synchrotron photons (syn) are considered with synchrotron photons exhibiting a cut-off at 1 GeV for high energies and at  $10^{-6}$  eV for low energies.

$$d\Omega = \frac{r_{\rm j}r_{\rm disk}}{(r_{\rm j}^2 + r_{\rm disk}^2)^{3/2}} dr_{\rm disk} d\phi. \tag{3.10}$$

The resulting photon density can be described by

$$\frac{\mathrm{d}n(E, r_{\rm j})}{\mathrm{d}E} = \frac{2E^2}{(hc)^3} \int_0^{2\pi} \mathrm{d}\phi \int_{r_{\rm in}}^{r_{\rm out}} \mathrm{d}r_{\rm disk} \frac{r_{\rm j}r_{\rm disk}}{(r_{\rm j}^2 + r_{\rm disk}^2)^{3/2}} \frac{1}{\exp(E/[k_{\rm B}T(r_{\rm disk})]) - 1}.$$
(3.11)

The accretion disk photon density is calculated using  $r_{\rm in} = 6\,R_{\rm S}$  and  $r_{\rm out} = 8\times10^8\,{\rm cm}$  based on the Roche lobe [49]. The resulting differential photon density is depicted in Fig. 3.10 and Fig. 3.11 for the corresponding acceleration regions, where a mass accretion rate based on Eq. (2.10) is considered. The accretion disk spectrum looks like a regular blackbody spectrum due to the narrow accretion disk. For an acceleration region close to the accretion disk, these photons contribute significantly at lower energies.

These assumptions only hold for efficient accretion rates close to the Eddington accretion rate as described in the accretion disk model from Sunyeav and

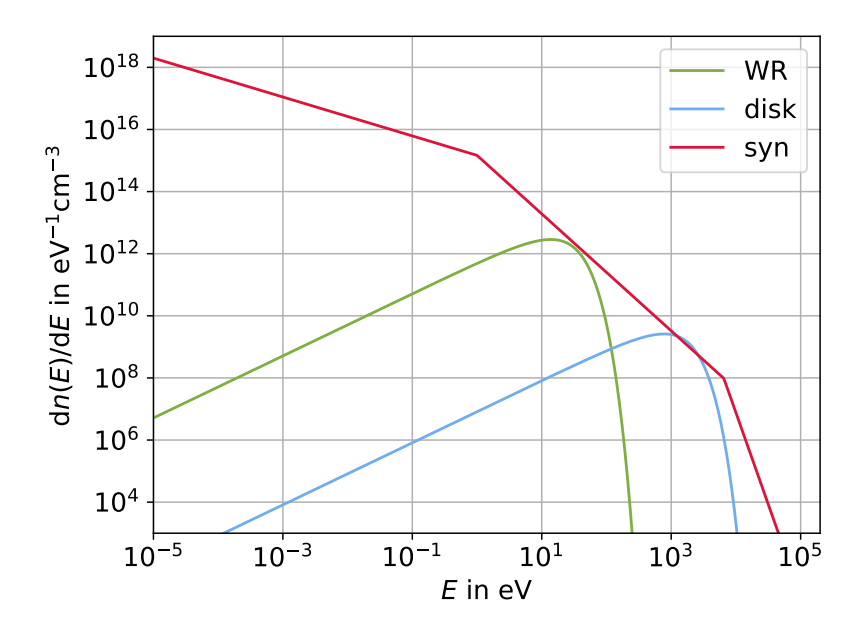


**Figure 3.11:** Photon densities ambient in the vicinity of Cygnus X-3 in  $S_2$ . Accretion disk photons (disk), stellar photons (WR) and synchrotron photons (syn) are considered with synchrotron photons exhibiting a cut-off at 1 GeV for high energies and at  $10^{-6}$  eV for low energies.

Shakura [25]. Furthermore, these geometric assumptions approximate the photon density close to the accretion disk and thus in  $S_1$ . However, in  $S_2$  it holds that  $r_j \ll r_{\rm disk}$ , which verifies a simple point-source approximation for the accretion disk. As a result, in  $S_2$  and at locations  $r_j$  far enough away from the black hole, the accretion disk photon density can be approximated by Eq. (3.7), where the reference radius becomes  $r_{\rm in}$  as the inner accretion disk dominates in radiation emission.

In Fig. 3.10, it becomes apparent that the shape of the photon density for the accretion disk does not vary much compared to the stellar photon spectrum. Due to the small size of the accretion disk, the overlapping blackbody spectra do not significantly broaden the curve. Therefore, it is a valid approach to approximate the accretion disk spectrum by a blackbody spectrum for a given temperature of an accretion disk ring element  $r_0$  reducing the differential photon density of the accretion disk to

$$\frac{\mathrm{d}n_{ph}(E,r)}{\mathrm{d}E} = \frac{4\pi}{(hc)^3} \frac{E^2}{\exp(E/[k_{\rm B}T(r_0)]) - 1} \left[ \frac{r}{\sqrt{r^2 + r_{\rm in}^2}} - \frac{r}{\sqrt{r^2 + r_{\rm out}^2}} \right].$$
(3.12)

The photon spectrum resulting from synchrotron emission is first outlined theoretically here by following the explanation in M. Longair [2]. First, it is assumed that the distribution of charged particles, which in this case are protons and electrons, can be described as  $N(E) dE \sim E^{-p} dE$  with a power-law distribution for particles within the energy interval E + dE. Furthermore, it can be approximated that particles with energy E emit photons close to the critical frequency  $v_c$  and thus

$$v_{\rm c} \approx \left(\frac{E}{mc^2}\right)^2 \left(\frac{eB}{2\pi m}\right) \tag{3.13}$$

can be written for the emitted frequency with the gyro frequency  $v_g$ . The radiated spectrum in the frequency interval v + dv, which results from an accelerated particle in the energy range E + dE, can be described as

$$J(\nu)d\nu = \left(-\frac{dE}{dt}\right)N(E)dE. \tag{3.14}$$

The given particle distribution as well as the relation between the particle energy and photon frequency allow to write

$$E = \sqrt{\left(\frac{v_{\rm g}}{v}\right)}mc^2,\tag{3.15}$$

$$dE = \frac{mc^2}{2\sqrt{v_g \nu}} d\nu, \tag{3.16}$$

whereby Eq. (4.16) in Section 4.3 is used here without derivation. It follows that the spectrum of synchrotron photons is proportional to  $J(v) \sim v^{-(p-1)/2}$ . This leads to the conclusion that the shape of the photon spectrum can be deduced from the slope of the particle distribution, which in this context is p=2.3 for particles accelerated by both shock acceleration and reconnection.

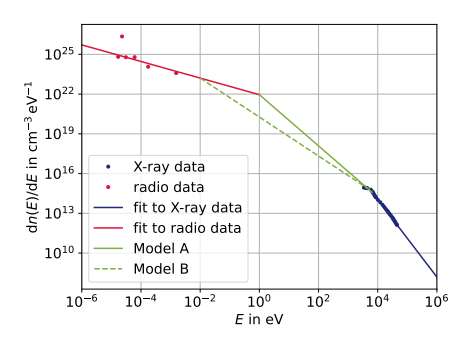
However, the source becomes optically thick for low-energy photons due to synchrotron self-absorption. The low-energy synchrotron photons scatter with the initial electrons, which gain energy and emit synchrotron photons again by being deflected by the magnetic field. The resulting plasma that can be described as a quasi-thermal equilibrium, and thus an effective temperature  $T_{\rm eff} = \gamma mc^2/(3k_{\rm B})$ 

can be assigned to the particles by noting that the temperature depends on the particle energy. Due to the low energy regime and the fact that the particles cannot emit radiation more efficiently than a black body, the Rayleigh-Jeans limit holds giving

$$S_{\nu} = \frac{2k_{\rm B}T_{\rm eff}}{\lambda^2}\Omega,\tag{3.17}$$

with  $\Omega$  representing the solid angle covered by the source and  $\lambda$  being the photon wavelength associated with the photon frequency. Consequently, it can be deduced that the low-energy end of the photon spectrum yields  $J(\nu) \sim \nu^{5/2}$ .

As the maximum energy of the electrons is limited, the synchrotron radiation exhibits a cut-off for high energies. Hence, as suggested in the previous analyzes, the synchrotron spectrum can be explained by a broken power-law function accompanied by a cut-off. In this context, two separate photon data sets from Cygnus X-3 are of particular relevance, one corresponding to high energies and the other to low energies.



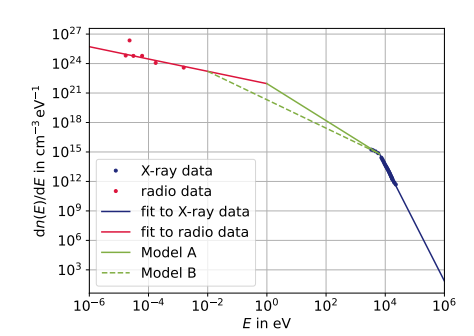


**Figure 3.12:** Synchrotron flux estimated for  $S_1$  (*left*) and  $S_2$  (*right*) on the basis of X-ray data from Ref. [50] and radio data from Ref. [45]. A power-law fit has been applied to both data sets, which have been connected by another power-law.

The radio photon data are taken from Ref. [45], and the X-ray data are taken from Ref. [50], respectively. It should be noted that, for high-energy photons, it is possible to distinguish between the different regions of Cygnus X-3 (see Section 3.3). Consequently, two different spectra can be obtained for  $S_1$  and  $S_2$ , although both regions are part of the HS. However,  $S_2$  is assumed to appear only close to HyS and therefore the photon spectrum measured for HyS is considered more realistic in  $S_2$ . The considered X-ray photon fluxes are presented in Fig. 3.12 consistent with the considerations in Section 3.3.

It is important to note that the photon energy band between the radio and

X-ray bands is not included in the data. Theoretically, a power law spectrum corresponding to  $E^{-(p-1)/2}$  can be found for this. It is assumed that three power law functions,  $f_i$  with  $i \in \{0, 1, 2\}$ , describe the synchrotron spectrum. However, due to the presence of other unknown parameters, the value of p is not strictly defined, and multiple configurations for the medium power-law are possible. A change in slope can be observed in the X-ray data, indicating an transition from  $f_1$  to  $f_2$  at  $\sim 5 \times 10^3$  eV. The transition from  $f_0$  to  $f_1$  would determine the slope of  $f_1$ . Fig. 3.12 illustrates the congruence between the data and the power-law fits, incorporating two distinct slopes of  $f_1$  (denoted as Model A and Model B). In the subsequent analysis, Model A is selected, as the transition from  $f_0$  to  $f_1$  is determined in Ref. [45] and corresponds to approximately 1 eV.

The photon density can be calculated as

$$\frac{\mathrm{d}n(E,r_{\rm j})}{\mathrm{d}E} = \frac{F(E)}{Ec}k(r_{\rm j}),\tag{3.18}$$

where the flux is assumed on the basis of the data and included model for synchrotron photons (see Fig. 3.12) and  $k(r_i)$  is a factor taking into account the location of the observer. The synchrotron photons are produced in the respective acceleration region including the production of synchrotron photons in  $S_1$ at  $r_{\rm cr} = 10 R_{\rm S}$  and in  $S_2$  at  $r_{\rm cr} = 7 \times 10^{11}$  cm. For a simple approach, the synchrotron emitting region is a lobe of diameter  $r_{\rm syn}$  equal to the length scale of the accelerating region with center  $r_{\rm cr}$ . Inside the lobe, the photon density is constant at  $n(E, r_{syn})$ . Note that  $r_{syn}$  varies with distance from the black hole. In  $S_1$ , the length scale of the acceleration region is given by B. Khiali [45] as  $l_{\rm acc} = 5 \times 10^7 \, {\rm cm} \approx 8.3 \, R_{\rm S}$ . The innermost circular orbit, the photon sphere, has an extension of  $r_p = 1.5 R_S$  [51] for non-rotating black holes. Comparing this with the extension of the accelerating region it can be concluded that  $S_1$  extends almost into the photon sphere. Consequently, in reality  $S_1$  may be more farther from the black hole but not closer. However, the important parameters, especially in comparison to the parameters in  $S_2$ , would not shift significantly for slightly larger assumptions for  $r_{cr,S1}$ , and to be consistent with the mentioned literature, the center of the acceleration region is not shifted outwards here.

The length of the acceleration region for  $S_2$  can be calculated using trigonometry, taking into account the jet opening angle  $\theta_o = 12^\circ$ . The radius of the acceleration region is equal to the shock radius, which is determined by the jet cross section at  $r_{\rm cr}$ . Subsequently, the length scale of the shock acceleration region is equal to

$$r_{\text{cr,S2}} \cdot \tan(\theta_o) = 1.5 \times 10^{11} \text{ cm.}$$
 (3.19)

Based on these assumptions, the distance factor includes jet photons for both particle interactions and particle spectra. As a result, the distance factor equals

$$k(r) = \begin{cases} \left(\frac{(d - r_{\rm cr})^2}{|(r_{\rm cr} - r_{\rm syn})|^2}\right), \text{ for } r_{\rm j} \ll r_{\rm syn}, \\ \left(\frac{(d - r_{\rm cr})^2}{|(r_{\rm cr} - r_{\rm j})|^2}\right), \text{ for } r_{\rm j} \gg r_{\rm syn}. \end{cases}$$
(3.20)

In Fig. 3.10 and Fig. 3.11 the assumed synchrotron photon density is shown for the regions  $S_1$  and  $S_2$ . The maximum synchrotron photon energy has a cutoff at  $E_{\rm max}=10^6$  eV, while a minimum synchrotron energy is reached at  $E_{\rm min}=10^{-6}$  eV. The photons from the accretion disk are found to be considerably denser than the synchrotron photons for energies between  $[2\times10^2$  eV,  $5\times10^3$  eV]. The stellar photons are less abundant in  $S_1$  relative to the other two photon fields, which is reasonable, as the Wolf-Rayet star is significantly more distant.

It can be concluded that, for most energies, synchrotron photons dominate the ambient photon density due to the narrow acceleration region. However, in S2, the acceleration region becomes larger by a factor greater than 10³, leading to a lower synchrotron photon density. Furthermore, an increase in distance to the black hole results in the reduction of the accretion disk to a point source, leading to a further decrease in the abundance of accretion disk photons. This results in dominant stellar photon density compared to the accretion disk photons, whereas the stellar photons peak at lower energies due to lower temperature. Synchrotron radiation remains dominant for all energies. However, within the energy interval [10¹ eV, 10⁴ eV], both accretion disk photons and stellar photons are present in significant quantities, thereby contributing to a photon density that originates from all three sources within the specified energy range.

Both the photohadronic interaction and the opacity vary strongly depending on which photon field is considered. In the following work, interactions with the ambient photon field are carried out. Therefore, it is useful to distinguish between the different photon sources, as they scale differently with respect to distance. Therefore, WR refers to the stellar blackbody photons, disk refers to the accretion disk photon field, and syn refers to the photons in the blob originating from synchrotron emissions and the summed photon density contributes as

$$\frac{\mathrm{d}n}{\mathrm{d}E} = \frac{\mathrm{d}n_{\mathrm{syn}}}{\mathrm{d}E} + \frac{\mathrm{d}n_{\mathrm{disk}}}{\mathrm{d}E} + \frac{\mathrm{d}n_{\mathrm{WR}}}{\mathrm{d}E}.$$
 (3.21)

Initially, highly relativistic protons are injected into the acceleration region, and this chapter focuses on the critical interactions that occur following this injection. First, important energy loss and acceleration rates are evaluated, providing a basic context for understanding the dynamics. Previous chapters have established that the main secondary particles of interest are neutrinos and photons. Unlike neutrinos, photons interact with ambient photon fields and are subject to attenuation. Consequently, the concept of optical depth is studied in detail for photons, enhancing the understanding of their propagation and interaction mechanisms beyond the acceleration region.

# 4.1 Energy Change

To understand the physical processes in microquasars, it is necessary to study the interactions of the initial protons, but also of secondary particles such as ultra-high-energy photons. Particle interactions include both energy loss and energy gain processes. The protons and the corresponding secondary particles are subject to acceleration and deceleration mechanisms while they are in the acceleration region. In general, the interaction rate  $t_{\rm int}^{-1}$  is described by the power P = -dE/dt as follows

$$t_{\text{int}}^{-1} = \frac{1}{E} \left| \frac{dE}{dt} \right|$$
 [2]. (4.1)

A heuristic approach is to examine the particle interactions that occur only in terms of the respective energy loss rate. It is assumed that the energy loss rates ultimately determine the maximum energies of the particles. Therefore, the most efficient acceleration and emission rate competes with the most efficient deceleration or absorption rate. This enables the estimation of maximum particle energies and the development of a simulation concept based on  $t_{\rm int}^{-1}$ .

### 4.2 Particle Acceleration

As discussed earlier, the protons are accelerated by two different mechanisms depending on the considered acceleration region. Khiali et al. proposed a specific scenario for particle acceleration by magnetic reconnection, which is used for the

#### **Chapter 4** Particle Interactions

following simulations. Based on the 3D numerical simulation results of Ref. [52], the proton acceleration rate can be described as

$$t_{\text{rec},p}^{-1} = 1.3 \times 10^5 \left(\frac{E}{E_0}\right)^{-0.4} t_0^{-1},$$
 (4.2)

where  $t_0$  describes the Alfvén time. This time is defined as  $t_0 = l_{\rm acc}/v_{\rm A}$ , where the relativistic Alfvén velocity is given by  $v_{\rm A0} = B/\sqrt{4\pi\rho}$  as

$$v_{\rm A} = v_{\rm A0} \left( 1 + \frac{v_{\rm A0}^2}{c^2} \right)^{-0.5}. \tag{4.3}$$

The acceleration rate in the Eq. (4.2) holds for protons, although it can be usefully modified to  $t_{{\rm rec},i}^{-1}=\sqrt{m_p/m_i}t_{{\rm rec},p}^{-1}$  for other particles noted with index i [45].

To describe the shock acceleration, in the Bohm limit for a quasi-parallel shock, it can be assumed that the mean free path of a particle is its Larmor radius  $r_L$ . The Bohm diffusion coefficient  $D_{\rm B}$  can be used to approximate the shock acceleration rate as

$$t_{\rm sh} = \zeta \frac{D_{\rm B}}{v_{\rm c}^2},\tag{4.4}$$

with shock velocity  $v_s$  [30] and efficiency  $\zeta$  estimated as  $\zeta \approx 0.1$  [53]. In consideration of the definition of the Bohm diffusion coefficient as  $D_B = 1/3r_Lc$ , the shock acceleration rate is expressed as

$$t_{\rm sh}^{-1} = \eta \frac{ecB}{E},\tag{4.5}$$

where the shock velocity is accounted for by  $\eta \sim v_{\rm s}^2/c^2$ . It is assumed that the shock velocity is not relativistic, and thus the parameter  $0 < \eta \ll 1$  is applicable. For the purposes of this study, the parameter will be set to  $10^{-3}$ .

# 4.3 Synchrotron Radiation

All charged particles interact with the surrounding magnetic fields and are thus accelerated. This particle acceleration causes the emission of photons, which are defined as synchrotron radiation if they are emitted by relativistic particles. However, a non-relativistic approach can be used to derive the synchrotron radiation rate by considering the photon emission in the rest frame of the accelerated particle. A comprehensive calculation has been carried out by M. Longair [2], and the following explanations and calculations are based on his work. The non-relativistic acceleration  $\vec{v}$  of a charged particle in a homogeneous magnetic field

by neglecting external forces is determined by the Lorentz force. This can be described in the rest frame of the charged particle S' by

$$\frac{\mathrm{d}\vec{p}'}{\mathrm{d}t'} = e(\vec{E}' + \vec{v}' \times \vec{B}') = m\dot{\vec{v}}'. \tag{4.6}$$

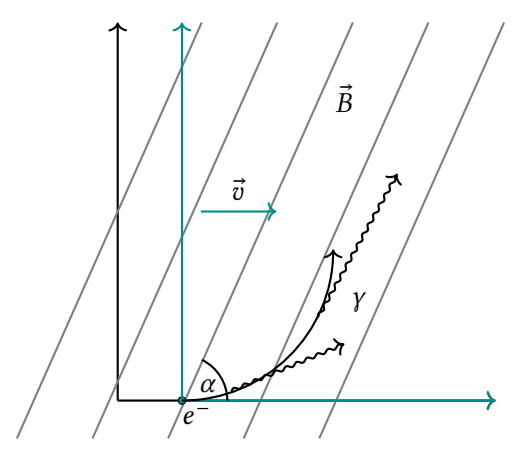


**Figure 4.1:** Sketch of a charged particle  $(e^-)$  moving in a static magnetic field that expands in the x and z directions. Acceleration causes the emission of photons  $(\gamma)$ . The configuration can be described in the magnetic field frame (black) and also in the rest frame of the electron (blue coordinates).

The magnetic field is described by  $\vec{B}'$  and the particle velocity by  $\vec{v}'$  in the particles rest frame. Let the magnetic field be constant in S with no y direction (the configuration is illustrated in Fig. 4.1). Since a constant magnetic field does not induce an electric field, it is assumed here that there is no other significant independent electric field. However, in S' the magnetic field is moving and an electric field is induced as a result. On the other hand, the velocity of the charged particle in its rest frame becomes  $\vec{v}' = 0$ , and as a result the Lorentz force in S' reduces to  $\vec{F}' = e\vec{E}'$ .

The Lorentz transformation can be found by describing the electromagnetic field in terms of the tensor  $F^{\mu\nu}$ . A detailed derivation can be found in Ref. [54] and here without calculation, the electromagnetic field tensor equals

$$F^{\mu\nu} = \begin{pmatrix} 0 & -E_x/c & -E_y/c & -E_z/c \\ E_x/c & 0 & B_z & -B_y \\ E_y/c & -B_z & 0 & B_x \\ E_z/c & B_y & -B_x & 0 \end{pmatrix}. \tag{4.7}$$

#### **Chapter 4** Particle Interactions

The Lorentz transformation matrix is given by Eq. (2.25) and requires a calculation for a velocity in the *x*-direction. The field vector then transforms via  $F^{\mu\nu'} = \Lambda^{\mu}_{\alpha}\Lambda^{\nu}_{\beta}F^{\alpha\beta}$  [54] and the respective components of the electric field result in

$$E_x' = E_x, (4.8)$$

$$E_y' = \gamma (E_y - vB_z), \tag{4.9}$$

$$E_z' = \gamma (E_z + vB_u). \tag{4.10}$$

The geometry of the system results in an acceleration given by Eq. (4.6) as  $\dot{\vec{v}} = e/m\vec{E}'$  and with the E-field component from Eq. (4.8) it follows

$$\dot{\vec{v}} = -\frac{v\sin(\alpha)Be\gamma}{m}.\tag{4.11}$$

A particle accelerated by  $\dot{\vec{v}}$  emits power given by Larmors formula [27]

$$P = \frac{e^2 \dot{\vec{v}}^2}{6\pi\epsilon_0 c^3}. (4.12)$$

For this scenario the calculation yields

$$P = \frac{e^4 v^2 \sin^2(\alpha) \gamma^2 B^2}{6\pi \epsilon_0 c^3 m^2}.$$
 (4.13)

This equation can be rearranged by using  $c = 1/(\mu_0 \epsilon_0)$  and the definition of the Thompson cross section  $\sigma_T$  which leads to

$$P = \sigma_{\rm T} \frac{m_e^2}{m^2} \frac{B^2}{\mu_0} \beta^2 \gamma^2 \sin^2(\alpha) c. \tag{4.14}$$

This calculation is accurate for specific separation angles between particle velocity and magnetic field. However, as explained in Section 2.5, the charged particles constantly scatter on magnetic irregularities. Therefore, Eq. (4.14) has to be modified by considering an isotropic distribution of the separation angles. This can be done by including the average

$$P = 2\sigma_{\rm T} \frac{B^2}{8\pi} \beta^2 \gamma^2 c \int_0^{\pi} \frac{\sin^3(\alpha)}{2} d\alpha = \frac{4}{3} \frac{m_e^2}{m^2} \frac{\sigma_{\rm T} B^2}{8\pi} \beta^2 \gamma^2 c. \tag{4.15}$$

To calculate consistently in cgs units, it holds  $\mu_0 = 4\pi$  and the magnetic energy density  $B^2/(2\mu_0)$  becomes  $B^2/(8\pi)$ . Finally, Eq. (4.1) can be used to write the synchrotron rate as

$$t_{syn}^{-1} = \frac{4}{3} \frac{\sigma_{\rm T} B^2}{8\pi} \left(\frac{m_e}{m}\right)^2 c \frac{E}{m^2 c^4} = \frac{4}{3} \frac{\sigma_{\rm T} B^2}{8\pi} \left(\frac{m_e}{m^2}\right)^2 \frac{E}{c^3}.$$
 (4.16)

### 4.4 Photohadronic Interactions

All charged elementary particles interact in first order with photons. Thus not only protons but also secondary particles among them pions, muons and kaons interact with photons. In the following, the photohadronic interaction is described explicitly and differences to explicit photomesonic interactions are discussed below.

Once a fraction of the initial protons are accelerated to sufficient high energies, they may interact with the ambient photons and produce neutral and charged pions via

$$p + \gamma \to \Delta^+ \to \begin{cases} n + \pi^+ \\ p + \pi^0 \end{cases}$$
 (4.17)

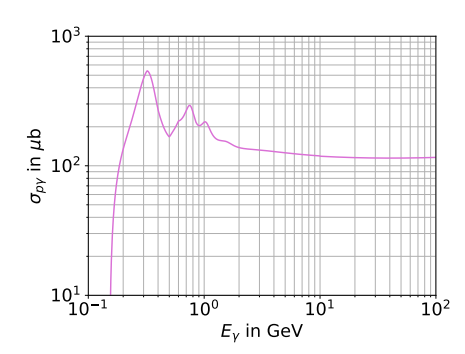
In Eq. (4.17) the excited proton state  $\Delta^+$  decays into the proton and positively charged pion with a branching ratio of 1/3. Neutral pions immediately decay into two photons due to their lifetime of  $t_{\pi^0}^{-1}=(8.43\pm0.13)\times10^{-17}~\mathrm{s}$  [55]. Charged pion decay chains contain various leptons depending on the initial charge and energy. Pions mainly decay as follows

$$\pi^{\pm} \to \mu^{\pm} + \nu_{\mu} \to e^{\pm} + 2\nu_{e} + \nu_{\mu},$$
 $\pi^{0} \to \gamma + \gamma,$ 
(4.18)

whereby no differentiation is made between antineutrinos and neutrinos. A more detailed description for the branching ratios and the following secondary particles is given in [55]. For higher energies, multiple meson and lepton production becomes relevant and must be considered in the calculations. All processes occur under charge, lepton flavor, and lepton number conservation.

The cross section for photohadronic interactions  $\sigma_{p\gamma}$  is strongly energy dependent, which is illustrated in Fig. 4.2. In the low energy regime, the cross section is dominated by resonance peaks, since resonance production is the dominant process in this regime. For higher energies, the cross section is determined mainly by multi-particle production [56]. The photohadronic energy loss rate can be described as

#### **Chapter 4** Particle Interactions



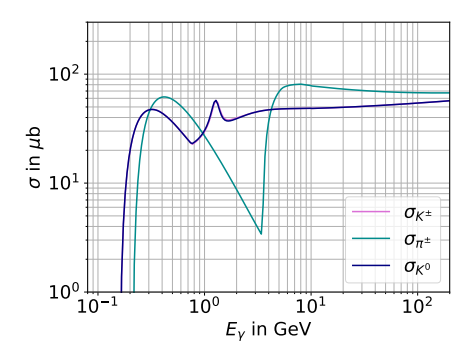


**Figure 4.2:** Cross section of the results obtained from photohadronic interactions, expressed in terms of the photon energy in GeV in the rest frame of the respective hadron. *Left* presents the cross section taken from the SOPHIA program [56] and *right* illustrates cross sections for mesons, calculated by an adjusted SOPHIA program by Ref. [57].

$$t_{p\gamma}^{-1}(\gamma_p) = \frac{c}{2\gamma_{p_p}^2} \int_{E_{\text{th}}/(2\gamma_p)}^{\infty} dE_{\text{ph}} \frac{n_{\text{ph}}(E_{\text{ph}})}{E_{\text{ph}}^2} \int_{E_{\text{th}}}^{2\gamma_p E_{\text{ph}}} d\epsilon_{\text{r}} \sigma_{p\gamma}(\epsilon_{\text{r}}) K_{p\gamma}(\epsilon_{\text{r}}) \epsilon_{\text{r}}$$
(4.19)

in the rest frame of the proton with  $K_{p\gamma}$  representing the elasticity of the scattering process. Then describes  $\epsilon_{\rm r} = \epsilon \gamma_p (1 - \beta_p \cos(\phi))$  the photon energy in the proton rest frame. This follows directly from Eq. (2.31), since the photon is a massless particle. An isotropic photon distribution  $n_{\rm ph}(E_{\rm ph})$  is assumed [58].

The threshold energy for the process  $E_{\rm th}$  can be determined by minimizing Eq. (2.34) in the proton rest frame. Therefore, the three momenta of both protons and the pion are set to zero and it follows by considering the rest energies  $E_{i,0}$ 

$$s = m_p^2 + 2E_{p,0}E_Y \ge m_p^2 + m_\pi^2 + 2E_{p,0}E_{\pi,0}. \tag{4.20}$$

Thus, the minimum photon energy for the interaction is

$$E_{\rm th} = E_{\gamma} = m_{\pi} \left( 1 + \frac{m_{\pi}}{2m_p} \right) \approx 145 \text{ MeV}.$$
 (4.21)

For photomesonic interactions, in particular photon-pion and photon-kaon scattering, the photon density considerations apply, and the geometric considerations regarding the threshold energy for the process equally apply to mesons. For the photohadronic interactions the SOPHIA code [56] is used. SOPHIA is a powerful Monte Carlo simulation for the calculation of photon-proton interactions in astrophysical environments. In this context, the SOPHIA code will

be used in an extended version that can also be used to study interactions of photons with pions and kaons.

For photomeson interactions, Eq. (4.19) holds, but with different cross sections  $\sigma_{\pi\gamma}$  and  $\sigma_{K\gamma}$ . However, the cross sections for photomesonic interactions are not directly given by the SOPHIA algorithm. A detailed analysis for  $\gamma\pi$  and  $\gamma K$  interactions is given by Ref. [57]. The cross sections calculated with the extended SOPHIA code are given in Fig. 4.2. They are approximate, therefore the resonances are not calculated in detail. The interactions with charged and neutral kaons appear to be of equal first order.

## 4.5 Hadronic Interactions

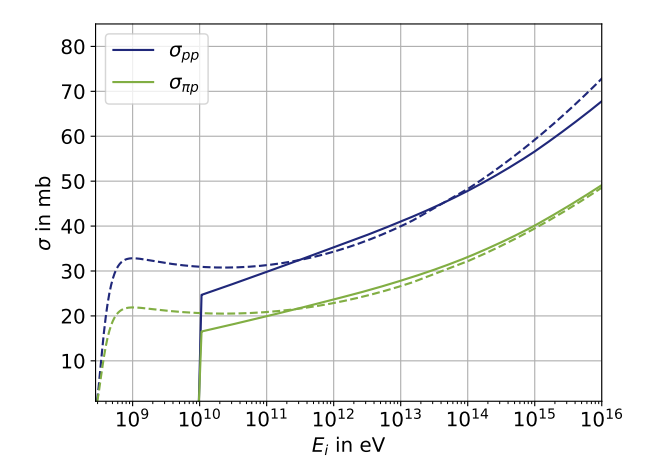


**Figure 4.3:** Calculated cross sections for hadronic interactions of pions and protons. The solid line is the respective  $\sigma$  calculated with QGS-JET and the dashed line indicates the approximated cross section from Eq. (4.23).

As mentioned in Section 3.4, the main focus is on hadronic scenarios to explain the measured spectra of Cygnus X-3. Therefore, the inelastic proton-proton interaction is relevant. Several interactions can occur in this collision. Excited proton resonances such as  $\Delta^{++}$  and  $\Delta^{+}$  could be produced, as well as other secondary particles. These inelastic processes and subsequent decays occur under the conservation of all fundamental variables such as energy, momentum, charge, baryon number and lepton number.

The most important secondary particles in these processes are neutral pions,

#### **Chapter 4** Particle Interactions

which decay into high-energy photons. Furthermore, charged pions and kaons are created, which can also produce neutrinos and high-energy photons in their decays. The proton-proton energy loss rate is given by Ref. [45] as

$$t_{pp}^{-1}(E_p) = n_p \sigma_{pp} ck, (4.22)$$

where k denotes the elasticity of the interaction, which is approximately  $k \approx 0.5$  and the proton density is described in Section 3.6. In this case, the cross section  $\sigma_{pp}$  has been calculated by Ref. [59] and is dependent on the energy of the incoming proton  $E_p$  through

$$\sigma_{pp}(E_p) = \left[34.3 + 1.88 \ln\left(\frac{E_p}{1\text{TeV}}\right) + 0.25 \ln\left(\frac{E_p}{1\text{TeV}}\right)^2\right] \left(1 - \left(\frac{E_{\text{th}}}{E_p}\right)^4\right)^2 \text{mb.}$$
 (4.23)

This approximation is used to estimate the energy loss rate. In the full simulation, however, the QGS-JET Software [60] with the internal hadronic interaction model is used, which includes detailed cross section calculations. Fig. 4.3 shows the cross sections for both pion and proton interactions with the surrounding protons in the Wolf-Rayet stellar wind. The solid line represents the cross-section predictions as computed by QGS-JET, while the dashed line provides a comparative representation of the approximation derived from Eq. (4.23). A local maximum in the interaction cross section is observed for both pions and protons at energies in the low GeV range. This feature is not taken into account in the QGS-JET model, but does not significantly affect the primary results, since particles in the GeV energy range are not energetic enough to contribute significantly to the production of gamma rays and associated high-energy neutrino. At higher energies, both the QGS-JET calculations and the approximation yield qualitatively congruent results, underlining the consistency of the two approaches in the relevant energy regimes.

The threshold energy for single  $\pi^0$  production can be calculated via [59]

$$E_{th} = (m_p + 2m_\pi)c^2 + \frac{m_\pi^2}{2m_p} \approx 1.22 \times 10^{-3} \text{TeV}.$$
 (4.24)

The secondary pions can also interact with the surrounding protons. In general, inelastic scattering interactions can not be calculated using pertubative quantum chromodynamics. However, Ref. [1] introduced a rough assumption about the pion-proton cross section based on the valence quark content in the particles. This leads to  $\sigma_{\pi p} \approx 2/3\sigma_{pp}$ , which is close to the empirical results. This assumption is taken here to be precise enough for approximations.

# 4.6 Inverse Compton Scattering

Muons, like protons, undergo interactions with both matter and radiation. Muons in matter interact via four main processes, namely ionisation (electronic stopping power), bremsstrahlung, pair production in the electric field of a nucleus and inelastic nuclear interactions. The last three can be summarised as radiative processes. The stopping power for muons in matter can be described by

$$\left\langle \frac{\mathrm{d}E}{\mathrm{d}x} \right\rangle = a(E) + b(E)E,$$
 (4.25)

where the term b(E) denotes the radiative processes and a(E) describes the ionisation contribution [61].

Both parameters for the respective muon interactions depend on the initial muon energy. However, for a rough overview, the parameters can be approximated by constants  $a = 2 \times 10^{-3} \,\text{GeVcm}^3/\text{g}$  and  $b = 3.9 \times 10^{-6} \,\text{cm}^3/\text{g}$  [29]. For these values, Fig. 4.4 shows muon stopping power due to interactions in matter as a function of muon energy. It can be seen that ionisation processes play a dominant role for muons with energies below 1 TeV. Radiative processes become relevant for higher muon energies and may be more important in this context.

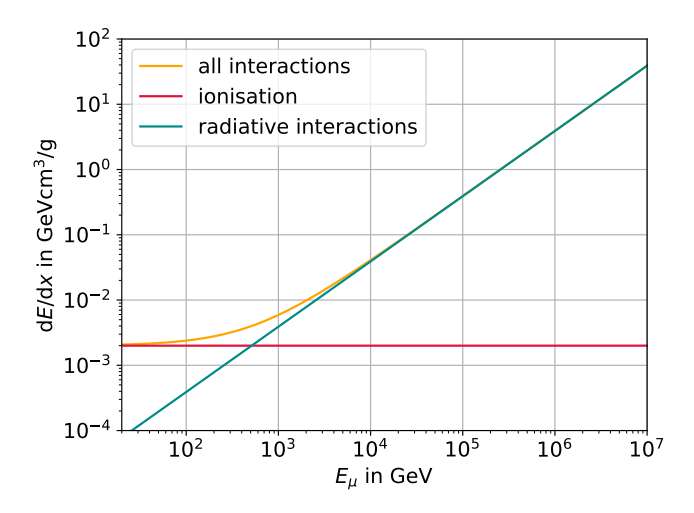


**Figure 4.4:** Muon stopping power in matter as a function of muon energy  $E_{\mu}$ , calculated using Eq. (4.25) and approximate values taken from Ref. [29].

Muons are the lightest particles of matter considered in this thesis that interact with other photons ( $e^{\pm}$  are not important in this scenario). Therefore, unlike heavier particles such as pions, they can interact with photons via the inverse Compton effect.

#### **Chapter 4** Particle Interactions

Inverse Compton scattering describes the energy transfer process in which ultrarelativistic particles scatter off low-energy photons. The relativistic particle looses energy, and the photon gains energy. This process is therefore called inverse Compton scattering, because it is the opposite energy transfer to Compton scattering, but from a physical point of view the two scattering processes are equivalent. The following explanations for the scattering process were first described by G.R. Blumenthal and J.R. Gould [62]. They introduced high-energy electron interaction processes with radiation. However, the same considerations apply to muon-photon interactions in the case of inverse Compton scattering, so the following section is based on their work.

In general, the inverse Compton effect is effective for low-mass particles such as electrons and muons. In the following, values in the laboratory system (S) are not marked and variables in the electron rest frame (S') are written as dashed variables. The following considerations are based on photon-electron scattering, although they can also be applied to photon-muon scattering. The final photon energy  $\epsilon_f$  after the scattering process can be described as

$$\epsilon_f' = \frac{m\epsilon'}{m + \epsilon'(1 - \cos(\vartheta'))} \tag{4.26}$$

by the scattering angle  $\theta$  and the initial photon energy  $\epsilon_0$  in the rest frame of the massive particle. While in the lab system the outgoing photon energy is described by

$$\epsilon_f = \gamma \epsilon_f (1 + \beta \cos(\pi - \theta')) \approx \gamma \epsilon_f (1 - \cos(\theta')).$$
 (4.27)

In the Thompson limit it holds  $\epsilon \ll mc^2$ . As a result, the photon carries a small amount of energy from the scattering particle, since Eq. (4.26) reduces to  $\epsilon_f' \approx \epsilon_0$ . In the laboratory system, the maximum energy of the photon is given by assuming a head-on collision for Eq. (4.27). This results in  $\epsilon_{f,\max} \approx 2\gamma\epsilon_f' \approx 4\gamma\epsilon$ . The characteristic energy gain of the photon is proportional to  $\gamma^2$ . However, the energy loss of a non-relativistic particle is small compared to a relativistic particle. On the other hand, in the Klein-Nishima regime, the cross section becomes energy dependent and the scattered photon carries a large fraction of the incident particle.

For the energy loss rate of the electron energy conservation applies and thus it is the inverse of the energy gain rate of the scattered photon. In the general case, where the initial electron has relativistic energies, the Klein-Nishina limit has to be considered. For the total energy loss rate per particle is then

$$-\frac{\mathrm{d}E}{\mathrm{d}t} = \int \mathrm{d}E_{\gamma} (E_{\gamma} - E_{\mathrm{ph}}) \frac{\mathrm{d}N}{\mathrm{d}t \mathrm{d}E_{\gamma}},\tag{4.28}$$

with  $E_{\gamma}$  denoting the resulting photon energy and  $E_{\rm ph}$  describes the initial energy of the scattered photon. The scattered photon spectrum per particle can be derived by geometrical considerations and yields as

$$\frac{\mathrm{d}N}{\mathrm{d}t\mathrm{d}E_{\gamma}} = \frac{2\pi r_0^2 mc^3}{\gamma} \frac{n(E_{\mathrm{ph}})dE_{\mathrm{ph}}}{E_{\mathrm{ph}}} F_{\mathrm{IC}}(q) \tag{4.29}$$

where  $\gamma = E/(mc^2)$  yields and the following definitions hold as follows with *l* denoting the respective lepton properties

$$F(q) = 2q \ln(q) + (1 + 2q)(1 - q) + 0.5(1 - q) \frac{(\Gamma q)^2}{1 + q\Gamma},$$

$$\Gamma = \frac{4E_{\text{ph}}E_l}{(m_l c^2)^2},$$

$$q = \frac{E_{\gamma}}{\Gamma(E_l - E_{\gamma})}.$$
(4.30)

As a result, the inverse Compton rate can be written by integrating over both the ambient photon field and the scattered photons as

$$t_{\rm IC}^{-1} = \frac{2\pi r_0^2 m^2 c^5}{E^2} \int_{E_{\rm min}}^{E_{\rm max}} \frac{n(E_{\rm ph})}{E_{\rm ph}} dE_{\rm ph} \int_{E_{\rm ph}}^{\Gamma E/(\Gamma+1)} F_{\rm IC}(q) (E_{\gamma} - E_{\rm ph}) dE_{\gamma}.$$
(4.31)

Here,  $\gamma$  represents the final photon energy, while initial photon variables are marked with the subscript (ph). This holds for all particles, scattering on an isotropic distributed photon field. Since  $t_{\rm IC}^{-1}$  scales with the square of the particle mass, inverse Compton energy losses are only relevant for low-mass particles interacting electromagnetically.

### 4.7 Pair Production

Radiation propagating through media can interact via various processes depending on the energy of the photons. The radiation transfer equation

$$\frac{\mathrm{d}I_{\mu}}{\mathrm{d}s} = -\alpha_{\mu}I_{\mu} + j_{\mu} \tag{4.32}$$

describes emission and absorption processes for photons with specific intensities  $I_{\mu}$  related to their frequency along a line element ds. The coefficients  $\alpha_{\mu}$  and  $j_{\mu}$  value the emission and absorption regarding to the process. For the specific case in which only absorption is considered ( $j_{\mu}=0$ ), the linear differential equation can be solved as

$$I_{\mu}(s) = I_{\mu}(s_0) \exp\left(-\int_{s_0}^{s} \alpha_{\mu}(s') ds'\right).$$
 (4.33)

This form can be rewritten as  $I_{\mu}(s) = I_{\mu}(s_0) \exp(-\tau)$  with  $\tau$  defined as optical depth along the direction of photon propagation [63].

Since the energy of the protons considered is sufficiently high, it is convenient to assume that only photon pair production is the dominant energy loss process. The optical depth for pair production depends strongly on the energy of the interacting photons. In the case of Cygnus X-3, the high-energy photons from the jet annihilate the low-energy photons from the Wolf-Rayet star. The stellar photon distribution is determined by the thermal radiation profile of the star and is given by Eq. (3.7).

The most significant interaction of high-energy photons is pair production mechanism in form of  $\gamma + \gamma \rightarrow e^+ + e^-$ . The optical depth for this process can be written as

$$\tau_{\gamma}(E_{\gamma}, r) = \int_{r}^{\infty} \int_{\epsilon_{\min}}^{\infty} n(\epsilon_{0}, r') \sigma_{\gamma\gamma}(\epsilon_{0}, E_{\gamma}) d\epsilon_{0} dr', \tag{4.34}$$

with  $E_{\gamma}$  representing the energy of the  $\gamma$ -ray and  $\epsilon_{\min}$  being the threshold energy for pair production in an isotropic photon field [6].

The process is well understood from the quantum mechanical perspective. Now, let the four-momentum vectors of the incoming photons be  $p_{\gamma}$  and  $p'_{\gamma}$  and further the four-momentum vector of the outgoing electron is  $p_{e^-}$  and for the positron respectively  $p_{e^+}$ .

With the conservation of momentum, the squared center of mass energy can be calculated as follows

$$s = (p_{\gamma} + p_{\gamma}')^2 = (p_{e^+} + p_{e^-})^2. \tag{4.35}$$

Considering the photon rest frame and the scattering angle between the photons  $\theta$  the equation becomes

$$\epsilon E_{\gamma}(1 - \cos(\theta)) = 2E_{e}^{2},\tag{4.36}$$

whereby  $\epsilon$  describes the low energy photon and  $E_{\gamma}$  the high-energy photon. The energies need to add up to the total electron and positron energies  $E_e^2$  and thus the threshold energy for the scattering on a thermal photon is determined by

$$\epsilon_{\min} \ge \frac{2m_e^2 c^4}{E_V(1 - \cos(\theta))}.\tag{4.37}$$

For pair production, the total cross section  $\sigma_{\gamma\gamma}$  in dependency on relative velocity  $\beta$  equals [64]

$$\sigma_{\gamma\gamma}(\beta) = \frac{\pi r_0^2}{2} (1 - \beta^2) \left[ (3 - \beta^4) \ln \left( \frac{1 + \beta^2}{1 - \beta^2} \right) - 2\beta (2 - \beta^2) \right]$$
 (4.38)

for a relative velocity of electron or positron in the center of momentum frame  $\beta = \sqrt{1-s^{-1}}$ . The dimensionless center of mass energy of the system is given by s in the form of

$$s = \frac{E_{\gamma}\epsilon(1 - \cos(\theta))}{2m_e^2c^4}.$$
 (4.39)

The particle interactions and properties of Cygnus X-3 have been taken into account in the previous chapter. In the subsequent analysis, the energy loss rates in the simulation are used to estimate the maximum particle energies in order to evaluate the simulation results and control the foundation of the simulation. Furthermore, the energy loss rates are used to calculate the proton attenuation depth in addition to the optical depth. This interaction depth is relevant for integrating interactions outside the acceleration region into the simulation and for predicting the expected particle spectra on Earth. A comprehensive overview is given, highlighting the contributions of the energy loss rates to the simulation and the numerical setup. Finally, a summary of all expected interactions is given, together with the critical simulation parameters.

# 5.1 Particle Behavior in the Acceleration Region

Based on the assumptions about acceleration and energy loss rates, it is possible to estimate the maximum energy for a given particle. The maximum energy is reached once the rate of the strongest acceleration becomes smaller than an energy loss rate of the specific particle. First, some considerations regarding the system geometry and general parameters are presented. After deriving these values and finalizing the simulation assumptions, the maximum energies for the protons are considered determining the initial energies for the secondary particles. The energy loss rate and resulting energies of the most abundant secondary particles ( $\mu^{\pm}$ ,  $\pi^{\pm}$ ,  $K^{\pm}$ ) are also estimated. They have lifetimes which may allow them to interact with the surrounding medium before decaying. All interaction mechanisms are studied in both jet acceleration regions  $S_1$  and  $S_2$ . Due to the circular orbit, the maximum particle energies should be not significantly modulated in  $S_1$ . However, in  $S_2$  it is important to distinguish between different orbital phases.

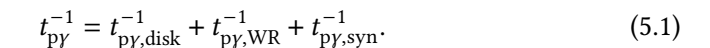
It is valid to approximate the maximum particle energies  $E_{i,\max}$  for the different particle types based on the respective energy loss rates. The interactions as well as the simulations are stochastic processes and therefore the following calculations regarding the maximum particle energy are order of magnitude estimates and are important for understanding the simulation results. As the simulation is based on energy loss rate calculations, it is important to know

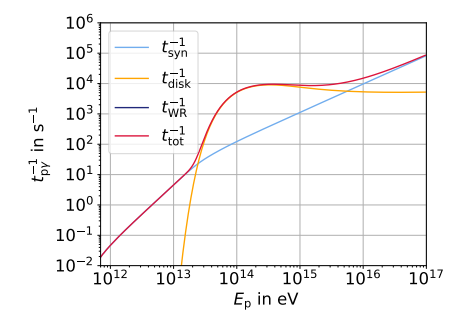
what to expect from the Monte Carlo interaction in order to minimize errors and achieve consistent results.

It is important to note that Fermi acceleration models are confronted with what is referred to as the *injection problem*. The Fermi acceleration mechanism only becomes effective for particles that exhibit energies significantly higher than those observed in thermal equilibrium. While the Fermi mechanism is adequate for describing high-energy particle spectra, it is incapable of intrinsically resolving the initial acceleration of particles in thermal equilibrium. To address this challenge, various models have been developed to explain the injection problem, with particle-in-cell (PIC) simulations being employed for specific investigations [65, 66]. As both the shock acceleration and reconnection acceleration are based on the Fermi mechanism, the injection problem manifests in both  $S_1$  and  $S_2$ . However, the subsequent simulation does not address the initial acceleration of thermal particles suggesting that the injection problem may be adequately addressed.

#### 5.1.1 Protons

First, the photohadronic energy loss rate is considered individually, beginning with protons in  $S_1$ . The different photon sources contribute to the total photohadronic energy loss rate by





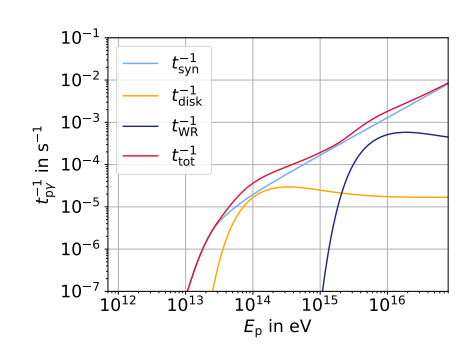


**Figure 5.1:** Photohadronic energy loss rate  $(t_{\text{tot}}^{-1})$ , considered individually for synchrotron photons  $(t_{\text{syn}}^{-1})$ , stellar photons  $(t_{\text{WR}}^{-1})$  and accretion disk photons in  $(t_{\text{disk}}^{-1})$  for  $S_1$  on the *left* and  $S_2$  on the *right*.

In Fig. 5.1, the photohadronic energy loss rate is presented separately for the different photon sources in  $S_1$ . The synchrotron photons have high enough energies to dominate the interactions with protons in the energy range up to  $E_p = 10^{13}$  eV.

The energy cut-off of the synchrotron photons determines the onset of photohadronic interactions. As demonstrated in the graph, the synchrotron cut-off at  $E_{\rm ph}=10^6$  eV causes an onset of synchrotron radiation for the lowest energies, which are relevant for this analysis. With increasing proton energies, the protons can contribute more to the threshold energy and are able to interact with lower-energy photons. Therefore, the accretion disk photons become important interaction targets. For proton energies higher than  $E_{\rm p}=2\times10^{13}$  eV, they dominate the photohadronic energy loss rate. In the case of energies that exceed  $E_{\rm p}=5\times10^{15}$  eV, the synchrotron photons once again dominate the interaction. This result corresponds to the analysis of the different photon fields in Section 3.6. Stellar photons possess even lower energies than accretion disk photons. However, they are not abundant enough to contribute significantly to the photohadronic energy loss rate.

The photohadronic energy loss rates with both the accretion disk photons and the stellar photons scale as a function of distance determined by Eq. (3.6). However, the factors are different, and in addition the synchrotron photon density in  $S_2$  has a different shape. It is therefore useful to study the photohadronic energy loss rate for the separate photon densities in  $S_2$  as well as illustrated on the right-hand side of Fig. 5.1.

Since the size of the synchrotron emission lobe  $l_{\rm acc}$  is larger by a factor more than  $10^3$  in  $S_2$ , the peak density of synchrotron photons is significantly reduced. The accretion disk photons are also less dense in  $S_2$  due to the distance from the accretion disk. Consequently, the photohadronic energy loss rate in  $S_2$  is primarily dominated by the synchrotron photons leading to a different shape than for  $S_1$ . However, the scale of the energy loss rate is substantially diminished by a factor of  $10^7$  resulting in interactions with stellar photons at proton energies exceeding  $E_{\rm p}=10^{16}$  eV. Note, that the accretion disk is characterized by a higher temperature than the Wolf-Rayet star. The stellar photons are unable to contribute to interactions involving lower energy jet protons. In summary, the energy loss rate is dominated in  $S_2$  by interactions with synchrotron photons and some contributions from the other two photon fields.

The proton energy loss rates are illustrated in Fig. 5.2 for the proton acceleration in  $S_1$ . The magnetic reconnection acceleration is highly efficient and therefore the maximum proton energy reaches approximately  $E_{\rm max}=6\times10^{16}$  eV. Protons in this energy regime belong to the region above the knee in the cosmic ray spectrum. Protons at these energies are capable of producing ultra-high-energy  $\gamma$  rays. The maximum energy is determined by photohadronic interactions, as they represent the dominant energy loss process in this context. As previously analyzed, the main photon field contributing to the interaction is the synchrotron photon field. Synchrotron emissions are the primary cause of proton energy

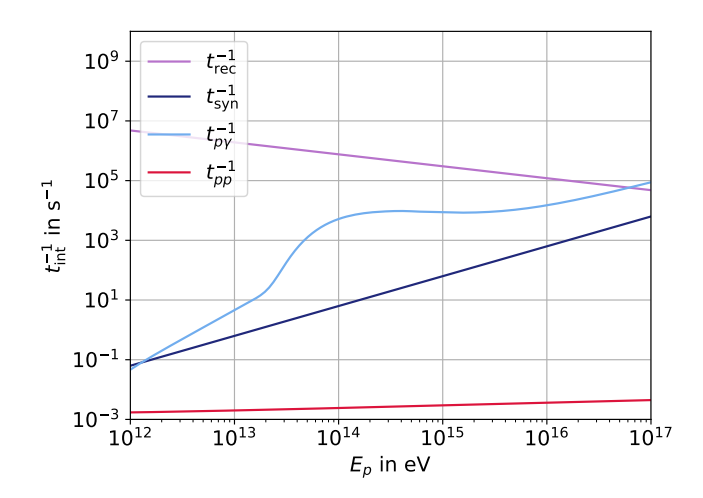


**Figure 5.2:** Particle energy loss rates for protons in the Cygnus X-3 jet for  $S_1$  dominated by magnetic reconnection acceleration  $(t_{\rm rec}^{-1})$ . The protons loose energy through hadronic  $(t_{pp}^{-1})$ , photohadronic  $(t_{p\gamma}^{-1})$  and synchrotron interactions  $(t_{\rm syn}^{-1})$ .

loss in  $S_1$  only for energies lower than  $E_p = 10^{12}$  eV, which is not relevant in this instance. Proton-proton interactions are smaller than the other energy loss mechanisms and therefore their influence on the resulting proton spectrum is negligible.

Within the framework of this particular configuration, protons are accelerated to energies sufficient to engage in interactions with the ambient photons. This may result in significant particle production due to photohadronic interactions for energies greater than  $E_{\rm p}=10^{16}$  eV.

This finding can be regarded as a basis for comparison with the results obtained by Khiali et al. [45]. Their research focused on proton acceleration in the vicinity of a black hole, at a distance  $10\,R_{\rm S}$ , analogous to  $r_{\rm cr}$  in  $S_1$ . The magnetic field in their study is equivalent to the one considered here, given the same distance, thereby ensuring equivalent synchrotron losses. Both  $t_{\rm rec}^{-1}$  and  $t_{\rm pp}^{-1}$  are determined by the ambient protons (see Eq. (4.2)), and, given their assumption of significantly higher densities, these rates are higher than in this work. Shock acceleration was considered as an additional factor in their work. However, it is at least an order of magnitude less efficient and therefore does not determine the maximum proton energy, so it is not initially considered in this work for  $S_1$ . Finally, the photohadronic interaction in this work includes different photon fields with especially including measurement data for synchrotron estimates, and thus differs the most from all the considered rates. In contrast to the assumptions performed

in Section 3.6, the accretion disk photons and the stellar photons were considered negligible in Khiali et al. [45]. They found the photohadronic interaction dominating the energy loss mechanisms. However, due to the mentioned differences in the photon field estimates, their calculated maximum energy is one order of magnitude lower than found in this scope.

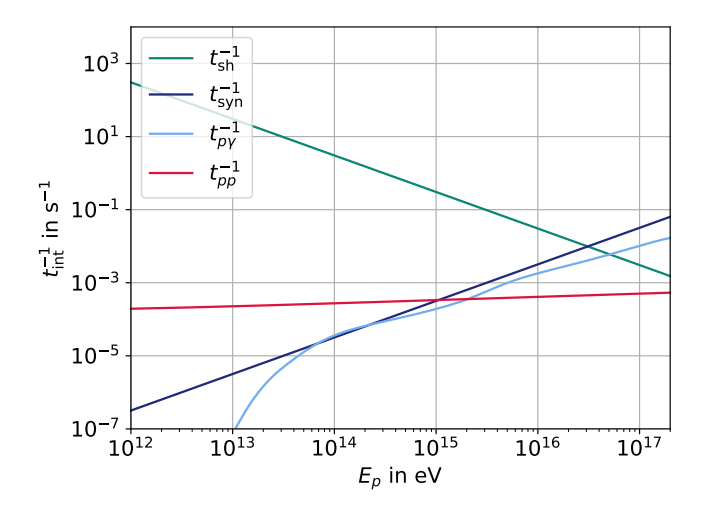


**Figure 5.3:** Particle energy loss rates for protons in the Cygnus X-3 jet for  $S_2$  with shock acceleration  $(t_{\rm sh}^{-1})$ . The protons loose energy through hadronic  $(t_{pp}^{-1})$ , photohadronic  $(t_{p\gamma}^{-1})$  and synchrotron interactions  $(t_{\rm syn}^{-1})$ .

The interactions in  $S_2$  are calculated based on the equations in Chapter 4 and illustrated in Fig. 5.3. The magnetic field strength B is significantly lower in this region due to the greater distance of the acceleration region in the jet from the black hole. The particle densities for Wolf-Rayet particles, as protons and blackbody photons, are phase dependent. The phase has been set to  $\theta = 0$  in this graph. This refers to the outermost position of particle acceleration, relative to the Wolf-Rayet star.

As mentioned in Section 3.4, the significant particle acceleration mechanism at this distance is shock acceleration. In general, magnetic reconnection is more efficient than diffusive shock acceleration. Furthermore, shock acceleration becomes less effective due to the weaker magnetic field strength. Due to the lower magnetic fields, the synchrotron losses are less efficient. The synchrotron photons are now originating from a larger region and thus are less dense at  $r_{\rm cr}$  in  $S_2$  than in  $S_1$ . Accretion disk photons and stellar photons can contribute to photohadronic interactions at specific energies. However, due to the distance to the

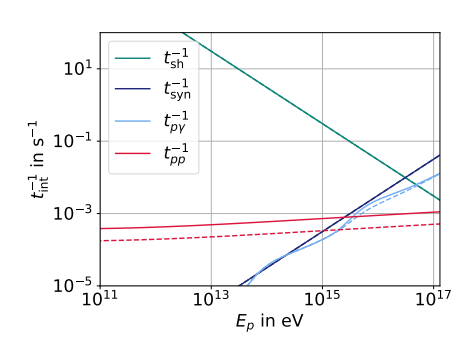
respective photon source, the density of accretion disk and stellar photons is reduced, thus leading to a dominance of the synchrotron photon field in the photohadronic interaction. The lower magnetic field results in a lower synchrotron rate, yet it remains the dominant energy loss mechanism for energies exceeding  $E_{\rm p}=10^{12}\,{\rm eV}$ . The proton-proton energy loss rate is independent of  $r_{\rm j}$ , instead being influenced by  $r_{\rm WR}$ , which exhibits a substantially smaller relative change and consequently undergoes a less significant reduction compared to the other two energy loss mechanisms. The shock acceleration rate is lower than in Khiali et al. [45], as it is less efficient ( $\eta=10^{-3}$ ) and the magnetic field is some orders of magnitude weaker in  $S_2$  in comparison to  $S_1$ . Moreover, the results from Khiali et al. [45] should only be compared to  $S_1$  as the parameters in  $S_2$  do not correspond to those.

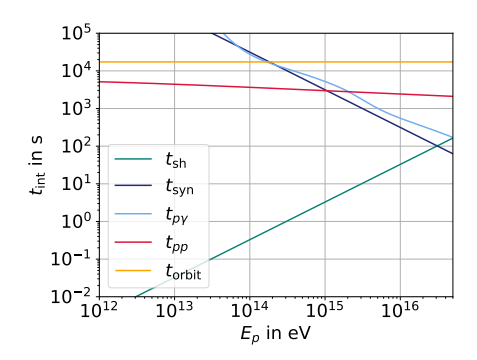
In consideration of the previously mentioned factors, the maximum proton energy in  $S_2$  is determined by the synchrotron loss mechanism, resulting in energies of  $E_{\rm max}=3\times10^{16}$  eV. However, as photohadronic interactions play a subdominant role, there is an insufficient number of target photons to cause high-energy  $\gamma$  production in the acceleration region. A further discussion point is whether the high-energy protons interact sufficiently with the ambient medium after leaving the source and causing high-energy  $\gamma$  and corresponding neutrinos outside the acceleration region.

Finally, it is essential to consider the geometrical restriction (Hillas criterion, see Section 2.5) for both acceleration regions. This criterion is contingent on the magnetic field strength and the extent of the acceleration region, necessitating its separate consideration for both regions. It is noteworthy that the maximum energy constrained by the Hillas criterion is  $E_{\rm Hillas} = 2.26 \times 10^{17}$  eV in S1 and  $E_{\rm Hillas} = 1.51 \times 10^{18}$  eV in S2. In both scenarios, the Hillas criterion represents the upper limit, which exceeds the calculated maximum energy. This outcome serves to demonstrate the efficiency of the accelerator, attributable to the presence of strong magnetic fields. Furthermore, it is reasonable to expect that protons will be limited by their respective interactions in these two distinct regions, rather than leaving the source due to geometrical constraints.

The total energy loss rates and the resulting maximum proton energy are phase independent in  $S_1$  due to the circular orbit. However, they become phase dependent in  $S_2$  because the jet has an extension greater than the orbital distance. It is therefore important to study the interaction timescales  $t_{\rm int}$ . Fig. 5.4 shows on the right side the timescales for the four main interaction mechanisms in  $S_2$  at the orbital angle  $\vartheta = 0$ . All considered energy loss interactions occur on timescales of the order of the orbital period. However, the shock acceleration  $t_{\rm sh}$  occurs on timescales of less than a second. Moreover, the restriction of proton energy due to synchrotron losses and some photohadronic losses manifests for protons

with energies exceeding  $E=10^{15}$  eV. In this case, the two interactions are in the order of 10 s, corresponding to a negligible fraction of the orbital period and can be attributed to a particular orbital phase. This leads to the conclusion that particle acceleration occurs at specific orbital configurations of Cygnus X-3. As a consequence, the particle interactions must be considered depending on orbital phase  $\theta$ , since the orbital phase modulates the position of the acceleration region and may influence the maximum particle energy.



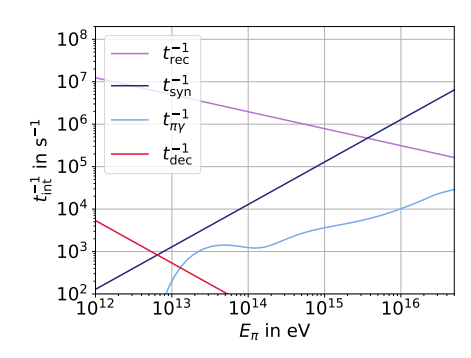


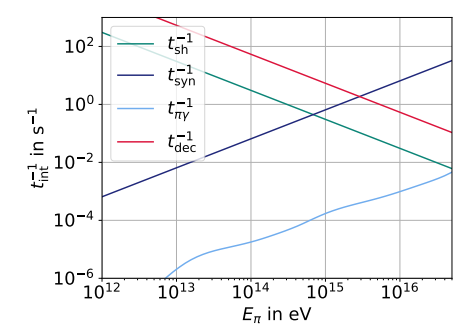
**Figure 5.4:** Particle energy loss rates (*left*) and timescales (*right*) for protons in the Cygnus X-3 jet in  $S_2$ . Diffusive shock acceleration (sh) is favored. The protons loose energy through hadronic (pp), photohadronic (p $\gamma$ ) and synchrotron interactions (syn). Note that the dashed lines indicate phase  $\vartheta = \pi$ . The timescales are compared to the orbital timescale (orbit).

Fig. 5.3 shows the maximum energy in  $S_2$  for  $\vartheta=0$ . The same interactions are examined at  $\vartheta=\pi$  for the same orbital separation. The energy loss rates for the orbital phase  $\vartheta=\pi$  (dashed lines) compared to  $\vartheta=0$  (solid lines) in Fig. 5.4 on the left side. Reconnection, proton-proton interaction and photohadronic interactions with stellar photons depend on the local proton density. However, the reconnection is only considered for  $S_1$ . Due to the elaborations regarding photohadronic interactions,  $t_{p\gamma}$  here does depend on the orbital phase only for high energetic protons as they may interact with the stellar photons. Furthermore,  $t_{pp}$  is the only interaction that is shifted in the graph for all proton energies. It is shifted by a factor less than two, which is almost negligible as it is already a less important interaction mechanism.

These findings confirm the calculation of the following interactions with a fixed angle  $\theta=0$  and demonstrate that phase modulation of the particle interactions in the acceleration region is negligible. It is important to note that this is clearly distinguished from the orbital modulated signal at Earth, which may appear due to propagation after the acceleration region.

# **5.1.2 Pions**





**Figure 5.5:** Pion interactions in  $S_1$  (*left*) and in  $S_2$  (right). In  $S_1$ , reconnection  $(t_{\rm rec}^{-1})$  is favored, where in  $S_2$  shock acceleration  $(t_{\rm sh}^{-1})$  is considered for pion acceleration. They loose energy through photomesonic  $(t_{\pi\gamma}^{-1})$  and synchrotron  $(t_{\rm syn}^{-1})$  interactions. The decay rate is denoted as  $t_{\rm dec}^{-1}$ .

In proton interactions, pions are produced as secondary particles. In the following, only charged pion interactions are considered, as neutral pions do not carry an electromagnetic charge and therefore do not interact with the magnetic field. Furthermore, their lifetimes are too short, so they immediately decay into two gamma-rays. Charged pions may have lifetimes long enough to interact with the surrounding medium before decaying.

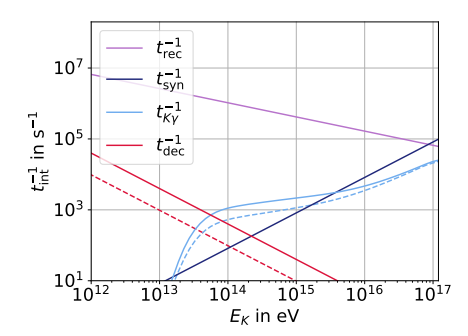
The pion interactions are presented in Fig. 5.5 on the left side for  $S_1$ . In this region, synchrotron emission is the main energy loss process for pions since their rest mass is lower than the rest mass of protons. It is important to note that, when taking into account the synchrotron interactions, the lower pion mass is the only difference to the considerations for protons. In the context of photohadronic interactions, the distinct cross section,  $\sigma_{\pi\gamma}$ , is incorporated in conjunction with the lower pion mass. As a result, synchrotron energy loss for pions dominates the energy regime where photohadronic interactions are dominant for protons. Reconnection is sufficiently efficient in the considered energy regime that the pions are significantly accelerated and interact before decaying, since  $t_{\rm dec}^{-1}$  is always lower than  $t_{\rm rec}^{-1}$ . The energy-dependent decay rate is a well understood relativistic effect. Finally, synchrotron emission limits the pion energy to  $E_{\pi,\rm max} \approx 3 \times 10^{15}\,{\rm eV}$ . This is less than the maximum proton energy. However, pions originating from protons with less than  $E_{\pi,\rm max}$  can be further accelerated in the acceleration region before they may decay.

In  $S_2$ , synchrotron emission plays a rather minor role due to the weaker mag-

netic field strength. Nevertheless, photomeson interaction is not the dominant energy loss process for pions in the energy regime of interest due to the same reasons as mentioned for protons in  $S_2$ . However, here the pion decay rate is an order of magnitude higher than the acceleration rate. Thus, pions resulting from interaction processes neither gain nor loose energy in the acceleration regime. They decay immediately without interaction.

It can be concluded that, in both regions, photomesonic interactions play a subdominant role in the acceleration region. This implies that pions, as secondary particles in the simulation, do not create further secondary particles by photomesonic interactions. In  $S_1$ , pions may be accelerated if they have lower energies, and in  $S_2$  they decay immediately. Consequently, it is expected that only decay products will result from pions in the acceleration region.

# 5.1.3 Kaons



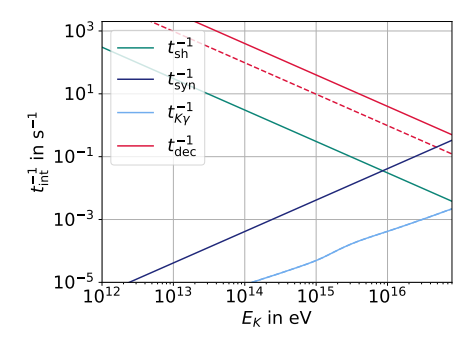


**Figure 5.6:** Kaon interactions in  $S_1$  (*left*) and in  $S_2$  (right). In  $S_1$ , reconnection  $(t_{\rm rec}^{-1})$  is favored, where in  $S_2$  shock acceleration  $(t_{\rm sh}^{-1})$  is considered. They loose energy through photomesonic  $(t_{K\gamma}^{-1})$  and synchrotron  $(t_{\rm syn}^{-1})$  interactions. The decay rate is denoted as  $t_{\rm dec}^{-1}$ . The dashed lines in both plots represent the neutral Kaon  $(K_L^0)$  interactions.

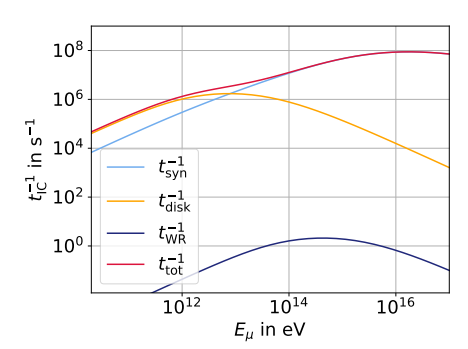
Distinctions can be made between the four different kaon types by examining their mass, charge and lifetime. The first two variables differ only for charged and neutral kaons. However, it is necessary to distinguish between  $K_S^0$  and  $K_L^0$  only in terms of kaon lifetime. In contrast, the same assumptions about charge apply to kaons as apply to pions. Neutral kaons decay without interaction due to the absence of electromagnetic charge, even if the  $K_L^0$  has a lifetime comparable to the charged kaons which may interact. The kaon energy loss rates for  $S_1$  are shown in Fig. 5.6 on the left side. Charged kaons are heavier than pions but lighter than protons, resulting in synchrotron emission being a more effi-

cient process of energy loss than for pions, but less efficient than for protons. However, in the small energy regime between  $E_{\rm disk} = [2 \times 10^{13} \, {\rm eV}, 2 \times 10^{15} \, {\rm eV}]$ , photomesonic energy losses become more relevant than synchrotron losses. In comparison to pions in  $S_1$ , the kaon decay rate is lower than the acceleration rate, resulting in kaons with a given initial energy being accelerated in the acceleration region to energies of almost  $E_{K,\rm max} \approx 9 \times 10^{16} \, {\rm eV}$ . However, these are ultimately limited by synchrotron radiation, and thus only direct kaon decay products may result from kaons of the maximum energy. For kaons with energies in  $E_{\rm disk}$ , photomesonic processes are the most dominant energy loss mechanism, and thus various secondary particles are created in photomesonic interactions if the acceleration of kaons is neglected.

As illustrated in Fig. 5.6, neutral kaons ( $K_L^0$ ) exhibit distinct interactions that require separate analysis due to their independence from the magnetic field, resulting in neither acceleration nor synchrotron radiation emission. Consequently, the sole interaction mechanism considered for neutral kaons is photomeson interaction. As demonstrated in the graph, neutral kaons exhibit distinct decay rates and photomesonic energy loss rates due to their higher mass and longer lifetime compared to charged kaons. Kaons decay exclusively for energies below  $E_K = 4 \times 10^{13} \, \mathrm{eV}$  without interaction, implying that for higher energies, neutral kaons primarily produce secondary particles through interactions with photons in  $S_1$ .

The kaon energy loss rates in  $S_2$  are depicted in Fig. 5.6 on the right-hand side. In this scenario, the energy loss rates are derived using the same rationale as for pions and protons. Due to the reduced magnetic field strength, both synchrotron emission and shock acceleration are less efficient. Photomeson interactions are diminished due to the lower photon densities, and now synchrotron photons are the primary photons contributing as targets for all energies considered here. Synchrotron interactions limit the kaon energies to approximately  $E_K = 9 \times 10^{15}$  eV. However, kaons decay in  $S_2$  for all energies prior to interaction in the acceleration region. Consequently, in the simulation, kaons decay immediately in  $S_2$  before any energy change occurs.

In the analysis of  $S_1$ , it was established that neutral kaons must be considered for photomesonic interactions, and this principle also applies to  $S_2$ . However, the photon density in  $S_2$  is so low that neutral kaon decay is dominant for all energies, resulting in immediate kaon decay without energy loss, as is the case for charged kaons.



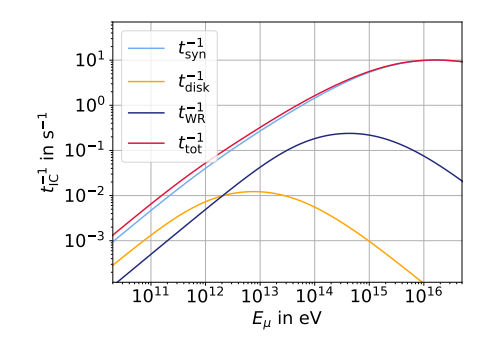


**Figure 5.7:** Inverse Compton energy loss rate  $t_{\text{IC}}^{-1}$  for muons considered separately for the ambient photon fields in  $S_1$  (*left*) and  $S_2$  (*right*). The muons can interact with stellar photons ( $t_{\text{WR}}^{-1}$ ), accretion disk photons ( $t_{\text{disk}}^{-1}$ ) and synchrotron photons ( $t_{\text{syn}}^{-1}$ ).

# 5.1.4 **Muons**

Muons, as elementary particles, interact with photons via inverse Compton radiation. Unlike the particles considered previously, the inverse Compton interaction does not produce any secondary particles. A detailed discussion of the inverse Compton effect is given in Section 4.6. Due to the absence of a threshold energy for the interaction and the two interaction regimes, namely the Thompson and Klein-Nishima regimes, the three considered photon fields may contribute differently to the photohadronic interactions. The total Compton energy loss rate is determined as

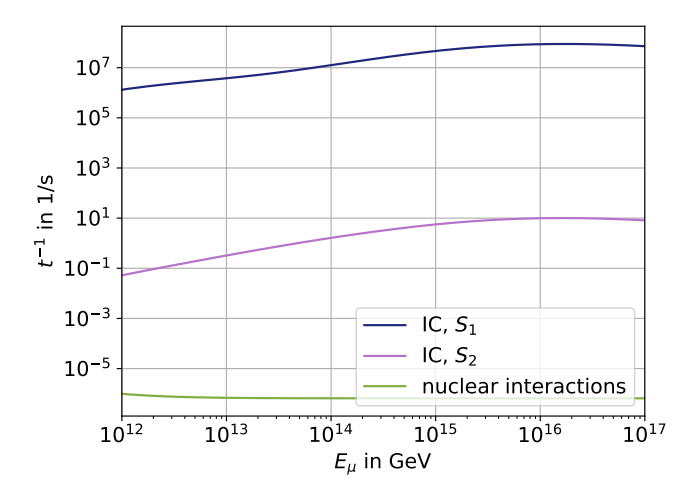
$$t_{\rm IC}^{-1} = t_{\rm IC, \, disk}^{-1} + t_{\rm IC, wr}^{-1} + t_{\rm IC, syn}^{-1}$$
 (5.2)

using Eq. (4.31) for the separate photon field interactions, analogue to the photomesonic interactions.

As illustrated in Figure 5.7, the left side of the figure shows the contribution of the different photon fields to the total inverse Compton interaction in  $S_1$  and the right side shows the contribution in  $S_2$ . In  $S_1$ , the muons are close to the accretion disk, resulting in the accretion disk photons being the dominant scattering target for muon energies up to  $E_{\mu} = 10^{13}$  eV. The contribution of stellar photons to the inverse Compton process is negligible due to the distance of the Wolf-Rayet star. However, for energies above  $E_{\mu} = 10^{13}$  eV, synchrotron photons become the dominant interaction target due to the increasing photon density for lower energy synchrotron photons. Consequently, for muons with higher energies, the threshold energy is already satisfied with lower energetic photons, thereby enabling synchrotron photons with lower energies to become

the target. At these energies, the accretion disk photons exhibit significantly lower densities. As the subsequent investigations focus on high-energy particles with energies above  $10^{13}$  eV, it can be deduced that in  $S_1$  solely the synchrotron photons contribute to the inverse Compton interaction of the muons.

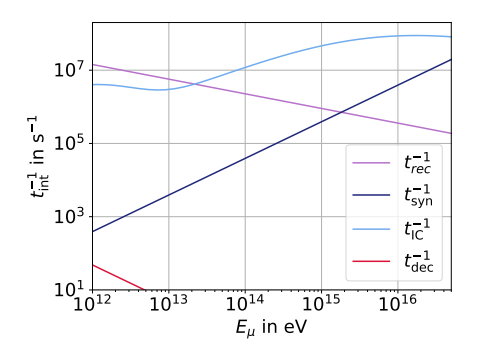
In the case of  $S_2$ , the scenario is distinct, given that the distance from the acceleration region to the accretion disk and to the Wolf-Rayet star is of the same order of magnitude as the extent of the acceleration region itself. This results in inverse Compton rates that are significantly lowered for both synchrotron photons and accretion disk photons. However, given the logarithmic scale employed in Fig. 5.7, it is evident that synchrotron photons emerge as the predominant target for muon inverse Compton interactions within the pertinent energy range. In comparison to the  $S_1$  scenario, the total inverse Compton rate is reduced by seven orders of magnitude.



**Figure 5.8:** Muon interactions represented with both photons (IC) for different muon energies in  $S_1$  and  $S_2$ . Nuclear interactions of muons are plotted for  $S_1$ , representing a mean energy loss rate.

It is evident from Chapter 4 that the interactions of muons may be not only photon-based, but also involve nuclear interactions. The investigation presented in Fig. 5.8 illustrates the outcomes of all the observed muon interactions. It is important to note that nuclear interactions are influenced by distance. The nuclear energy loss rate depends on nuclear density, which is determined by the distance to the Wolf-Rayet star  $r_{\rm WR}$ , it is maximum in  $S_1$  and does not change significantly. It can be seen directly that inverse Compton interaction is dominant in both regions. As the most effective energy loss mechanism is determining the energy

behavior of the particle, it is valid to exclude nuclear interactions of muons in the simulation.



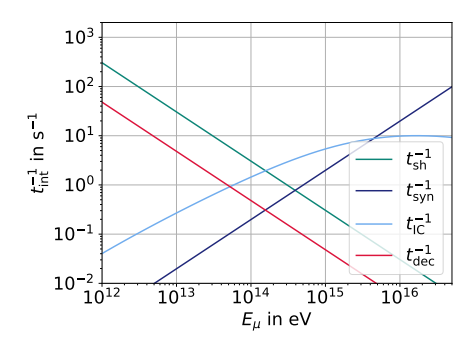


**Figure 5.9:** Muon interactions in  $S_1$  (*left*) and in  $S_2$  (right). In  $S_1$ , reconnection  $(t_{\rm rec}^{-1})$  is favored, where in  $S_2$  shock acceleration  $(t_{\rm sh}^{-1})$  is considered. They loose energy through inverse Compton interaction  $(t_{\rm IC}^{-1})$  and synchrotron  $(t_{\rm SVI}^{-1})$  interactions. The decay rate is denoted as  $t_{\rm dec}^{-1}$ .

In order to calculate the maximum muon energy in  $S_1$ , it is necessary to take all relevant muon energy loss rates into account. Fig. 5.9 illustrates on the left the important muon interactions that account for  $S_1$ . Muons decay at a rate that is smaller than all other energy loss rates for the considered energy regime. For most muon energies, inverse Compton scattering is the dominant interaction mechanism. However, reconnection is sufficiently efficient to enable muons to gain energy, with synchrotron interactions playing a subdominant role. Ultimately, muons are accelerated to a maximum energy of approximately  $E_{\text{max},\mu} \approx 2 \times 10^{13} \text{ eV}$ , where inverse Compton interactions limit the muon energy. Given that particles with energies higher than 10<sup>13</sup> eV are the focus of consideration, it is anticipated that high-energy muons resulting from other secondary decay or interactions will undergo a substantial loss in energy, with the result that they will depart from the acceleration region or decay with energies in the order of some  $E_{\mu} = 10^{13}$  eV. It is crucial to note that the inverse Compton mechanism does not result in the creation of secondary particles. Consequently, determining the energy at which the respective muons decay is essential for calculating the final energy of the resulting neutrinos.

Furthermore, Fig. 5.9 shows all significant muon energy loss rates for muons in  $S_2$ . As in  $S_1$ , muon decay is a non-dominant process over the entire energy range of interest and scales anti-proportional to the shock acceleration rate. The inverse Compton interaction with the surrounding synchrotron photons is the primary mechanism for muon energy dissipation for all muons with energies between  $E_{\mu} = 2 \times 10^{14}$  eV and  $E_{\mu} = 5 \times 10^{15}$  eV. For high muon energies, the

synchrotron interaction becomes dominant. However, it does not contribute in first order to maximum muon energies, as they are limited by inverse Compton interactions to approximately  $E_{\mu} = 2 \times 10^{14}$  eV. With regard to  $S_1$ , it is anticipated that muons with higher energies will either depart from the acceleration region or undergo decay within it. In either scenario, a substantial energy loss will have occurred, resulting in muons with energies of approximately  $10^{14}$  eV being present in  $S_2$ .

# 5.1.5 Comparative Analysis

This section provides a brief overview of the anticipated outcomes of the simulation which is also summarized in Tab. 5.1. It has previously been outlined how diverse interaction mechanisms for particle interactions, and the corresponding rates, have been thoroughly examined. All these interactions are encompassed within the simulation; nevertheless, the results are ultimately determined by the predominant interactions.

In  $S_1$ , the protons are accelerated to energies of  $E_{\rm max}=6\times 10^{16}$  eV, with the dominant energy loss mechanism being photohadronic interaction. This results in the production of secondary particles, including  $\pi^\pm, K^\pm, K_L^0$  and  $\mu^\pm$ , which are unstable but have lifetimes sufficient to interact in the acceleration region. Stable secondary particles, such as photons and neutrinos, are also created, and their behavior will be analyzed subsequently. Charged pions loose energy primarily through synchrotron radiation. The creation of high-energy pions is possible due to the high proton energies. However, the predominant loss of energy for these pions limits their energies to  $E_{\rm max}=3\times 10^{15}$  eV. Muons undergo an even more pronounced loss of energy via inverse Compton radiation and subsequently decay at energies  $E_{\rm max}=2\times 10^{13}$  eV without further interaction. As a result, in  $S_1$ , for muons and pions, mainly decay products are expected to occur as secondary particles.

In  $S_1$ , for several reasons, the most interesting secondary particles are kaons. Firstly, it is also true for charged kaons that their maximum energy is limited by synchrotron radiation, but at higher energies than the maximum proton energy. As a result, kaons can produce the highest energy secondary particles. Due to the dominant synchrotron radiation, only secondary particles from direct kaon decay are expected in first-order. However, as the photohadronic rate is also efficient, kaons may be trapped in the acceleration region long enough to also interact via photohadronic interactions. Nevertheless, kaons produce a variety of secondary particles that eventually lead to neutrinos and photons. Secondly, charged kaons have an energy range in which photohadronic interaction is the dominant interaction, and so for energies up to  $E_{\rm max} = 4 \times 10^{15}$  eV, secondary

**Table 5.1:** Conclusion of particle behavior in the acceleration regions  $S_1$  and  $S_2$ . It details the calculation of maximum energy  $E_{\rm max}$ , the dominant energy loss mechanism and the anticipated secondary particles, categorized as stable or possessing sufficient lifetime to interact. Note that the symbol  $\nu$  is employed to denote all neutrino flavors and their corresponding antiparticles.

		$S_1$	S <sub>2</sub>
р	E <sub>max</sub> [eV]	$6 \times 10^{16}$	$3 \times 10^{16}$
	limiting rate	$t_{\mathrm{p}\gamma}^{-1}$	$t_{ m syn}^{-1}$
	main secondaries	n, $\pi^\pm, K^\pm, K^0_L, \mu^\pm, \nu e^\pm \gamma$	-
$\pi^{\pm}$	$E_{\rm max}$ [eV]	$3 \times 10^{15}$	-
	limiting rate	$t_{ m syn}^{-1}$	$t_{ m dec}^{-1}$
	main secondaries	$\mu^{\pm}, \nu$	$\mu^{\pm}, \nu$
K <sup>±</sup>	$E_{\rm max}$ [eV]	$9 \times 10^{16}$	-
	limiting rate	$t_{ m syn}^{-1}$	$t_{ m dec}^{-1}$
	main secondaries	$\pi^\pm, \mu^\pm, \nu$	$\pi^\pm, \mu^\pm, \nu$
	E <sub>max</sub> [eV]	$4 \times 10^{13}$	-
$K_L^0$	limiting rate	$t_{\mathrm{p}\gamma}^{-1}$	$t_{ m dec}^{-1}$
	main secondaries	$\pi^\pm, \mu^\pm, \nu$	$\pi^\pm, \mu^\pm, \nu$
$\mu^{\pm}$	E <sub>max</sub> [eV]	$2 \times 10^{13}$	$2 \times 10^{14}$
	limiting rate	$t_{ m IC}^{-1}$	$t_{ m IC}^{-1}$
	main secondaries	$e^{\pm},  u$	$e^{\pm}, v$

particles also appear from interactions with photons. Finally, neutral kaons ( $K_L^0$ ) do not interact via synchrotron radiation, and thus photohadronic interaction is the dominant energy loss mechanism for all energies down to  $E_{\rm max}=4\times10^{13}$  eV, leading also to secondary particle production via interactions. Note that neutral kaons are not accelerated and so can only have energies corresponding to the primary proton.

In the case of  $S_2$ , the protons are initially accelerated to lower energies ( $E_{\rm max} = 3 \times 10^{16}$  eV), and the dominant interaction is that of synchrotron radiation. This results in negligible secondary particle production. However, it should be noted that proton-proton interactions are relatively more significant, and photohadronic interactions also occur. As all interactions are stochastic, it is possible for secondary particles to be created in the acceleration region. Pions and both charged

and neutral kaons immediately decay without interaction, while muons loose much energy via inverse Compton scattering, as their intrinsic maximum energy is given as  $E_{\rm max}=2\times10^{14}\,{\rm eV}$  in this region. In the acceleration region, it is therefore expected to create fewer secondary particles and particles of lower energy. However, it is necessary to analyze which interactions may appear after leaving the acceleration region.

# 5.2 Particle Spectrum on Earth

In order to produce a spectrum of high-energy protons and associated secondary particles that can be compared to experimental results, it is important to analyze all the interactions of the particles on their way to Earth introduced by Chapter 4.

The final neutrino spectrum measured on Earth is composed of neutrinos produced in the acceleration region and neutrinos from secondary decay outside the acceleration region. In addition, high-energy protons can interact with the surrounding medium, causing inelastic scattering to produce more secondary particles and finally neutrinos between the acceleration region in Cygnus X-3 and Earth. The same arguments hold for photons. Photons also interact with the medium on their way to Earth, and the optical depth must be included in the photon spectrum. As the main interaction for high-energetic photons is pair production, they do not cause secondary particles of interest. It is therefore important to consider how much of the initial photon spectrum is absorbed. The resulting electrons and positrons propagate, but can also annihilate again, producing two high-energy photons. This process can occur several times, shaping the photon spectrum. However, it is sufficient for first estimates to neglect further secondary interactions in the pair production process.

Protons are stable and reach the Earth. However, they are deflected by magnetic fields and contribute to the diffuse cosmic ray spectrum. Proton interactions with the medium after leaving the acceleration region are included to give a complete picture of what secondary particle spectra are expected. All secondary particles considered are unstable and decay before reaching the Earth, except photons and neutrinos (electrons are not of interest in this context).

# 5.2.1 Proton Interaction Depth

The main proton interaction mechanisms in the energy regime of interest are inelastic proton-proton collisions and photohadronic interactions. Proton interactions with other mesons are not considered as they are not sufficiently stable and therefore decay in the narrow edge of the acceleration region. Based on

the interaction timescales for the respective interaction mechanism given in Chapter 4, the proton interaction depth of the protons can be calculated by

$$\tau_{pi}(E_p) = \int_{r_1}^{r_2} \frac{t_{pi}^{-1}(E_p, r)}{c} dr.$$
 (5.3)

In this case, the index i represents either a proton for hadronic interactions or a photon for photohadronic interactions. Due to lower magnetic field behind the acceleration region, ballistic propagation is considered for protons. Note that this is a more reasonable approach in  $S_2$ . The proton interaction depth  $\tau$  is unitless and represents the proton analogue for optical depth. Hence, for values of  $\tau > 1$ , the proton is assumed to be interacting and the corresponding secondary particles are produced.

However, as interaction is a stochastic process, it is important to consider the interaction probability. The general interaction probability for particles in a medium with a given optical depth or interaction depth is expressed by



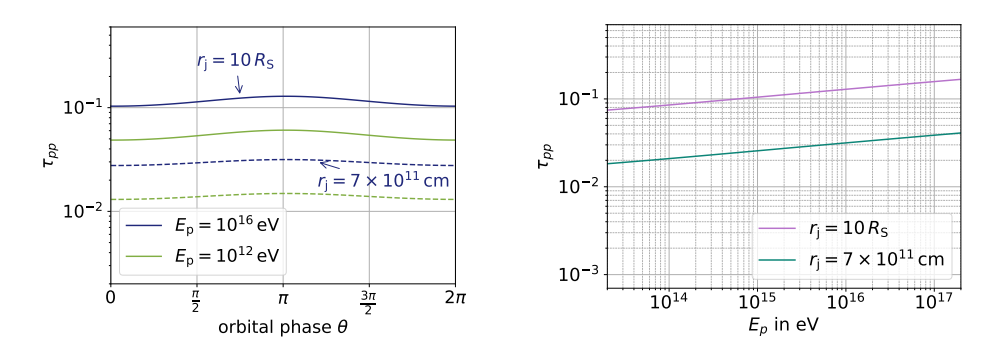


**Figure 5.10:** *Left*: The proton interaction depth  $\tau_{pp}$  depending on orbital phase  $\theta$ , proton energy  $E_p$  and distance do the black hole  $r_j$ . *Right*: Interaction depth of high-energy protons originating from the jet depending on their energy.

First, hadronic interactions are taken into account by using Eq. (5.3). For the integration, the extension  $r_2$  of the Wolf-Rayet wind of Cygnus X-3 is assumed to be of the order of  $10^3$  AU, and  $r_1$  denotes the point where the proton leaves the acceleration region (marked with  $r_j$  in Fig. 5.10). Proton interactions with the interstellar medium are assumed to be negligible for the Cygnus X-3 distance. The integration is performed in the jet direction  $r_j$ , however, the hadronic energy loss rate depends on the distance to the Wolf-Rayet star. As a result, the orbital

period of Cygnus X-3 contributes to  $\tau_{pp}$  by taking into account the geometrical considerations for the non-precessing jet. The integration has to be performed over the distance for different orbital periods.

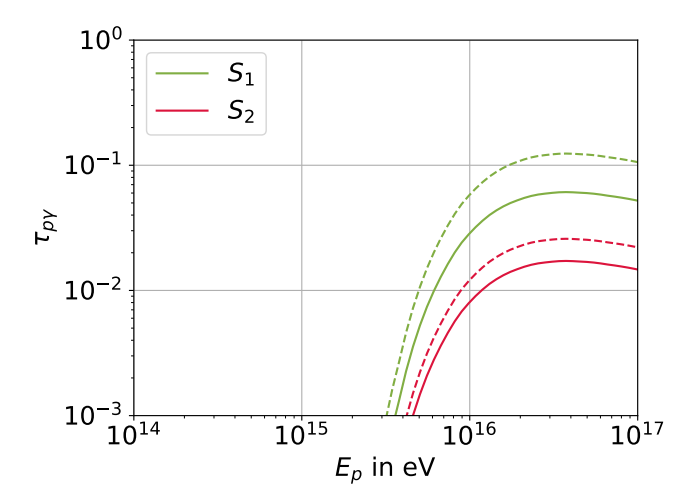
As demonstrated in Fig. 5.10, the orbital period affects the interaction depth in a manner that is distinct depending on the location of the acceleration region, denoted by  $r_j$ . This phenomenon can be understood through the symmetry of the system. In the jet, the orbit leads to modulated proton densities. The longer the particles propagate through the dense medium, the stronger the orbital modulation appears, resulting in a more significant orbital modulation for  $S_1$ .

Fig. 5.10 illustrates the opacity  $\tau_{\rm pp}$  for protons of different energies. It can be seen that the opacity of protons increases for high-energy protons by a factor of 2. Note again, it is important to consider the position of the protons in the jet (in  $S_1$ ). Overall, the orbital phase  $\theta$ , the particle energy  $E_{\rm p}$  and the jet position  $r_{\rm j}$  affect the proton interaction depth in detail.

It should be noted that in these calculations no scattering and a straight propagation down to earth is expected. It is important to compare the interaction depth outside the acceleration region with the interaction depth inside the acceleration region. Within the accelerating region, all charged particles perform a random walk. Following the initial simulations that exclusively considered interactions within the acceleration region, it is necessary to evaluate the influence of the interactions outside the acceleration region. This will determine the relevance of these interactions and whether they should be incorporated into the simulations. Alternatively, it may be concluded that the particle spectrum on Earth is already determined to first order for all particles leaving the acceleration region.

In addition to the proton-proton interaction, the interaction depth is calculated also for photohadronic interactions by using Eq. (5.3). Photons of all energies propagate with constant velocity c and therefore, in all interactions with photons an interaction angle appears. In the acceleration region, the protons scatter on the magnetic field irregularities. The result is photohadronic interaction without a preferred scattering angle. After leaving the interaction region, the protons and photons of interest are directed towards Earth. In accordance with this theoretical framework, the exclusive photon field that governs interactions beyond the acceleration region is the stellar photon field for particles propagating towards Earth. This assertion can be substantiated by examining the interaction energies in the proton rest frame (see Chapter 4). For particles propagating in the same direction, the interaction angle approaches zero, consequently resulting in a vanishing interaction cross section. Therefore, the sole photon field that is taken into account for additional interactions occurring beyond the acceleration region in the jet is the stellar photon field.

The interactions with the stellar photon field are contingent on the distance to



**Figure 5.11:** Interaction depth for protons in  $S_1$  and  $S_2$  and interacting with stellar photons. The interaction depth is modulated by the orbit for stellar photon interactions, and the solid line corresponds to inferior conjunction, the dashed lines to superior conjunction.

the Wolf-Rayet star, and thus implicitly on  $r_{\rm j}$ , the orbital phase  $\theta$  and the proton energy  $E_{\rm p}$ . As illustrated in Fig. 5.11, the interaction depth for protons in the jet is depicted on the left-hand side.  $\tau_{\rm p\gamma}$  is visualized for both regions  $S_1$  and  $S_2$  with superior and inferior conjunction, respectively. It has previously been determined that interactions with the stellar photon field have a high proton threshold energy due to the temperature of the blackbody spectrum. Furthermore, the phase modulation observed in hadronic interactions is also applicable in this case, resulting in higher  $\tau_{\rm p\gamma}$  in superior conjunction compared to inferior conjunction. In  $S_1$ ,  $\tau_{\rm p\gamma}$  becomes significant exclusively for proton energies above  $E_{\rm p}=5\times10^{15}~{\rm eV}$  and the signal is phase modulated (with the largest attenuation depth in superior conjunction). However,  $\tau_{\rm p\gamma}$  is maximum at  $E_{\rm p}=5\times10^{16}~{\rm eV}$  and approximately at  $\tau_{\rm p\gamma}=0.1$ .

# 5.2.2 Optical Depth

For high-energy photons, the optical depth  $\tau_{\gamma\gamma}$  in the jets can be calculated using the Eq. (4.34). In the case of photon interactions in the jet, the same reasoning applies as for protons interacting in the jet on their way to Earth.

In Fig. 5.12, the opacity of photons propagating towards Earth and interacting with the Wolf-Rayet photon field is depicted as a function of different photon energies. Note that the interaction angle is maintained constant and the star is

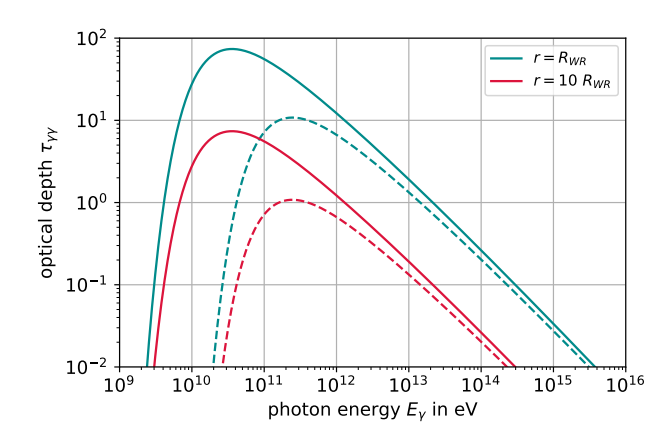


**Figure 5.12:** Modulated optical depth for two different distances two Wolf-Rayet star  $r_{\text{WR}}$ . The solid lines represent a scattering angle of  $\pi$  and thus a head on collision. The dashed lines represent photon interaction with an angle  $\vartheta = pi/4$ .

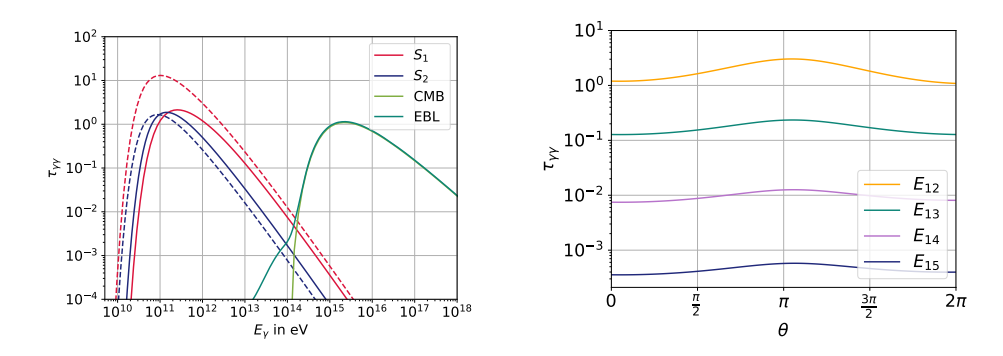


**Figure 5.13:** *Left*: Optical depth for photons  $\tau_{\gamma\gamma}$  in the jet for  $S_1$  and  $S_2$ , due to pair production with stellar photons and EBL photons based on the model in Ref. [67]. The solid line represents inferior conjunction, whilst the dashed line denotes superior conjunction. *Right*: Orbital modulation of  $\tau_{\gamma\gamma}$  for different photon energies  $E_i$  with i denoting for magnitude in eV.

approximated as a point source. It is evident from the figure that the opacity undergoes a change for varying interaction angles. The peak shifts to higher energies for narrow interaction angles, which is valid as the head-on collision is the most effective interaction in terms of energy transfer. The distance to the photon source affects the height of the peak, as might be expected. Within the scope of

this thesis, the formation of electromagnetic cascades is neglected, which would shift photon energy by a factor  $10^{-3}$ . The calculations of interactions behind the acceleration region serve as a preliminary approximation, indicating the spectra that may be expected at Earth.

In the context of high-energy photons propagating towards Earth, the interaction angle with the stellar photons changes, with the Wolf-Rayet star being regarded as a point source by the jet photons. Integration over the distance to Earth results in an optical depth of the combined interaction angles, contingent on the photon position, as illustrated in Fig. 5.13. For photons with significant distance to the Wolf-Rayet star ( $r_i = 10^{14}$  cm), the interaction angle declines and thus the optical depth becomes zero. However, the high-energy photons interact with the stellar photons in the broader circumference of the system (see Figure 5.13). The solid line in Figure 5.13 represents inferior conjunction and the jet photons propagate instantaneously against the star. The dashed lines represent superior conjunction, where the jet elongates closer to the star. Due to the long distance, photons are propagating close to the star, resulting in significant variations in optical depth in  $S_1$  with orbital phase. The orbital modulation is depicted in the Figure on the right side, and it can be seen in both graphs that the orbital modulation affects the peak optical depth more than the edges. As demonstrated in Fig. 5.13, for photons with energies above  $E_V = 10^{15}$  eV, the medium is transparent for the respective photons.

In addition, high-energy photons propagating toward Earth can interact with the cosmic microwave background (CMB) and the extragalactic background light (EBL). The interaction depends strongly on the redshift and not on the orientation of the geometry of the system. The model used to approximate the EBL is taken from Ref. [67]. It is shown in Figure 5.13 that the intergalactic medium becomes opaque for photons with energies above  $E_{\gamma} = 10^{15}$  eV. This may have a significant effect on the photons of interest in this work and must be taken into account.

# 5.2.3 Comparative Analysis

The purpose of this section is to provide an overview of the interactions that have a lasting effect on the spectrum on Earth after leaving the acceleration region. The interaction depth can be calculated using Eq. (5.3) as integration over the relevant distance. However, this calculation is not trivial for the particles in the acceleration region, as they perform a random walk. Therefore, for an initial estimate of the interaction depth, the simulation results will be used beforehand without taking into account the interactions outside the acceleration region. By

taking the fluxes  $\Phi$ , the effective interaction depth in the acceleration region can be approximated by

$$\Phi_{\nu} = \tau_{\text{eff}} \Phi_{\text{p}} \langle y \rangle, \tag{5.5}$$

with  $\langle y \rangle$ , being the inelasticity of the interaction. The inelasticity is estimated to be  $\langle y \rangle \approx 0.2$ , as referenced in the literature [45]. Utilizing Fig. 6.1, one obtains  $\Phi_{\nu}/\Phi_{\rm p} \approx 0.01$  for high energies in both regions, while precise energy modulation is neglected, resulting in an effective interaction depth of  $\tau_{\rm eff} = 0.05$ . As previously elaborated, secondary particles are primarily caused by photohadronic interactions. Accordingly, the interaction depth due to photohadronic interactions, which is of the order of the effective interaction depth, i.e. the order of 0.05 in this case, is a key factor in the secondary spectrum on Earth and must be considered in the simulation. Furthermore, the interaction depth of hadronic interactions in this regime indicates that proton-proton interactions outside the acceleration region may modulate the secondary signal significantly, compared to what is expected based on only photohadronic interactions. Based on these arguments, proton interactions are considered to be relevant outside the acceleration region in  $S_1$  and  $S_2$  if  $\tau \gtrsim 10^{-2}$ .

**Table 5.2:** Interaction depth (protons) and optical depth (photons) are demonstrated at an energy of  $E=10^{15}$  eV in  $S_1$  and  $S_2$ . It is also marked for those configurations the energy interval at which the respective  $\tau$  becomes higher than the critical  $\tau_{\rm crit}$ , which is  $\tau_{\rm crit}=10^{-2}$  for protons and  $\tau_{\rm crit}=1$  for photons.

	S <sub>1</sub>		$S_2$	
	$\tau(10^{15}  {\rm eV})$	$E$ [eV], $\tau \gtrsim \tau_{\rm crit}$	$\tau(10^{15}{\rm eV})$	$E$ [eV], $\tau \gtrsim \tau_{\rm crit}$
$ au_{ m pp}$	$\approx 10^{-2}$	$\geq 10^{13}$	$\approx 2 \times 10^{-2}$	$\geq 10^{13}$
$ au_{\mathrm{p}\gamma}$	$< 10^{-3}$	$\geq 4 \times 10^{15}$	-	$\geq 10^{16}$
$ au_{\gamma\gamma}$	1	$3 \times 10^{10} - 3 \times 10^{12}, 10^{15}$	1	$3 \times 10^{10} - 3 \times 10^{11}, 10^{15}$

Both the interaction depth for protons and the optical depth for photons are presented in Tab. 5.2. It can be concluded for  $S_1$  that proton-proton interactions are dominant for energies up to  $E = 10^{16}$  eV, and for all proton energies in the simulation (starting at  $E_p = 10^{13}$  eV) hadronic interactions appear to be noteworthy in their propagation towards Earth. For protons with energies above  $E_p = 5 \times 10^{15}$  eV, photohadronic interactions appear, affecting the spectrum at very high energies. Due to the aim of this work, it has to be mentioned that the energy regime around  $E_p = 10^{16}$  eV is of major interest. Both photohadronic and

proton interactions can produce important secondary particles during proton propagation beyond the acceleration region. Especially at these energies, the medium is transparent to photons. Based on these calculations, the medium is expected to be opaque to photons in the lower energy regime at  $E_{\gamma} \approx 10^{11}$  eV. In conclusion, the neutrino flux on Earth is expected to be higher than in calculations considering only the acceleration regime. Furthermore, it is assumed that photons with higher energies can escape from the medium and be measured on Earth.

In  $S_2$ , the same arguments hold while the interactions appear less dominant due to the location of  $S_2$  with especially photohadronic interactions becoming relevant for proton energies above  $E = 10^{16}$  eV. It is mentioned here, that orbital modulation is less significant in  $S_2$  due to the less dense medium. Evidence has been presented in this work demonstrating the expectation of a signal with orbital modulation, particularly in  $S_1$ . Nevertheless, given the objective of this study is to examine the potential for high-energy photons and neutrinos, a mean interaction probability has been incorporated into the simulation. It is noteworthy that phase modulation should manifest distinctly in the measurements.

# 5.3 Simulation Setup

In the following, the simulation for the particle acceleration in the vicinity of Cygnus X-3 is carried out in the two important acceleration regions  $S_1$  and  $S_2$ , which are described in Section 3.4. This section explains in detail which parameters and particle interactions have been integrated into the simulation in order to provide a detailed picture of how final calculations of the particle spectra are performed. The different simulation scenarios with the corresponding parameters are given in Tab. 5.3.

A flowchart that roughly explains the structure of the simulation is shown in Fig. 5.14. In the interest of numerical time, protons with energies of  $E_{\rm p}=10^{13}$  eV are inserted into the acceleration region. The time step is chosen in the order that it is smaller than all the interaction timescales considered above. For each particle with a given energy E the corresponding energy loss rate  $t_{\rm int}^{-1}$  is calculated. Using Eq. (4.1), for all interactions in the continuous energy loss approximation (including acceleration)  $t_{\rm int}^{-1}$  the specific energy change  $\Delta E$  can be calculated as

$$\Delta E = E t_{\text{int}}^{-1}(E) \Delta t. \tag{5.6}$$

The energy chances for the respective interactions are added up at each time interval to calculate a new particle energy and, based on that, a resulting interaction timescale. This principle is used for all interactions except photohadronic

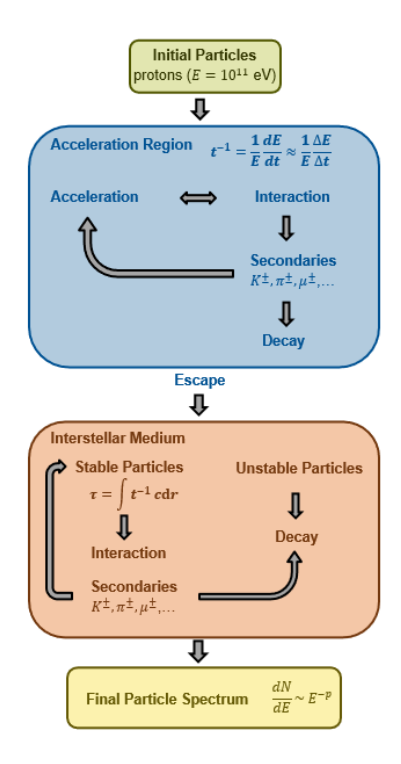


Figure 5.14: Flowchart showing the structure of the final simulation program.

interactions, as these interactions are dominating secondary production inside the acceleration region.

In order to accurately calculate photohadronic interactions, the interaction probability is calculated for each time step as

$$p_{\rm int} = \exp(-t_{\rm int}^{-1} \Delta t). \tag{5.7}$$

A random number is generated determining whether or not an interaction occurs. For an interaction, all particle information is passed to the SOPHIA program. SOPHIA has already been introduced in Section 4.4 and an extended version of the algorithm is used to calculate not only proton-photon interactions but also photomesonic interactions as it may appear for kaons and pions. In SOPHIA, it is possible to specify which of the unstable particles decay and which do not. In this setting, kaons, pions and muons do not decay immediately in the acceleration region and are considered as temporarily stable. Hence, they are reinserted into the acceleration region with the space-time coordinates of the primary particle.

$R_{\mathrm{WR}}$	$6 \times 10^{10}  \text{cm}$
d	8 kPc
a	$3 \times 10^{11}  \mathrm{cm}$
$v_{ m wind}$	$10^8  \mathrm{cm/s}$
$\dot{M}$	$10^{-5}M_{\odot}/\mathrm{yr}$
$M_{ m WR}$	$50M_{\odot}$
T	$10^5\mathrm{K}$
$\Delta R$	$10^7  \mathrm{cm}$
$l_{\rm acc}, S_1$	$5 \times 10^7  \mathrm{cm}$
$l_{\rm acc}, S_2$	$1.5 \times 10^{11}  \text{cm}$
$r_{\rm cr}, S_1$	$10R_{ m S}$
$r_{\rm cr}, S_2$	$7 \times 10^{11} \mathrm{cm}$
$\partial_{j}$	9°
$\phi_{ m j}$	31°
$B_0$	$2.1 \times 10^7 \mathrm{G}$
$\delta$	0.65
$M_{ m BH}$	$20M_{\odot}$
$\dot{M}_{ m acc}$	$4.4 \times 10^{-7}  M_{\odot}/\mathrm{yr}$
P	4.8 h
$artheta_0$	$12^{\circ}$
$r_{ m in}$	$6R_{ m S}$

**Table 5.3:** Used parameters for different simulation scenarios  $K_i$ .

In the acceleration region, they are treated by the same logic as protons, interacting for each time interval. Their decay rates have already been analyzed. A decay probability is introduced into the program with the same logic as the interactions with the Eq. (5.7) for the initial particles.

 $8 \times 10^8 \, \text{cm}$ 

As explained in Section 2.5, both magnetic reconnection and diffusive shock acceleration accelerate protons in such a way that they produce a power-law spectrum  $dN/dE \sim E^{-k}$ . Following the considerations in Ref. [1], for each step i in the simulation, a particle gains energy such that  $E_i = (1 + \Delta E)E_{i-1}$  and for the particle number inside the acceleration region,  $N_i = (1 - p_{esc})N_{i-1}$  holds. In general, after n acceleration cycles, it can be stated for energy and particle number that

$$E = (1 + \Delta E)^{n} E_{0},$$

$$N = (1 - p_{esc})^{n} N_{0},$$
(5.8)

where index 0 denotes the initial parameter. Using basic logarithmic considerations, the integrated particle spectrum is described by the escape probability and the energy change as

$$N(E) = N_0 E^{\frac{\ln(1 - p_{\rm esc})}{\ln(1 + \Delta E)}}.$$
 (5.9)

Since the energy change is known, the slope k of the spectrum  $\mathrm{d}N/\mathrm{d}E \sim E^{-k}$  can be used to calculate  $p_{\mathrm{esc}}$ . For particle spectra for test particle approximations caused by diffusive shock acceleration, the slope follows k=2 [68]. In more realistic set-ups one finds often steeper spectra, thus k=2.3 is used here [69]. However, particle spectra in the case of magnetic reconnection follow different slopes depending on the exact mechanism. Here the magnetic reconnection is relativistic, which is correlated with a slope of k=2.3 [70]. Therefore, the expected power-law is equal in both scenarios and is used to determine the escape probability

$$p_{\rm esc} = 1 - \exp\left((-k+1)\ln\left(1 + \frac{\Delta E}{E}\right)\right) \tag{5.10}$$

for each time step in the simulation.

The introduction of a particle escape mechanism based on  $p_{esc}$  in Eq. (5.10) determines the particle spectrum of the initial particles. However, there is also a geometric constraint. If a particle leaves the acceleration region in a time step, it will not be accelerated further for obvious reasons. The geometric conditions are different for the two acceleration mechanisms in  $S_1$  and  $S_2$ . Both are described in more detail in Section 3.4. In  $S_1$ , the reconnection parameters are taken from Ref. [45], which introduces a cylindrical acceleration region with radius  $\Delta R$  and height  $l_{acc}$ . For  $S_2$ , in the case of shock acceleration, the Hillas criterion ( $R_L < R$ ) is applied assuming the size of the extension of the shock R corresponds to the geometry of the jet at the edge of the cocoon.

After leaving the acceleration region, the particles are assumed to propagate ballistic in the interstellar medium towards Earth. In the vicinity of the accelerator region, the medium is denser than the average interstellar medium due to the Wolf-Rayet wind. This is particularly important for specific orbital configurations in the respective acceleration regions, as the proton density depends on the relative position to the star.

There is a possibility of unstable secondary particles escaping the acceleration region. However, without calculation it is taken that unstable secondary particles besides neutrons decay in the vicinity of acceleration region. The program structure forces immediate decay of unstable secondary particles when they leave the acceleration region. Thus behind the acceleration region only protons,

photons and neutrinos enter the region beyond without protons being further accelerated. However, protons may interact with the ambient photons and protons. Additionally, the created  $\gamma$ -rays interact via pair production with stellar photons. The interaction probability is calculated from the optical depth for photons and the interaction depth for protons with Eq. (5.4). The neutrinos escape from the acceleration region without any interaction, thus the neutrino spectrum is not modified by any interaction. For the interactions, the calculated interaction probability is compared with a random number. For photohadronic interactions, the SOPHIA algorithm is used again, where all secondary particles are taken as unstable. For proton-proton interactions, the QGS-JET algorithm is used, which was introduced before (see Chapter 4) and is a Reggeon-based algorithm for calculating inelastic scattering [60]. All unstable secondary particles are transferred immediately to SOPHIA to decay finally. All these considerations lead to the spectra for photons and neutrinos expected to be measured on Earth originating from of Cygnus-X3.

Due to the complexity of the program, certain aspects of secondary particle interactions are not fully incorporated. The previous analysis has shown that  $S_1$  is the more promising acceleration region, thus the focus in the program development was set there. In the interest of accuracy the numerical capacity have been used for precise particle interactions thus neglected acceleration mechanisms of temporarily stable particles. Nonetheless, without further calculation it is argued here that this acceleration applies mostly to kaons, which show to neither dominate the neutrino spectrum nor the  $\gamma$ -ray spectra. Additionally, low energy pions would be accelerated, however as photohadronic interactions appear for high proton energies the resulting pions have already high energies thus integration of secondary acceleration lead to disproportionate more numerical capacity with low expected outcome.

To calculate the exact particle spectra and compare them with actual measurements, it is important to find a suitable standardization and to be able to specify units reasonably. As explained in Chapter 2, the maximum luminosity of the source is given by the Eddington luminosity  $L_{\rm edd}$ . It has to be taken into account that the efficiency  $\chi$  is of crucial importance for the Eddington luminosity. For Cygnus X-3, this has not yet been clearly determined and since there are also indications of super-Eddington accretion [71], an optimistic efficiency of  $\chi=0.1$  is chosen here, resulting in  $L_{\rm edd}=2.5\times10^{39}$  erg/s.

The proton spectrum is now derived from the simulation, incorporating all proton interactions. However, the proton energy loss is not included in the analysis. The differential spectrum E dN/dE is presented in Fig. 5.15 for both regions. Hence, the cosmic ray luminosity is calculated by

$$L_{\rm CR} = \frac{1}{T} \int E \frac{\mathrm{d}E}{\mathrm{d}N} \mathrm{d}E,\tag{5.11}$$

with T being a factor that accounts for the correct normalization of the luminosity dimension. The calculated result based on the Eddington luminosity can be taken now and it yields T = x for  $S_1$  and T = y holds for  $S_2$  respectively. An useful approach is to present the spectra in terms of the differential particle flux on Earth, leading to

$$\frac{\mathrm{d}N}{\mathrm{d}A\mathrm{d}E\mathrm{d}t} = \frac{\mathrm{d}N}{\mathrm{d}E} \frac{1}{4\pi d^2 T}.$$
 (5.12)

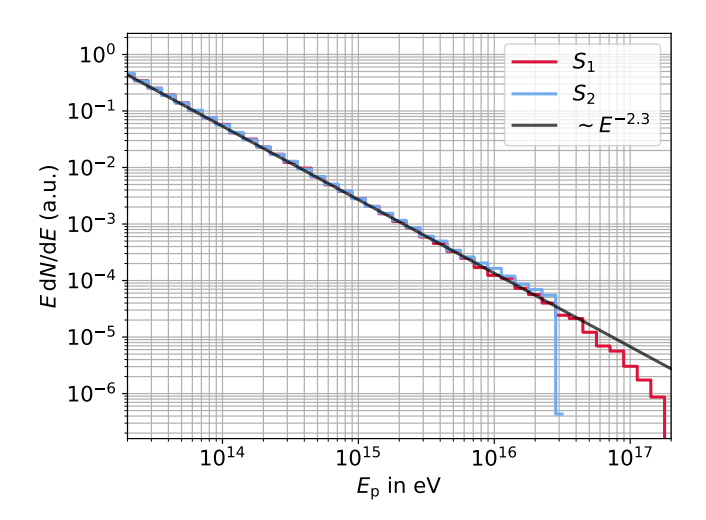


**Figure 5.15:** Generated spectrum for protons in the simulation for regions  $S_1$  and  $S_2$ . This spectrum is used for normalization based on Eq. (5.11) as protons do not actually loose energy in interactions.

As demonstrated in Fig. 5.15, the spectrum of the simulation provides a initial indication of the proton spectrum  $E\frac{dN}{dE}$ . The proton spectrum can be adequately described in both acceleration regions by a power-law  $E^{-2.3}$ , as determined by the program structure (see Figure 5.14). Furthermore, the cut-off due to proton interactions appears at energies that are expected based on previous analytical estimates. The protons in  $S_1$  have a cut-off at high  $E_p = 10^{16}$  eV, with a flux decrease leading to some protons reaching  $E_p = 10^{17}$  eV. In the  $S_2$ , the step cut-off manifests at lower energies, at approximately  $E_p = 2 \times 10^{16}$  eV.

In the following, the simulations for the two different acceleration regions  $S_1$  and  $S_2$  are examined, focusing on  $S_1$ . The interactions for each type of particle discussed in the previous analysis have been included in the program. The proton spectrum is examined first, as important information about the simulation results can be derived from its spectrum. Then, the secondary particle spectra can be studied in more detail. Photons are produced within the acceleration region and beyond, while the PeV photon spectra are compared with data from the LHAASO collaboration [9]. The resulting neutrino spectra will be studied specifically for  $S_1$  by distinguishing between the neutrino flavors produced for the respective regions and decay channels.

It is important to mention that antiprotons are produced as secondary particles, but play a minor role. Therefore, it was decided to present and analyze only the proton spectra, especially since the proton spectrum is not trivial to measure in connection with Cygnus X-3 as a source. Based on the considerations for normalization, all spectra are presented as particle flux per surface area and time on Earth. Since dA and dt are energy independent, the power law form  $E^2 \mathrm{d}N/\mathrm{d}E \sim E^{-0.3}$  does not change for the following representation  $E^2 \mathrm{d}N/(\mathrm{d}E\mathrm{d}A\mathrm{d}t) = E^2\phi$ .

# **6.1 Acceleration Region** $S_1$

For low energies in Fig. 6.1, the proton spectrum follows the power law  $E^2 \mathrm{d}N/\mathrm{d}E \sim E^{-0.3}$  as expected in Section 5.3 for initial protons. First deviations from this shape can be seen at  $E_p = 10^{16}$  eV, with a smooth cut-off leading to proton energies up to  $10^{17}$  eV, which is in good agreement with the estimations in Chapter 5. The smooth cut-off can be explained by the fact that the acceleration rate (reconnection) and the most efficient energy loss rate (photohadronic) are both in the same order of magnitude at  $E_p = 10^{16}$  eV. The close convergence of the energy loss rates in Fig. 5.2 illustrates the significant probability of protons interacting photohadronically at energies of  $E_p = 10^{16}$  eV. The dotted line in Fig. 6.1 mark the protons that have interacted. The conclusion that mostly high-energy protons interact with both other protons and photons in the surrounding medium is well in line with the theoretical expectations. Due to the logarithmic plot, the number of protons interacting with the surrounding medium after the accelera-

# Chapter 6 Results and Discussion

tion region appears to be of the same order for all proton energies. However, the fraction of interacting protons is significantly larger at high energies, reflecting the higher probability of interaction for PeV protons.

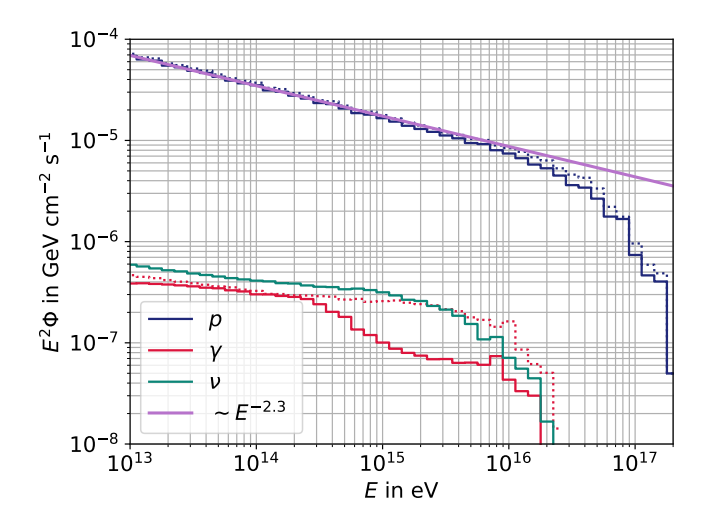


**Figure 6.1:** Final spectra of protons (p), photons  $(\gamma)$  and neutrinos  $(\nu)$  determined from a simulation in the acceleration region in Cygnus X-3 at  $S_1$  and subsequent propagation towards Earth has been determined. The dotted lines represent the particle spectra before interaction behind the acceleration region.

Considering the photon spectrum in Fig. 6.1, it is noticeable that the spectrum before absorption has a shape similar to the proton spectrum, with a cut-off at  $E_{\gamma}=10^{15}$  eV, leading to maximum photon energies in the order of  $E_{\gamma}=10$  PeV. In this energy regime, the photons are expected to propagate towards Earth without interacting with stellar photons from the Wolf-Rayet star, since only photons with energies well below  $E_{\gamma}=10^{14}$  eV are absorbed due to pair production (see Fig. 5.13). However, the photons from the CMB and EBL contribute to pair production with the produced photons. Therefore, the photon spectrum shows strong absorption effects from  $E_{\gamma}=5\times 10^{14}$  eV.

In Fig. 6.2 a comprehensive spectrum of the various photon origins is depicted. In this work, all photons result from neutral pion decay. Note that direct decay into subdominant photons manifests itself, for instance, in the  $K_S^0$ ,  $K_L^0$  or  $\eta$  decays [55]. Consequently, the focus is on the location of the photon production, namely whether the photon production occurs inside or outside the acceleration region. The shape of the photon spectrum points out that most photons with energies above  $E_{\gamma} = 1$  PeV are produced inside the acceleration region. Inside

the acceleration region, the initial protons are accelerated without many interactions up to energies of  $E_p = 10^{16}$  eV (see Fig. 5.2). Protons start to interact significantly at energies around  $E_p = 10^{16}$  eV, producing mostly photons with energies in the range between  $E_{\gamma} = 10^{15}$  eV and  $E_{\gamma} = 10^{16}$  eV.

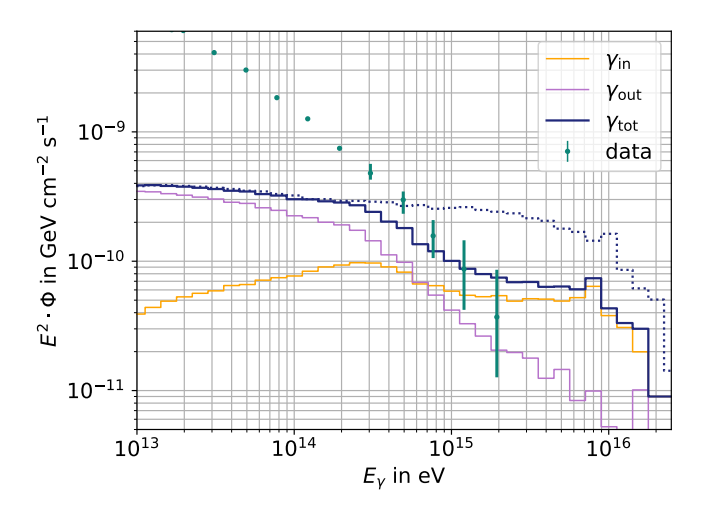


**Figure 6.2:** Photon spectrum obtained from the simulation for  $S_1$ , considering photons from the acceleration region ( $\gamma_{in}$ ) and behind the acceleration region ( $\gamma_{out}$ ). Note that the dotted line marks the spectrum before absorption by the CMB and EBL. The results are compared with measurements from the LHAASO collaboration [9].

After leaving the acceleration region, the protons only loose energy without being accelerated further. Synchrotron losses outside the acceleration region are not considered because they play a subdominant role due to the decrease in the magnetic field. Thus, the photons outside the acceleration region are caused by interactions of the protons with stellar photons and by proton-proton interactions. It has been pointed out that protons of all energies contribute to the proton-proton interactions with the medium behind the acceleration region. The photon spectra from different regions in Fig. 6.2 can be distinguished. The slope of the photons  $\gamma_{\rm in}$  coming from the acceleration region is caused by photohadronic interactions and therefore has a different shape to the proton spectrum in Fig. 6.1. The photons  $\gamma_{\rm out}$  produced behind the acceleration region are caused by proton-proton interactions, resulting in a spectral shape similar to the proton spectrum.

The photon spectrum from the simulation can be compared in Fig. 6.2 with photon data measured by LHAASO from the Cygnus bubble [9]. They found an excess of PeV photons coming from a region including Cygnus X-3 that is lower

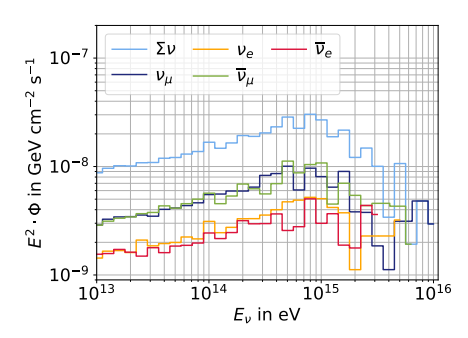
# Chapter 6 Results and Discussion

than the photon flux simulated here. Note that in Figure 6.1 the photon flux is shown as it was generated in the simulation, while in Fig. 6.2 all photon fluxes are modified by a factor  $10^{-3}$  to make them more comparable to the data. This is because the normalization chose an efficiency of  $\chi=0.1$ , corresponding to Eddington accretion, which is an optimistic approach. Furthermore, the cosmic ray efficiency may be low, leading to more energy being released via synchrotron radiation. Thus, the simulation found that the accretion efficiency in Cygnus X-3, or the cosmic ray efficiency, is lower, modifying the spectrum by a factor of  $10^{-3}$ . In addition, the compact object mass was chosen here to be  $20 M_{\odot}$ , while recent studies point to an upper compact object mass of  $M_{\rm BH} < 7 M_{\odot}$  [72]. The compact object mass affects Eq. (2.8) and thus also affects the normalization estimates. Therefore, the results of the simulation can also be interpreted as evidence for a smaller black hole mass in Cygnus X-3.

The total neutrino spectrum produced in  $S_1$  can be seen in Fig. 6.1, which follows a similar shape as the proton spectrum. The neutrino spectrum has a cut-off at  $E_{\nu}=10^{15}$  eV with a decline as steep as the proton spectrum, leading to maximum neutrino energies of  $E_{\nu}=10^{16}$  eV. As with photons, the neutrino spectrum can be analyzed in terms of location. Fig. 6.3 shows the neutrino spectra for a specific neutrino flavor produced in the acceleration region (left) and the neutrino spectra for neutrinos originating outside the acceleration region (right). For both regions, Cygnus X-3 is predominantly a muon neutrino source, producing the expected flavor ratio of  $1_e:2_{\mu}:0_{\tau}$ . This is the resulting flavor ratio for charged pion decay in its dominant decay branch, which leads to a neutrino flavor ratio on Earth of  $1_e:1_{\mu}:1_{\tau}$  [73] due to neutrino oscillations. Furthermore, the shape of the neutrinos from the acceleration region follows the shape of the  $\gamma$ -rays from the acceleration region, leading to the conclusion that both charged and neutral pions are produced in the proton interactions that shape the photon and neutrino spectra.

Beyond the acceleration region, the neutrinos become more abundant for lower energies with a cut-off at  $E_{\nu}=2\times 10^{15}$  eV. This shape can be understood by considering the different proton interactions. Both neutrinos and antineutrinos have the same origin in this picture, and are therefore presented together in Fig. 6.4 for electron neutrinos and in Fig. 6.5 for muon neutrinos. The dominant interaction mechanism of protons behind the acceleration region is the proton-proton interaction. The interaction depth for protons in the stellar wind increases at high energies. The lower interaction depth determines a lower interaction probability for TeV protons, leading to a smaller fraction of initial protons interacting. Thus, both the photon and neutrino spectra decrease with increasing energy.

Photohadronic interactions outside the acceleration region appear only for protons with energies above  $E_p = 10^{15}$  eV, leading to additional neutrino production



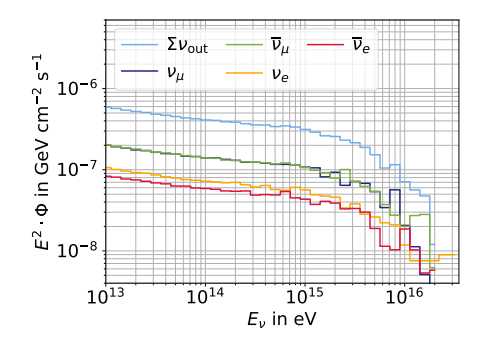


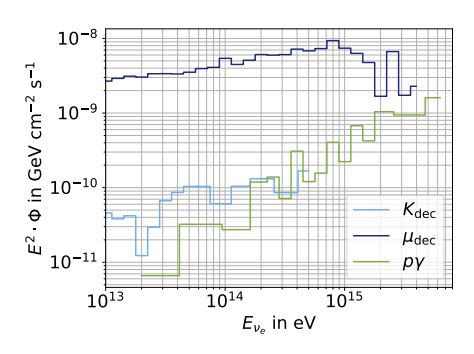
**Figure 6.3:** Spectrum of neutrinos considered for the different neutrino flavors and corresponding antineutrinos. A distinction is made between spectra produced inside the acceleration region (left) and outside the acceleration region (right). The total spectrum of neutrinos coming from the respective location is marked with  $\Sigma \nu$ .

especially at high energies. This interaction is subdominant even at high energies, hence photohadronic interactions appearing outside the acceleration region only marginally influence the photon spectra. For the purpose of completeness, it should be mentioned that for electron neutrinos, neutron decay appears outside the acceleration region. Neutron decay always occurs outside the acceleration region due to the absence of electric charge and the long lifetime of the neutron. The small amount of energy carried by neutrinos from neutron decay can be explained by the rough approximation that the energy distribution in neutron decay is proportional to the masses of the decay particles. This leads to the neutrino energy being approximated by the proportionality  $E_{\nu} \sim m_e/m_p$ . Since the flux is three orders of magnitude smaller than the flux due to proton-proton interaction, it serves as an indicator of the consistency of the program and leads to the conclusion that neutron decay is not an important contributor to the neutrino spectrum on Earth (including the flavor ratio).

Within the acceleration region represented by Fig. 6.4, electron neutrinos mostly originate from muon decay. Kaon decay and direct photohadronic interactions contribute to the neutrino spectrum mostly for energies above  $E_{\nu}=10^{15}$  eV. All secondary particles are produced by photohadronic interactions within the acceleration region. However,  $K^{\pm}$ ,  $K_{\rm L}^0$ ,  $\pi^{\pm}$  and  $\mu^{\pm}$  are re-inserted into the acceleration region to interact and then decay. Thus, neutrinos referred to as originating from photohadronic interactions in the acceleration region are produced by secondary particles that immediately decay in the SOPHIA program. The semileptonic decay of  $K_{\rm S}^0$  is one example where neutrinos are directly produced [55].

Muon decay dominates the neutrino flux from the acceleration region for elec-

# **Chapter 6** Results and Discussion



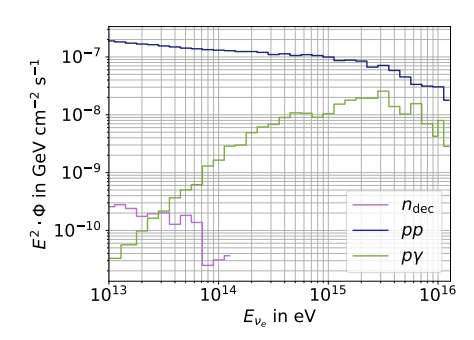
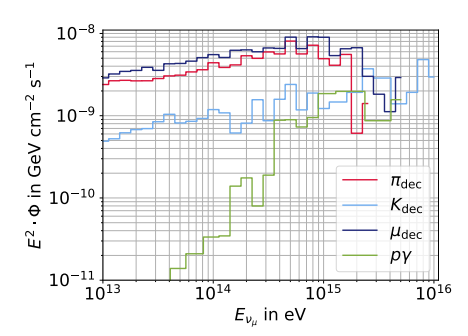


**Figure 6.4:** Spectrum of electron neutrinos taking into account the different decay channels for electron neutrinos, where the spectrum itself includes both neutrinos and antineutrinos. Within the acceleration region (left), electron neutrinos result from kaon decay ( $K_{dec}$ ), muon decay ( $\mu_{dec}$ ), and occur directly in photohadronic interactions ( $p\gamma$ ). Beyond the acceleration region (right), electron neutrinos additionally come from neutron decay ( $n_{dec}$ ), proton-proton interactions (pp).

tron neutrinos. A direct comparison with the muon neutrino spectra inside the acceleration region in Fig. 6.5 shows that the neutrinos produced by muon decay follow the same shape as the muon neutrinos resulting from pion decay. Hence, muons are not significantly produced inside the acceleration region since the pion lifetimes are long enough for the pions to leave the acceleration region. It can be concluded that secondary particles with long lifetimes can propagate and interact inside the acceleration region in  $S_1$  as long as they leave the acceleration region without decaying in the meantime.

For muon neutrinos inside the acceleration region presented in Fig. 6.5, the same picture holds as discussed for electron neutrinos. Pions give rise to neutrinos with maximum energies of  $E_{\nu}\approx 2\times 10^{15}\,\mathrm{eV}$ , which is well in line with expected pion behavior. Pions are lighter than kaons, leading to higher synchrotron energy loss rates, which results in a pion energy limit of an order reflected in the neutrino spectrum.

The general picture for Cygnus X-3 in  $S_1$  based on the simulations yields an efficient proton acceleration up to  $E_p=10\,\mathrm{PeV}$ . In the dense stellar wind, the accelerated protons interact, leading to efficient pion production resulting in  $\gamma$ -rays with maximum energies on the order of  $E_\gamma=10^{16}\,\mathrm{eV}$ . The  $\gamma$ -ray production is efficient due to the chosen accretion efficiency, allowing the conclusion that the LHAASO data can be explained with accretion rates significantly below the Eddington accretion rate. Furthermore, both the neutrino and photon spectra



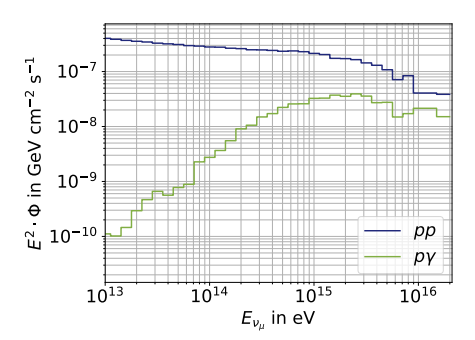


**Figure 6.5:** Muon neutrino spectra including both neutrinos and antineutrinos. Within the acceleration region (*left*), muon neutrinos are produced in kaon decay ( $K_{\text{dec}}$ ), muon decay ( $\mu_{\text{dec}}$ ), pion decay ( $\pi_{\text{dec}}$ ) and directly in photohadronic interactions ( $p\gamma$ ). Beyond the acceleration region (right), muon neutrinos are additionally produced in proton-proton interactions (pp).

indicate that the main secondary particle production occurs beyond the acceleration region in the dense stellar wind due to proton-proton interactions. The secondary particles from the acceleration region are produced by photohadronic interactions. In both proton interaction mechanisms, mainly pions are generated, so Cygnus X-3 efficiently produces neutrinos with a flavor ratio of  $1_e: 2_{\mu}: 0_{\tau}$ .

### **6.2** Acceleration Region $S_2$

The proton acceleration program has also been developed for  $S_2$ , focusing on the protons, photons and neutrinos produced. Since  $S_1$  and  $S_2$  have several key aspects in common, the analysis for  $S_2$  focuses on the differences, and for basic explanations see Section 6.1.

Considering the protons in Fig. 6.6, it is evident that the proton flux follows the predicted power-law  $\phi \sim E^{-2.3}$ . A sharp cut-off appears at  $E_p = 10^{16}$  eV, caused by synchrotron radiation losses and second order photohadronic interactions. Thus, the fraction of the secondary particle flux compared to the proton particle flux is almost three orders of magnitude smaller. However, in an energy range around  $10^{15}$  eV significant secondary production appears implying that the fraction of secondaries increases by more than one order of magnitude.

In general, the proton interactions outside the acceleration region are small. Consequently, the dotted lines visualizing the interactions in the graph are difficult to see. Therefore, it is expected that most of the secondaries are produced inside the acceleration region. For photons, the absorption caused by stellar photons

#### Chapter 6 Results and Discussion

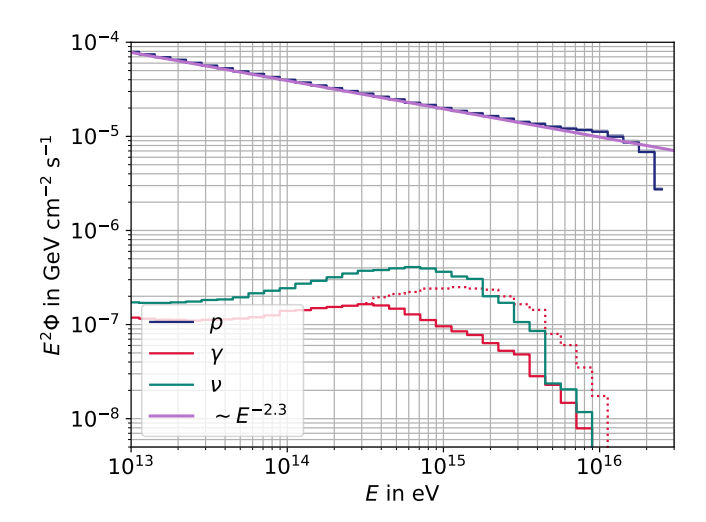


**Figure 6.6:** Final spectrum of protons (p), photons ( $\gamma$ ) and neutrinos ( $\nu$ ) from Cygnus X-3 in  $S_2$ . The dotted lines in the proton and photon spectra represent the spectra before interactions.

is negligibly small and the medium becomes more transparent to photons in  $S_2$  compared to  $S_1$ . The interactions with the CMB and EBL photons are independent of the specific geometry in Cygnus X-3 and therefore lead to the same photon absorption effects as in  $S_1$ . Neutrinos and photons again seem to have the same origin, since their spectral shapes are identical.

For the simulation results in  $S_2$ , the photon spectra are analyzed in more detail, as illustrated in Fig. 6.7. The  $\gamma$ -rays produced in  $S_2$  are mainly generated inside the acceleration region for photon energies above  $E_{\gamma} = 2 \times 10^{14}$  eV. However, some photons are created outside the acceleration region, where the spectrum  $\gamma_{\text{out}}$  in the graph is consequently three orders of magnitude lower than the proton spectrum in Fig. 6.6. This shows that a small fraction of the protons interact beyond the acceleration region, producing  $\gamma$ -rays with energies mainly between  $E_{\gamma} = 10^{13}$  eV and  $E_{\gamma} = 10^{15}$  eV, which are mainly absorbed by interactions with the EBL before reaching Earth.

The photon spectrum for  $S_2$  in Fig. 6.7 extends to energies that can explain the PeV excess photons measured by LHAASO, as do the results for  $S_1$ . The dominant photon absorption is due to interactions with the CMB and EBL, and thus the effects in  $S_1$  for the slope of the photon spectrum appear for  $S_2$  as well. Therefore, the shape at high energies fits the data with the particle flux. However, it is higher than the measured data by a factor of  $10^3$ , as is the case in  $S_1$ . The same

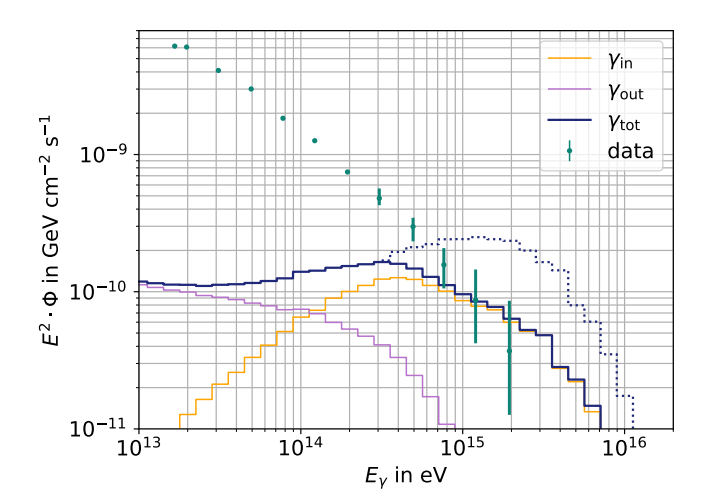


**Figure 6.7:** Photon spectrum obtained from the simulation for  $S_2$  considering photons originating from the acceleration region ( $\gamma_{in}$ ) and those on their way to Earth behind the acceleration region ( $\gamma_{out}$ ). Note that the dotted lines mark the spectra before absorption in the surrounding medium. The results are compared with measurements from the LHAASO collaboration [9].

correction factor for the photon spectrum in  $S_2$  implies the same explanations as for Cygnus X-3 in  $S_1$ .

The photon spectra simulated in  $S_1$  and  $S_2$  can be compared qualitatively (Fig. 6.2 and Fig. 6.7). Both results are able to explain the measured data, where the mass accretion rate has to be corrected by a factor of  $10^{-3}$  in both cases. The photon spectra for  $\gamma_{\rm in}$  peak at almost the same energy, but in  $S_1$  the edges are less steep. The cut-off in  $S_1$  to higher energies is smoother because photons are produced in sufficient quantities for these energies due to dominant photohadronic interactions. In contrast, in  $S_2$  synchrotron losses dominate and suppress the photohadronic energy loss rate. The steep increase in  $S_2$  for energies below  $E_{\gamma} = 10^{15} \, {\rm eV}$  can be explained by comparing  $t_{\rm sh}^{-1}$  with  $t_{p\gamma}^{-1}$  crossing at a steep angle. Photohadronic interactions for low-energy protons inside the acceleration region are suppressed, and in combination with synchrotron losses being dominant, fewer photons are produced inside the acceleration region.

A rough overview of the neutrino interactions occurring in the acceleration region ( $\nu_{in}$ ) and beyond ( $\nu_{out}$ ) in  $S_2$  is given in Fig. 6.8. Since the development of a detailed simulation program has focused on  $S_1$ , in  $S_2$  the program is only able to distinguish between the two different locations for neutrino production without considering the flavor or decay channel. Since the acceleration time in  $S_2$ 

#### Chapter 6 Results and Discussion

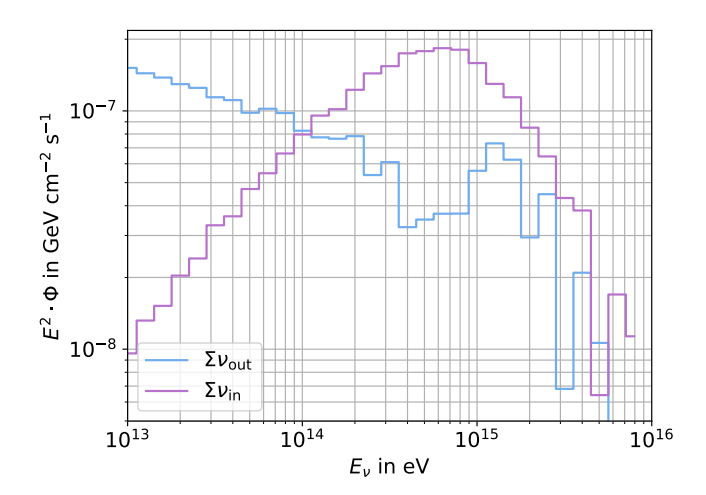


**Figure 6.8:** The neutrino spectrum obtained from the simulation for  $S_2$ , taking into account neutrinos coming from the acceleration region ( $\nu_{\text{in}}$ ) and those produced after the acceleration region ( $\nu_{\text{out}}$ ).

is larger than in  $S_1$ , the particles propagate longer in the acceleration region, and thus may interact more. The steeper shape of the neutrino spectrum in  $S_2$  can be explained by the same arguments that hold for the shape of the photon spectrum. In addition, the same arguments hold for the shape of the neutrino spectrum for neutrinos produced beyond the acceleration region. Thus, the picture manifests that in  $S_2$  the proton interactions beyond the acceleration region are significantly smaller than in  $S_1$  due to the less dense medium.

In conclusion, for  $S_2$  it is possible to accelerate protons in the acceleration region far from the black hole to energies of  $E_p=2\times 10^{16}$  eV, which is one order of magnitude less than in  $S_1$ . Furthermore, the resulting  $\gamma$ -rays and neutrinos reach similar particle fluxes as in  $S_1$  at energies around  $E_{\gamma}=10^{15}$  eV. The main difference to  $S_1$  is that the particle spectra are dominated earlier by the secondaries from within the acceleration region, since interactions outside the acceleration region are minimized due to the less dense medium. Since the important photon interactions occur with the EBL and CMB, there is no significant difference in absorption for PeV photons in either region  $S_1$  or  $S_2$ . It has been argued previously that in the hypersoft state additional acceleration may occur in the vicinity of the black hole. This implies the evolution of both acceleration regions  $S_1$  and  $S_2$ , in which case the two spectra obtained here must be summed, leading to a higher energy flux and thus the need for more restrictive estimates of the mass accretion rate with respect to the LHAASO data.

Cygnus X-3 is recognized as one of the most enigmatic sources in our Galaxy, but the precise acceleration mechanism remains elusive. Measurements of PeV photons from a region containing Cygnus X-3 require precise models for Cygnus X-3, while predicting the combination of interactions is challenging. In previous publications, two promising models explaining the particle spectra and acceleration mechanisms in Cygnus X-3 have been merged. Khiali et al. proposed a configuration for reconnection [45], which was found to lead to high proton energies. Furthermore, Koljonen et al. proposed the existence of two different acceleration regions [8], depending on the jet activity. They that high-energy photons reaching Earth arrive close to HyS as the jet forms a cocoon, leading to another acceleration region far from the dense region.

Estimations and simulations performed in this work found that Cygnus X-3 is efficient at accelerating protons in both regions, leading to significant secondary particle production. For  $S_2$ , photon interactions in the medium were found to be less significant for photons up to energies of  $E_{\gamma} = 10^{14}$  eV. For both acceleration regions, however, it was found that photons with energies above  $E_{\gamma} = 5 \times 10^{14}$  eV interact significantly with the EBL and the CMB and that the shape of the spectrum in both acceleration regions fits well with the LHAASO data. However, since the photon spectra in both  $S_1$  and  $S_2$  had to be corrected by a factor  $10^{-3}$ , the normalization requires further investigation. Possible explanations are a lower accretion rate, a lower cosmic ray efficiency or a lower mass of the black hole.

Based on the results of this work, it is evident that acceleration close to the black hole via reconnection is more efficient than shock acceleration at the edge of the cocoon. In  $S_1$  the photons thus reach higher energies of up to over  $E_{\gamma}=10^{16}\,\mathrm{eV}$ , whereas in  $S_2$  the maximum photon energy is approximately  $E_{\gamma}=7\times10^{15}\,\mathrm{eV}$ . Both acceleration mechanisms can account for the PeV photons measured by the LHAASO collaboration. It has been previously argued that in addition to the shock acceleration at the edge of the cocoon structure, there is also an acceleration close to the black hole in the hypersoft state. Consequently, the calculated fluxes resulting for configuration  $S_1$  are expected to dominate the spectrum over the additional spectrum calculated for  $S_2$  in the hypersoft state.

In this study, the magnetic field is assumed to be high, allowing highly efficient particle acceleration. As a result, the photon spectra reach a high energy range

#### Chapter 7 Conclusion and Outlook

above  $E_{\gamma} = 10$  PeV, which has not yet been detected by any instrument. LHAASO, the leading high-energy photon experiment, currently has an upper limit of a few PeV photons [74]. Consequently, the ability of LHAASO to detect high-energy photons from the calculated edge of the spectrum is limited. On the other hand, the developed program serves as a basis for further research on the crucial parameters in Cygnus X-3 that determine the secondary energies.

This work identified that the acceleration region  $S_1$  is the most promising. This region is characterized by efficient reconnection and proton energies that are first-order limited by photohadronic interactions. Additionally, proton-proton interactions are more probable in the dense stellar medium behind the acceleration region. This led to a focus on developing a program for reconnection that appears close to the black hole. The work showed that for  $S_1$  photons originating from the acceleration region dominate the spectrum above  $E_{\gamma} = 10^{15}$  eV. Interactions occurring outside the acceleration region dominate the spectrum for photon energies below  $E_{\gamma} = 10^{15}$  eV. The whole photon spectrum in  $S_1$  shows a cut-off at about  $E_V = 5 \times 10^{15}$  eV, while in  $S_2$  the picture is different, since the acceleration occurs in the less dense medium. For photon energies above  $E_{\rm Y} = 10^{14} \, {\rm eV}$  the spectrum is dominated by photons emitted from the acceleration region, while beyond the acceleration region photons are less significant. Summarizing, in  $S_1$  proton-proton interactions in the stellar wind play a larger role than in S<sub>2</sub>, while in both acceleration regions the proton and corresponding secondary spectra develop similar slopes, with  $S_2$  leading to a lower energetic cut-off for photons and neutrinos.

In this work it was found that Cygnus X-3 is efficient in accelerating particles resulting in high-energy neutrinos with a flavor ratio of  $1_e:2_\mu:0_\tau$  corresponding to the commonly expected flavor ratio of  $1_e:1_\mu:1_\tau$  [73]. It has been shown for both  $S_1$  and  $S_2$  that the introduction of particle interactions of unstable secondary particles is crucial for the study of the ongoing physical processes. Thus, it may be a useful further development of the program to include accelerations of kaons, pions and muons. Furthermore, this work has deduced that orbital modulation is expected for the photon and neutrino signal if interactions in the extended jet play a dominant role. The simulation showed that in  $S_1$  proton-proton interactions beyond the acceleration region are important. Therefore, not only  $S_2$  but also  $S_1$  could be modulated by the orbit, which is in agreement with previous measurements of Cygnus X-3 and therefore interesting to investigate further [75].

# List of Constants

**Table 7.1:** List of the physical constants and units that were utilized in the present work. It should be noted that all values are expressed in cgs units, unless otherwise indicated.

Constant		Value
Speed of light	c	$2.9979 \times 10^{10} \mathrm{cm}\mathrm{s}^{-1}$
Gravitational constant	G	$6.6743 \times 10^{-8} \text{ cm}^3 \text{ g}^{-1} \text{ s}^{-2}$
Planck constant	h	$6.6261 \times 10^{-27} \mathrm{erg}\mathrm{s}$
Boltzmann constant	$k_B$	$1.3807 \times 10^{-16} \mathrm{erg}\mathrm{K}^{-1}$
Elementary charge	e	$4.8032 \times 10^{-10} \text{ statC}$
Electron mass	$m_e$	$9.1094 \times 10^{-28} \mathrm{g}$
Proton mass	$m_p$	$1.6726 \times 10^{-24} \mathrm{g}$
Neutron mass	$m_n$	$1.6749 \times 10^{-24} \mathrm{g}$
Stefan-Boltzmann constant	$\sigma_{ m SB}$	$5.6704 \times 10^{-5} \mathrm{erg}\mathrm{cm}^{-2}\mathrm{s}^{-1}\mathrm{K}^{-4}$
Thomson cross-section	$\sigma_{ m T}$	$6.6524 \times 10^{-25} \mathrm{cm}^2$
Solar mass	$M_{\odot}$	$1.989 \times 10^{33} \mathrm{g}$
Astronomical unit	AU	$1.496 \times 10^{13} \mathrm{cm}$
Parsec	pc	$3.0857 \times 10^{18} \mathrm{cm}$
Jansky	Jy	$10^{-23}\mathrm{ergcm^{-2}s^{-1}Hz^{-1}}$

## Bibliography

- [1] Thomas K. Gaisser, Ralph Engel, and Elisa Resconi. *Cosmic Rays and Particle Physics: 2nd Edition.* Cambridge University Press, June 2016. ISBN: 978-0-521-01646-9.
- [2] Malcolm S. Longair. *High Energy Astrophysics*. 3rd ed. Cambridge University Press, 2011.
- [3] Alessandro De Angelis. Cosmic Rays. Multimessenger Astrophysics and Revolutionary Astronomy. Astronomers' Universe. Springer, 2023. ISBN: 978-3-031-38559-9, 978-3-031-38560-5. DOI: \url{10.1007/978-3-031-38560-5}.
- [4] D. Bose et al. "Galactic and extragalactic sources of very high energy gamma rays." In: *Eur. Phys. J. ST* 231.1 (2022), pp. 27–66. DOI: 10.1140/epjs/s11734-022-00434-8. arXiv: 2201.06789 [astro-ph.HE].
- [5] Xue-Bing Wu and F. K. Liu. "Black hole mass and accretion rate of active galactic nuclei with double-peaked broad emission lines." In: *Astrophys. J.* 614 (2004), pp. 91–100. DOI: 10.1086/423446. arXiv: astro-ph/0406415.
- [6] N. Sahakyan, G. Piano, and M. Tavani. "Hadronic Gamma-Ray and Neutrino Emission from Cygnus X-3." In: Astrophys. J. 780 (2014), p. 29. DOI: 10.1088/ 0004-637X/780/1/29. arXiv: 1310.7805 [astro-ph.HE].
- [7] G. Piano et al. "The AGILE monitoring of Cygnus X-3: transient gamma-ray emission and spectral constraints." In: *Astron. Astrophys.* 545 (2012), A110. DOI: 10.1051/0004-6361/201219145. arXiv: 1207.6288 [astro-ph.HE].
- [8] K. I. I. Koljonen et al. "The hypersoft state of Cygnus X-3 A key to jet quenching in X-ray binaries?" In: *Astron. Astrophys.* 612 (2018), A27. DOI: 10.1051/0004-6361/201732284. arXiv: 1712.07933 [astro-ph.HE].
- [9] Zhen Cao et al. "An ultrahigh-energy γ-ray bubble powered by a super PeVatron." In: *Sci. Bull.* 69.4 (2024), pp. 449–457. DOI: 10.1016/j.scib.2023.12.040. arXiv: 2310.10100 [astro-ph.HE].
- [10] R. Schlickeiser. Cosmic ray astrophysics. 2002.
- [11] Carmelo Evoli. *The Cosmic-Ray Energy Spectrum*. Dec. 2020. DOI: 10.5281/zenodo.4396125. URL: https://doi.org/10.5281/zenodo.4396125.
- [12] Francesco Riggi. Messengers from the Cosmos. An Introduction to the Physics of Cosmic Rays in Its Historical Evolution. UNITEXT for Physics. Cham, Switzerland: Springer, Nov. 2024. ISBN: 978-3-031-24761-3, 978-3-031-24764-4, 978-3-031-24762-0, 978-3-031-68636-8, 978-3-031-68637-5. DOI: 10.1007/978-3-031-24762-0.
- [13] Kenneth Greisen. "End to the cosmic ray spectrum?" In: *Phys. Rev. Lett.* 16 (1966), pp. 748–750. DOI: 10.1103/PhysRevLett.16.748.

- [14] G. T. Zatsepin and V. A. Kuzmin. "Upper limit of the spectrum of cosmic rays." In: *JETP Lett.* 4 (1966), pp. 78–80.
- [15] V. A. Kuzmin and G. T. Zatsepin. "On cosmic-ray interactions with photons." In: Canadian Journal of Physics 46.10 (1968), S617–S619. DOI: 10.1139/p68-309. eprint: https://doi.org/10.1139/p68-309. URL: https://doi.org/10.1139/p68-309.
- [16] Stephen Myers and Herwig Schopper, eds. *Particle Physics Reference Library*. *Volume 3: Accelerators and Colliders*. Springer, 2020. ISBN: 978-3-030-34244-9, 978-3-030-34247-0, 978-3-030-34245-6. DOI: 10.1007/978-3-030-34245-6.
- [17] Kai Zuber. *Neutrino Physics*. Boca Raton: Taylor and Francis, 2020. ISBN: 978-1-351-76458-2, 978-1-315-19561-2, 978-1-032-24220-0, 978-1-138-71889-0. DOI: 10. 1201/9781315195612.
- [18] Sylvain Chaty. "Nature, formation and evolution of High Mass X-ray Binaries." In: *ASP Conf. Ser.* 447 (2011), p. 29. arXiv: 1107.0231 [astro-ph.HE].
- [19] Francesca M. Fornasini, Vallia Antoniou, and Guillaume Dubus. "High-mass X-ray Binaries." In: (Aug. 2023). arXiv: 2308.02645 [astro-ph.HE].
- [20] Sylvain Chaty. Accreting Binaries. 2514-3433. IOP Publishing, 2022. ISBN: 978-0-7503-3887-5. DOI: 10.1088/2514-3433/ac595f. URL: https://dx.doi.org/10.1088/2514-3433/ac595f.
- [21] M. L. McCollough, K. I. I. Koljonen, and D. C. Hannikainen. "The X-Ray/Radio/Flaring Properties of Cygnus X-3." In: (Mar. 2010). arXiv: 1003.4278 [astro-ph. HE].
- [22] T.J.L. Courvoisier. *High Energy Astrophysics: An Introduction*. Astronomy and Astrophysics Library. Springer Berlin Heidelberg, 2012. URL: https://books.google.no/books?id=GKtUzloqaCMC.
- [23] Chris Shrader, Lev Titarchuk, and Nikolai Shaposhnikov. "New Evidence for a Black Hole in the Compact Binary Cygnus X-3." In: *Astrophys. J.* 718 (2010), pp. 488–493. DOI: 10.1088/0004-637X/718/1/488. arXiv: 1005.5362 [astro-ph.HE].
- [24] Aswath Suryanarayanan, Frits Paerels, and Maurice Leutenegger. "The Highresolution Fe K Spectrum of Cygnus X-3." In: *Astrophys. J.* 969.2 (2024), p. 110. DOI: 10.3847/1538-4357/ad4638. arXiv: 2212.04165 [astro-ph.HE].
- [25] N. I. Shakura and R. A. Sunyaev. "Black Holes in Binary Systems: Observational Appearances." In: *IAU Symp.* 55 (1973), pp. 155–164. DOI: 10 . 1017 / s007418090010035x.
- [26] Valentí Bosch-Ramon and Dmitry Khangulyan. "Understanding the Very-High Emission from Microquasars." In: *Int. J. Mod. Phys. D* 18 (2009), pp. 347–387. DOI: 10.1142/S0218271809014601. arXiv: 0805.4123 (astro-ph).
- [27] R. Fitzpatrick. Classical Electromagnetism. CreateSpace Independent Publishing Platform, 2016. ISBN: 9781530325917. URL: https://books.google.no/books?id=pSi2jwEACAAJ.

- [28] Masud Chaichian et al. *Electrodynamics*. Berlin, Heidelberg: Springer, 2016. DOI: 10.1007/978-3-642-17381-3.
- [29] M. Kachelriess. "Lecture notes on high energy cosmic rays." In: (Jan. 2008). arXiv: 0801.4376 [astro-ph].
- [30] Charles D. Dermer and Govind Menon. *High Energy Radiation from Black Holes: Gamma Rays, Cosmic Rays, and Neutrinos.* Princeton University Press, Oct. 2009. ISBN: 978-0-691-14408-5.
- [31] Fan Guo et al. "Magnetic Reconnection and Associated Particle Acceleration in High-Energy Astrophysics." In: *Space Sci. Rev.* 220.4 (2024), p. 43. DOI: 10.1007/s11214-024-01073-2. arXiv: 2309.13382 [astro-ph.HE].
- [32] P. A. Sweet. "Mechanisms of solar flares." In: *Ann. Rev. Astron. Astrophys.* 7 (1969), pp. 149–176. DOI: 10.1146/annurev.aa.07.090169.001053.
- [33] E. N. Parker. "Acceleration of Cosmic Rays in Solar Flares." In: *Phys. Rev.* 107 (1957), pp. 830-836. DOI: 10.1103/PhysRev.107.830. URL: https://link.aps.org/doi/10.1103/PhysRev.107.830.
- [34] E. M. de Gouveia Dal Pino and A. Lazarian. "Production of the large scale super-luminal ejections of the microquasar GRS 1915+105 by violent magnetic reconnection." In: (July 2003). arXiv: astro-ph/0307054.
- [35] M. M. Hanson, M. D. Still, and Robert P. Fender. "Orbital dynamics of cygnus x-3." In: *Astrophys. J.* 541 (2000), p. 308. DOI: 10.1086/309419. arXiv: astro-ph/0005032.
- [36] Paul A Crowther. "Physical and Wind Properties of [WC] Stars." In: *ASP Conf. Ser.* 391 (2008), p. 83. arXiv: 0710.5774 [astro-ph].
- [37] The LIGO Scientific Collaboration, the Virgo Collaboration, and the KAGRA Collaboration. Observation of Gravitational Waves from the Coalescence of a 2.5 − 4.5 M<sub>☉</sub> Compact Object and a Neutron Star. 2024. arXiv: 2404.04248 [astro-ph. HE]. URL: https://arxiv.org/abs/2404.04248.
- [38] W.D. McComb. *Dynamics and Relativity*. Oxford University Press, 1999. URL: https://books.google.no/books?id=REeqQgAACAAJ.
- [39] G. Dubus, B. Cerutti, and G. Henri. "The relativistic jet of Cygnus X-3 in gamma rays." In: *Mon. Not. Roy. Astron. Soc.* 404 (2010), p. 55. DOI: 10.1111/j.1745-3933.2010.00834.x. arXiv: 1002.3888 [astro-ph.HE].
- [40] Karri I. I. Koljonen et al. "The disk/jet connection in the enigmatic microquasar Cygnus X-3." In: *Proceedings of the International Astronomical Union* 6.S275 (2010), pp. 285–289. DOI: 10.1017/S1743921310016170.
- [41] Michael A. Nowak. "Toward a unified view of black hole high-energy states." In: *Publ. Astron. Soc. Pac.* 107 (1995), p. 1207. DOI: 10.1086/133679. arXiv: astro-ph/9509046.
- [42] Robert P. Fender et al. "Cygnus x-3 in outburst: quenched radio emission, radiation losses and variable local opacity." In: *Mon. Not. Roy. Astron. Soc.* 288 (1997), p. 849. DOI: 10.1093/mnras/288.4.849. arXiv: astro-ph/9612125.

- [43] P. Varniere, M. Tagger, and J. Rodriguez. "A microquasar classification from a disk instability perspective." In: *Astron. Astrophys.* 525 (2011), A87. DOI: 10.1051/0004-6361/201015028. arXiv: 1009.5330 [astro-ph.HE].
- [44] James C. A. Miller-Jones et al. "Time-sequenced multi-radio-frequency observations of Cygnus X-3 in flare." In: *Astrophys. J.* 600 (2004), pp. 368–389. DOI: 10.1086/379706. arXiv: astro-ph/0311277.
- [45] B. Khiali, E. M. de Gouveia Dal Pino, and M. V. del Valle. "A magnetic reconnection model for explaining the multiwavelength emission of the microquasars Cyg X-1 and Cyg X-3." In: *Monthly Notices of the Royal Astronomical Society* 449.1 (Mar. 2015), pp. 34–48. ISSN: 0035-8711. DOI: 10.1093/mnras/stv248. eprint: https://academic.oup.com/mnras/article-pdf/449/1/34/4130786/stv248.pdf. URL: https://doi.org/10.1093/mnras/stv248.
- [46] E. B. Waltman et al. "Quenched Radio Emission in Cygnus X-3." In: *Astron. J.* 112 (Dec. 1996). Provided by the SAO/NASA Astrophysics Data System, p. 2690. eprint: 10.1086/118213. URL: https://ui.adsabs.harvard.edu/abs/1996AJ....112.2690W.
- [47] Amy J. Mioduszewski et al. "A one-sided, highly relativistic jet from cygnus x-3." In: *Astrophys. J.* 553 (2001), p. 766. DOI: 10.1086/320965. arXiv: astro-ph/0102018.
- [48] Günter Sigl. Astroparticle Physics: Theory and Phenomenology. Vol. 1. Atlantis Studies in Astroparticle Physics and Cosmology. Springer, 2017. ISBN: 978-94-6239-242-7, 978-94-6239-243-4. DOI: 10.2991/978-94-6239-243-4.
- [49] Cerutti, B. and Dubus, G. and Malzac, J. and Szostek, A. and Belmont, R. and Zdziarski, A. A. and Henri, G. "Absorption of high-energy gamma rays in Cygnus X-3." In: *A and A* 529, A120 (May 2011), A120. DOI: 10.1051/0004-6361/201116581. arXiv: 1103.3875 [astro-ph.HE].
- [50] F. Cangemi et al. "INTEGRAL discovery of a high-energy tail in the microquasar Cygnus X-3." In: *Astron. Astrophys.* 645 (2021), A60. DOI: 10.1051/0004-6361/202037951. arXiv: 2011.06863 [astro-ph.HE].
- [51] Thomas Lacroix and Joseph Silk. "Constraining the distribution of dark matter at the Galactic Centre using the high-resolution Event Horizon Telescope." In: *Astron. Astrophys.* 554 (2013), A36. DOI: 10.1051/0004-6361/201220753. arXiv: 1211.4861 [astro-ph.GA].
- [52] Grzegorz Kowal, Elisabete M. de Gouveia Dal Pino, and A. Lazarian. "Particle Acceleration in Turbulence and Weakly Stochastic Reconnection." In: *Phys. Rev. Lett.* 108 (2012), p. 241102. DOI: 10.1103/PhysRevLett.108.241102. arXiv: 1202.5256 [astro-ph.HE].
- [53] Damiano Caprioli and Anatoly Spitkovsky. "Simulations of Ion Acceleration at Non-relativistic Shocks. III. Particle Diffusion." In: *Astrophys. J.* 794.1 (2014), p. 47. DOI: 10.1088/0004-637X/794/1/47. arXiv: 1407.2261 [astro-ph.HE].
- [54] Francesco Lacava. Classical Electrodynamics. From Image Charges to the Photon Mass and Magnetic Monopoles. Undergraduate Lecture Notes in Physics. Springer, 2016. ISBN: 978-3-319-39474-9.

- [55] S. Navas et al. "Review of particle physics." In: *Phys. Rev. D* 110.3 (2024), p. 030001. DOI: 10.1103/PhysRevD.110.030001.
- [56] A. Mucke et al. "SOPHIA: Monte Carlo simulations of photohadronic processes in astrophysics." In: *Comput. Phys. Commun.* 124 (2000), pp. 290–314. DOI: 10. 1016/S0010-4655(99)00446-4. arXiv: astro-ph/9903478.
- [57] M. Kachelriess, S. Ostapchenko, and R. Tomas. "High energy neutrino yields from astrophysical sources. 2. Magnetized sources." In: *Phys. Rev. D* 77 (2008), p. 023007. DOI: 10.1103/PhysRevD.77.023007. arXiv: 0708.3047 [astro-ph].
- [58] Armen M. Atoyan and Charles D. Dermer. "Neutral beams from blazar jets." In: Astrophys. J. 586 (2003), pp. 79–96. DOI: 10.1086/346261. arXiv: astro-ph/0209231.
- [59] S. R. Kelner, Felex A. Aharonian, and V. V. Bugayov. "Energy spectra of gammarays, electrons and neutrinos produced at proton-proton interactions in the very high energy regime." In: *Phys. Rev. D* 74 (2006). [Erratum: Phys.Rev.D 79, 039901 (2009)], p. 034018. DOI: 10.1103/PhysRevD.74.034018. arXiv: astro-ph/0606058.
- [60] Sergey Ostapchenko. "QGSJET-III model of high energy hadronic interactions: The formalism." In: *Phys. Rev. D* 109.3 (2024), p. 034002. DOI: 10.1103/PhysRevD. 109.034002. arXiv: 2401.06202 [hep-ph].
- [61] Donald E. Groom, Nikolai V. Mokhov, and Sergei I. Striganov. "Muon stopping power and range tables 10-MeV to 100-TeV." In: *Atom. Data Nucl. Data Tabl.* 78 (2001), pp. 183–356. DOI: 10.1006/adnd.2001.0861.
- [62] G. R. Blumenthal and R. J. Gould. "Bremsstrahlung, synchrotron radiation, and compton scattering of high-energy electrons traversing dilute gases." In: *Rev. Mod. Phys.* 42 (1970), pp. 237–270. DOI: 10.1103/RevModPhys.42.237.
- [63] G. B. Rybicki and A. P. Lightman. Radiative Processes in Astrophysics. Wiley-VCH, 2004. ISBN: 978-0-471-82759-7, 978-3-527-61817-0. DOI: 10.1002/97835276-18170.
- [64] Robert J. Gould and Gerard P. Schreder. "Pair Production in Photon-Photon Collisions." In: *Phys. Rev.* 155 (1967), pp. 1404–1407. DOI: 10.1103/PhysRev. 155.1404.
- [65] Divjyot Singh et al. "Low-energy Injection and Nonthermal Particle Acceleration in Relativistic Magnetic Turbulence." In: *Astrophys. J.* 979.1 (2025), p. 39. DOI: 10.3847/1538-4357/ad9b12. arXiv: 2404.19181 [astro-ph.HE].
- [66] J. G. Kirk and R. O. Dendy. "Shock acceleration of cosmic rays: A Critical review."
   In: J. Phys. G 27 (2001). Ed. by M. Giller, pp. 1589–1596. DOI: 10.1088/0954-3899/27/7/316. arXiv: astro-ph/0101175.
- [67] R. C. Gilmore et al. "Semi-analytic modeling of the EBL and consequences for extragalactic gamma-ray spectra." In: *Mon. Not. Roy. Astron. Soc.* 422 (2012), p. 3189. DOI: 10.1111/j.1365-2966.2012.20841.x. arXiv: 1104.0671 [astro-ph.CO].

- [68] Hyesung Kang and Dongsu Ryu. "Diffusive Shock Acceleration in Test-Particle Regime." In: *Astrophys. J.* 721 (2010), pp. 886–892. DOI: 10.1088/0004-637X/721/1/886. arXiv: 1008.0429 [astro-ph.HE].
- [69] F. Tavecchio et al. "Probing the low-energy particle content of blazar jets through MeV observations." In: *Astron. Astrophys.* 694 (2025), p. L3. DOI: 10.1051/0004-6361/202453411. arXiv: 2412.09089 [astro-ph.HE].
- [70] D. Karavola et al. "Neutrino and pair creation in reconnection-powered coronae of accreting black holes." In: (Oct. 2024). arXiv: 2410.12638 [astro-ph.HE].
- [71] Alexandra Veledina et al. "Cygnus X-3 revealed as a Galactic ultraluminous X-ray source by IXPE." In: *Nature Astron.* 8.8 (2024), pp. 1031–1046. DOI: 10.1038/s41550-024-02294-9. arXiv: 2303.01174 [astro-ph.HE].
- [72] Karri I. I. Koljonen and Thomas J. Maccarone. "Gemini/GNIRS infrared spectroscopy of the Wolf-Rayet stellar wind in Cygnus X-3." In: *Mon. Not. Roy. Astron. Soc.* 472.2 (2017), pp. 2181–2195. DOI: 10.1093/mnras/stx2106. arXiv: 1708.04050 [astro-ph.HE].
- [73] M. G. Aartsen et al. "Flavor Ratio of Astrophysical Neutrinos above 35 TeV in Ice-Cube." In: *Phys. Rev. Lett.* 114.17 (2015), p. 171102. DOI: 10.1103/PhysRevLett. 114.171102. arXiv: 1502.03376 [astro-ph.HE].
- [74] Zhen Cao. "LHAASO Status and Physics Results." In: *EPJ Web Conf.* 280 (2023), p. 01003. DOI: 10.1051/epjconf/202328001003.
- [75] A. A. Abdo et al. "Modulated High-Energy Gamma-Ray Emission from the Microquasar Cygnus X-3." In: *Science* 326.5959 (2009), pp. 1512–1516. DOI: 10.1126/science.1182174.